Numerical Failure Pressure Prediction of Crack-in-Corrosion Defects in Natural Gas Transmission Pipelines

by

Badr Bedairi

A thesis
presented to the University of Waterloo
in fulfillment of the
thesis requirement for the degree of
Master of Applied Science
in
Mechanical Engineering

Waterloo, Ontario, Canada, 2010

AUTHOR'S DECLARATION

I hereby declare that I am the sole author of this thesis. This is a true copy of the thesis, including any required final revisions, as accepted by my examiners.

I understand that my thesis may be made electronically available to the public.

Abstract

The aim of this study was to use the finite element method to model crack, corrosion, and Crack-in-Corrosion defects in a pipeline. The pipe material under investigation for this study was API 5L X60, 508 mm diameter with a wall thickness of 5.7 mm. The pipe material was evaluated using Tensile, Charpy, and J testing in order to model the defects and to establish the numerical failure criteria.

Corrosion defects were modeled as flat-bottomed grooves. The collapse pressure was predicted when the deepest point in the bottom of the defect reached a critical stress. Based on this criterion, the FE corrosion failure pressure predictions were conservative compared to the experimental failure pressures, conducted by Hosseini [9], with an average error of 10.13%.

For crack modeling, the failure criteria were established considering the plastic collapse limit and the fracture limit. Both the Von Mises stress in the crack ligament and the J-integral values around the crack were monitored to predict the failure pressure of the model. The crack modeling was done based on two approaches, the uniform depth profile and the semi-elliptical profile. The crack with uniform depth profile was done because the uniform shape is the logical equivalent shape for a colony of cracks. The crack with the semi-elliptical profile was done to have a less conservative results and because the experiments were done with semi-elliptical cracks. The FE crack modeling results were conservative compared to the experimental collapse pressure with an average error of 19.64% for the uniform depth profile and 5.35% for the semi-elliptical profile.

In crack-in-corrosion (CIC) defect modeling, the crack was modeled with uniform depth because it was very difficult to model the semi-elliptical crack profile when the crack defect is coincident with a corrosion defect. The results were conservative compared to the experimental results with an average error of 22.18%.

In general, the FE modeling provides the least conservative failure pressure prediction over the existing analytical solutions for pipe with longitudinal corrosion, crack, and CIC defects.

Acknowledgments

I am heartily thankful to Alla for his help and his countless gifts.

I am also thankful to my supervisors, Professor Duane Cronin and Professor Alan Plumtree, who guided, and encouraged me through my research program.

I would also thank my mother for her nightly prayers. I also thank my role model and my big brother Engineer Tariq for his support.

To my brothers and sisters especially, Hani and Wajanat, I give my thanks for being with me on Skype.

I also acknowledge my friends Dr. Amin Eshraqi and Ali Hosseini for their friendship and help over the past two years.

Table of Contents

Author’s Declaration..ii
Abstract iii
Acknowledgments v
List of Figures.. ix
List of Tables xv
List of Symbols... xvii
Chapter 1 Introduction...1
Chapter 2 Background..4

2.1 Corrosion Defects...5

2.1.1 Current Assessment Methods for Corrosion Defect..9

2.1.2 Modified B31-G..9

2.1.3 RSTRENG..12

2.1.4 FE Modeling of Corrosion..13

2.2 Crack Defect Overview...16

2.2.1 LEFM 16

2.2.2 EPFM 17

2.3 Current Codes for Crack-Like Flaws Assessment...19

2.3.1 Failure Assessment Diagram (FAD) 19

2.3.2 NG-18 23

2.3.3 CorLAS 24

2.3.4 FE Modeling of Cracks 25

Chapter 3 Experimental Testing 35

3.1 Corrosion Defect Experimental Data 35

3.2 Crack Defects Experimental Data 38

3.3 Crack-in-Corrosion (CIC) Experimental Data 40

Chapter 4 Material Characterization 45

4.1 Tensile Testing 45

4.2 Charpy V-notch Test 52

4.3 Fracture Toughness Empirical Evaluation 56

4.4 J-Integral Test 60

Chapter 5 Numerical Analysis 69

5.1 Overview 69

5.2 Corrosion Defect Numerical Evaluation 70

5.3 Crack Defect Numerical Evaluation 76

5.4 Crack-in-Corrosion (CIC) Defect Numerical Evaluation 89

Chapter 6 Results and Discussion 96
Chapter 7 Conclusions and Recommendations 99
References 101
Appendix A 105
Appendix B 110

List of Figures

Figure 2.1 Uniform Corrosion [12]. 5

Figure 2.2 Pitting Corrosion [12]. 6

Figure 2.3 Crevice Corrosion [12]. 6

Figure 2.4 Intergrangular Corrosion [12]. 7

Figure 2.5 Erosion Corrosion [13]. 7

Figure 2.6 Stress Corrosion Cracking [16] 8

Figure 2.7 Inspection Planes and the Critical Thickness Profile [1]. 11

Figure 2.8 The Difference in the Projected Area in Modified B31G and RSTRENG [4]. 12

Figure 2.9 Mode I loading [19] 17

Figure 2.10 Line J-Integral around the crack tip [16], ... 18

Figure 2.11 Level 1 FAD 20

Figure 2.12 Failure Assessment Diagram Level 2 [1] 21

Figure 2.13 Failure Assessment Diagram Level 3 [20]. 22

Figure 2.14 Ligament Yielding Range [40]. 23

Figure 2.15 Crack Tip [7] 26

Figure 2.16 Plastic Zone and K-dominance [7] 28

Figure 2.17 8-Nodes Isoparametric Element at Crack Tip [7] 29

Figure 2.18 Contour Integral [7] 30

Figure 2.19 Crack Extension Direction [7] 30

Figure 2.20 Blunt crack Tip and the Contours [7] 31

Figure 2.21 Nonlinear Elastic Material Behavior 32

Figure 2.22 Element Size at the Notch Tip Radius [7] 33

Figure 3.1 Corrosion Defect Dimensions 35

Figure 3.2 Burst Test of The 61%WT Corroded Pipe [9] 36

Figure 3.3 Experimental and Analytical Failure Pressure Results in Corroded Pipe [9] 37

Figure 3.4 Semi-elliptical Crack Geometry [9] 38

Figure 3.5 Experimental and Analytical Failure Pressure Results in Cracked Pipe [9] 40

Figure 3.6 Transverse View Through CIC Flaw and Definition of Depth [9] 41

Figure 3.7 Experimental and Analytical Failure Pressure Results in CIC Defected Pipe [9] 43

Figure 3.8 Experimental Summary of Corrosion, Crack, and CIC Defects [9] 44

Figure 4.1Tensile Test Specimen Dimensions... 46

Figure 4.2 True Stress-Strain Curve for all Circumferential Tensile Test Samples............................ 49

Figure 4.3 Exponential Curve Fitting to the True Stress-Strain Curve (C2) 49

Figure 4.4 Average True Stress Strain Curve in Circumferential Direction...................................... 51

Figure 4.5 Sub-Size Specimen Dimensions for Charpy Test [42]. 52

Figure 4.6 Scaled Energy-Temperature Chart 54

Figure 4.7 Percent Shear Fracture Chart 56

Figure 4.8 CVN Vs. K_{IC} Tyson [27]... 58

Figure 4.9 CVN Vs. $J_{0.2}$ Mak & Tyson [28]. 58

Figure 4.10 CVN Vs. $J_{0.2}$ 59

Figure 4.11 J-Integral Test Results for the First Test Set 61

Figure 4.12 J-R Curve (First test) 64

Figure 4.13 The Effect of Thickness on the Fracture Toughness [38] 65

Figure 4.14 Evaluation of $J_{0.2}$ (First test) 66

Figure 4.15 Evaluation of $J_{0.2}$ (Second test) 66

Figure 4.16 Evaluation of $J_{0.2}$ (Third test) 67

Figure 5.1 Plain Strain Boundary Conditions 70

Figure 5.2 45% Corrosion Model 71

Figure 5.3 Corrosion Defect Failure Pressure Analysis 72

Figure 5.4 Numerical Failure Pressure Prediction of the Corrosion Defect 73

Figure 5.5 Corrosion Defect Analysis and Comparison [9] 74

Figure 5.6 Average Error Comparison between Corrosion Defect Failure Prediction Methods 75

Figure 5.7 Comparison between LEFM and EPFM Modeling 76

Figure 5.8 Crack Defect (Uniform depth Profile) Model 78

Figure 5.9 FE Analysis of 38%WT Crack Model (Uniform Depth Profile) 79

Figure 5.10 FE Analysis of 47%WT Crack Model (Uniform Depth Profile) 80

Figure 5.11 FE Analysis of 48%WT Crack Model (Uniform Depth Profile) 80

Figure 5.12 FE Analysis of 51%WT Crack Model (Uniform Depth Profile) 81

Figure 5.13 Side View of Experimental and FE Modeled Uniform Depth Crack Profile 82

Figure 5.14 Side View of Experimental and FE Modeled Semi-elliptical Crack Profile 83

Figure 5.15 Crack Defect Model (Semi-elliptical Profile) 84

Figure 5.16 FE Analysis of 38%WT crack Model (Semi-elliptical Profile) 85

Figure 5.17 FE Analysis of 47%WT crack Model (Semi-elliptical Profile) 85

Figure 5.18 FE Analysis of 48%WT crack Model (Semi-elliptical Profile) 86

Figure 5.19 FE Analysis of 51%WT crack Model (Semi-elliptical Profile) 86

Figure 5.20 Comparison between FE and Analytical Failure Pressure Prediction. 88

Figure 5.21 Crack Defect Comparison between FE, Experiment, and Analytical Failure Pressure [9] 89

Figure 5.22 CIC Defect Profile 90

Figure 5.23 View of Actual and Modeled CIC Profile 91

Figure 5.24 Failure Pressure Analysis of CIC-1 92

Figure 5.25 Failure Pressure Analysis of CIC-2 92

Figure 5.26 Failure Pressure Analysis of CIC-3 93

Figure 5.27 Failure Pressure Analysis of CIC-4 93

Figure 5.28 Failure Pressure Analysis of CIC-5 94

Figure 5.29 Comparison Between Experimental and FE Results for CIC Modeling [9] 95

List of Tables

Table 3.1 Experimental and Analytical Failure Pressure Results in Corroded Pipe [9] 36

Table 3.2 Geometry of the Artificial Crack Defect [9] 38

Table 3.3 Failure Pressure Results in Cracked Pipe [9] 39

Table 3.4 Geometry of Tested Pipes for Crack-in-Corrosion Defects [9] 41

Table 3.5 Experimental and Analytical Failure Pressure Results in CIC Defected Pipe [9] 42

Table 4.1 Longitudinal Tensile Test Results 46

Table 4.2 Circumferential Tensile Test Results 47

Table 4.3 True Stress and Ramberg-Osgood Material Parameters - Circumferential Direction 50

Table 4.4 Summary of The Tensile Test Results 51

Table 4.5 Non Scaled Charpy Test Results 53

Table 4.6 Scaled Charpy Test Results 54

Table 4.7 Shear Fracture Percentage Results 55

Table 4.8 Summary of Charpy V-notch Test Results 56

Table 4.9 Empirical Conversion of CVN Energy to K_{IC} and $J_{0.2}$ 59

Table 4.10 Summary of $J_{0.2}$ Results 67

Table 5.1 FE and Analytical Results for Corrosion Modeling 73

Table 5.2 Comparison Between Experimental and FE Results for Corrosion Modeling 74

Table 5.3 FE Results for Crack Defect (Uniform Depth Profile) 81

Table 5.4 Crack Defect (Uniform Depth Profile) Analysis and Comparison [9] 82

Table 5.5 Crack Defect (Semi-elliptical profile) Analysis and Comparison 87

Table 5.6 CIC Defect Geometry [9] 90

Table 5.7 Comparison Between Experimental and FE Results for CIC Modeling 94

List of Symbols

A	Fracture area of the Charpy specimen
$A1$	Maximum Charpy energy
A_o	Crack defect area
$A2$	Minimum Charpy energy
A_{pl}	Area under force versus displacement recorded from J-testing
α	Material coefficient for the Ramberg-Osgood relationship
α	Exponential coefficient
a	Crack length
a_i	Initial crack size
B	Material thickness
B_N	Net specimen thickness
b_o	Remaining ligament (distance from the original crack front to back of the specimen
C	Paris constant
c	½ Crack or corrosion length in longitudinal direction
c_{eq}	Crack half length
CVN	Charpy impact energy for full size specimen
CVN^S	Charpy impact energy for sub-size specimen
D	Pipe diameter
d	Defect depth
δ	Crack-tip opening displacement

δ_V	Side deflection (parallel to the external load)
δ_H	Side deflection (transverse to the external load)
Δa	Crack extension
Δa_{max}	Maximum crack extension
ΔK	Stress intensity range
E	Modulus of Elasticity
E'	Elasticity modulus for plane strain
$f_{ij}^{I}(\theta)$	Function of the angular variation of the stress in mode I loading
$f_{ij}^{II}(\theta)$	Function of the angular variation of the stress in mode II loading
$f_{ij}^{III}(\theta)$	Function of the angular variation of the stress in mode III loading
e	Engineering strain
ϵ	Total strain
ϵ_e	Elastic strain
ϵ_p	Plastic strain
ε_{ref}	Reference strain
ε_T	True strain
G	Arbitrary load or moment applied to the system
H	Horizontal force applying on the pipe
J	J integral
$J_{0.2}$	Resistance against stable crack initiation in J-integral terms at the point of 0.2 mm
J_c	Fracture toughness in J-integral determined at the point of instability

J_{el}	J-Integral the elastic part
J_{pl}	J-Integral the plastic part
J_{max}	Maximum capacity of J-Integral
J_{limit}	J-Integral limit
K_I	Stress Intensity (mode I loading)
K_{IC}	Fracture toughness of material
K_{th}	Threshold stress intensity
K_{mat}	Lower bound estimate for fracture toughness of material
K_r	Toughness ratio (FAD) (=K_I / K_c)
L_r^P	Abscissa of the failure assessment diagram (FAD Level 2 &3) (=σ_{ref}^P / σ_Y)
m	Paris constant
M_0	Bending moment
M_p	Bulging factor
M_t	Folias bulging factor
M_{Max}	Maximum bending moment
n	Strain hardening exponential
P	Force recorded from J-testing specimen
P_f	Failure pressure
R	Pipe radius
r_p	Plastic zone radius
s	Arc length in J-integral contour

$\mathrm{S_r}$	Abscissa of the failure assessment diagram (FAD Level 1) (=$\sigma_{\mathrm{ref}}^{\mathrm{P}}$ / σ_{flow})
σ_{h}	Hoop stress
σ_{m}	Nominal stress
σ_{Y}	Yield strength
σ_{T}	True stress
σ_{u}	Ultimate tensile strength
σ_{Eng}	Engineering stress
$\sigma_{\mathrm{ref}}^{\mathrm{P}}$	Reference stress
$\bar{\sigma}$	Flow stress
T	Temperature
T_o	Transition temperature
Γ	Arbitrary path enclosing the crack tip
t	Pipe wall thickness
$\mathrm{t_c}$	Thickness of the full-size specimen
$\mathrm{t_c^s}$	Thickness of the sub-size specimen
T	Traction vector
u	Displacement vector
U	Strain energy
V	Vertical force applying on the pipe
W	The strain energy density
W	Specimen width (J-testing specimen)

x1,x2	Coordinate directions
Y	Dimensionless geometry factor

Chapter 1 Introduction

Pipelines have been used widely since the 1860s because they are the most economical way to transport high capacities of natural gas, oil and other products. In Canada for example, 97% of the natural gas and oil are transported by pipelines [1]. Canada uses pipelines to produce and export crude oil to the USA. In 2005 Canada was known as the second largest exporter of natural gas with a value of $27.8 billion [1]. In order to meet the forecast production increases, the production is expected to be doubled by 2015 [1].

At present, many pipelines are several decades old and may have experienced corrosion damage as a result of aging and the corrosive environment. This has led to the need for integrity assessment improvement for defects such as corrosion, cracks in welds, or dents. Some crack defects are due to coating or cathodic protection degeneration. Corrosive environments and damage during fabrication are also factors that may lead to pipelines defects.

Traditionally, the pipeline companies used to investigate a pipe section after the failure. With high-resolution inspection devices such as ultrasonic pigs, the operators have better awareness of the condition of the pipelines. The cost of regular inspection and repair of significant defects is more economical than the cost of replacing the failed line [2]. Thus, several failure assessment methods were developed over the past several years to evaluate the failure pressure of different pipeline defects. The current methods that assess pipeline defects are typically conservative, which causes unnecessary removal or repair of some pipe sections. Therefore, it is important to understand how critical a defect is and to make the right decision about a damaged pipe section.

Corrosion is one of the common defects found in operating pipelines. It is commonly found on the external surface of the pipe due to improper cathodic protection or coating. These defects may also be found on the internal surface of the pipe due to product contamination. Currently, there are accepted evaluation techniques such as the Modified B31G and RSTRENG [3] to assess corrosion defects. Although these techniques have been used successfully, they are considered to be conservative. Most recently, Elastic-Plastic finite element models have been used to provide more accurate results in evaluating the corrosion defects [4].

Another type of critical defect is cracking. Cracks may occur in welds or in the pipe body. Several analytical assessment methods have been discovered to evaluate the failure pressure of a cracked pipe such as API579 [5] and BS 7910 [6]. On the other hand, FE commercial programs such as ABAQUS [7] and ANSYS [8] can be used to numerically evaluate the collapse pressure of crack defects.

Recently, in operating pipelines, a form of hybrid defect has been identified known as Crack-in-Corrosion (CIC). CIC is a hybrid form of defect that contains cracks coincident with a significant amount of corrosion. This type of defect has not been studied extensively and needs to be investigated to improve the evaluation methods of pipeline integrity.

The primary focus of this study was to include advanced numerical modeling analysis to predict the failure pressure of pipes with corrosion, crack, and CIC defects. The finite element program ABAQUS was used to model a series of experimental rupture tests. It should be noted that Trans Canada Pipeline Company (TCPL) provided several pipe sections which were used later for material characterization and burst tests.

In this study, in chapter 2 a background is given to understand the pipeline defect problem. In chapter 3, relevant experimental results carried out by Hosseini [9] are given. In chapter 4, the material properties are evaluated for the material from the experimentation tests, in order to have a good material representation for the modeling. Numerical modeling for simulated corrosion, crack, and CIC defects are carried out in chapter 5. The results are then compared to the experimental and analytical results for validation and comparison. Chapter 6 discusses the modeling results. The last chapter contains the conclusions and recommendations.

Chapter 2 Background

Corrosion and crack defects are known and have been investigated extensively in the past years, while CIC defects are relatively new and need to be investigated [10]. CIC defects may occur in pipelines due to weak cathodic protection or coating damage. In 2006 a study was undertaken by Cronin and Plumtree on pipes that had long cracks within long corrosion grooves. The results showed that the collapse pressures of these hybrid defects fell between those for cracks and corrosion [10]. A reduced collapse pressure was noted for shallower defects due to the contribution of local bending to the local stress within the defect. Because crack defects are usually more critical than corrosion defects, one procedure to deal with the cracks is by grinding them out resulting in a smooth metal loss defect, similar to corrosion.

Although, corrosion and crack defects have several codes to assist in determining the integrity of the pipes, numerical analysis or finite element method (FEM) gives more accurate results [4] when material properties and defect geometries are closely matched to those determined by experiment. For CIC defects, numerical modeling is an important tool to be used for collapse pressure prediction. To understand the behavior of the CIC defects, crack and corrosion defects should be studied separately first. The modeling procedure and failure criteria have to be established for both types of defects that form the CIC defect. The following sections review the different methods that evaluate the failure pressure in corrosion and crack defects, including general information about the assessment methods as well as an explanation of the source of conservatism in each method.

2.1 Corrosion Defects

Pipelines are usually made of steel and buried under ground. Corrosion defects occur because of chemical or electrochemical interactions between the pipe and the surrounding environment on both the internal and external surfaces [11]. As a result, material losses could compromise the pipe integrity. In 2002-2003 The U. S. Department of Transportation's Research and Special Programs Administration, Office of Pipeline Safety (RSPA/OPS) concluded that 25.6% of the natural gas transmission incidents were caused by corrosion with property damages of $24,273,051[13]. The types of corrosion are classified according to the following categories [11]:

- **Uniform corrosion**

The corrosion in this type has the same depth over the whole corroded pipe surface. The extent of the corrosion can be measured as the mass loss per unit area. Figure 2.1 shows a corroded pipe.

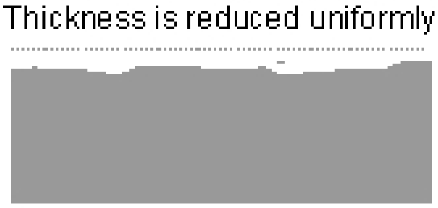

Figure 2.1 Uniform Corrosion [12].

- **Pitting**

Due to localized corrosion, pits are created on the surface of the pipe.

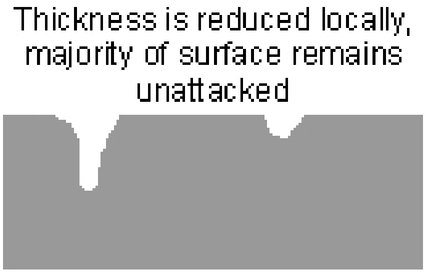

Figure 2.2 Pitting Corrosion [12].

- **Crevice corrosion**

When a break in the pipe surface occurs, crevice corrosion is immediately formed around the break as shown in Figure 2.3.

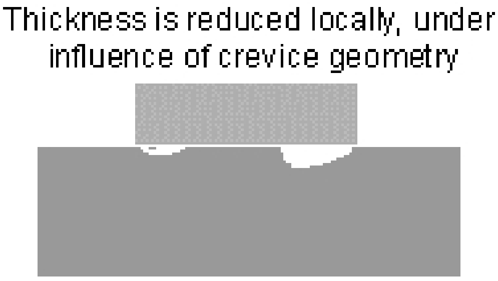

Figure 2.3 Crevice Corrosion [12].

- **Intergranular corrosion**

Occurs at the grain boundaries of the metal as shown in Figure 2.4.

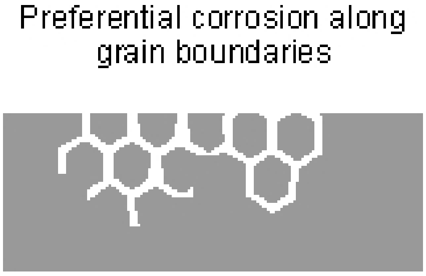

Figure 2.4 Intergrangular Corrosion [12].

- **Erosion corrosion**

Fast flowing liquids with high levels of turbulence result in erosion corrosion on the inner surface of the pipe, especially in elbows. Figure 2.5 shows the erosion corrosion.

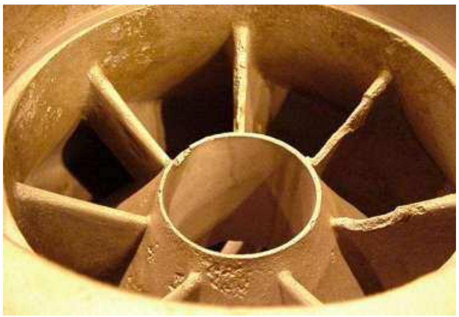

Figure 2.5 Erosion Corrosion [13].

- **Environment-induced cracking**

  Joint action of mechanical stress and corrosion is the cause of this type of corrosion. Stress Corrosion Cracking (SCC) is included in this group of corrosion defects.

When a corrosion defect occurs on the internal or external pipe surface as shown in Figure 2.6, the integrity of the pipe is reduced. The important parameters that determine the strength of a pipe are as follows [4]:

- Internal pressure.
- Pipe Diameter.
- The defect depth related to the wall thickness.
- Ultimate tensile strength.
- Yield strength and stain hardening behavior.
- Fracture toughness.

Figure 2.6 Stress Corrosion Cracking [16]

2.1.1 Current Assessment Methods for Corrosion Defect

Several methods were developed to evaluate the failure pressure caused by corrosion defects in pipelines. The most recent and accepted methods are modified B31G and RSTRENG [3]. Both methods were developed using the NG-18 approach as a basis for the failure caused by part-wall flaw. The Modified B31G and RSTRENG approaches differ in their approximations of the Folias factor [3], defect profile, and flow stress. These methods approximate the complex corrosion profile in different ways. The Finite element method has been found to provide an accurate estimation of the failure pressure of the corroded pipes [4].

2.1.2 Modified B31-G

For many years the corrosion defect assessment codes have been developed for the safety of pipelines. The Battelle Memorial Institute in Columbus, Ohio carried out much of the original work that led to the development of the through-wall and part-wall NG-18 equations, used for the failure analysis of the flaws. This approach incorporates the Folias factor and was originally used by Eiber [14] to describe the failure of through-wall defects in pipes. Battelle's work resulted in being included a section of the American code B31G. The B31G criterion was based on the assumption that the maximum principle stress (hoop stress) in the plain pipe controlled failure. B31G was improved later to Modified B31G to provide less conservative results. Modified B31G was a major development by changing the approximated parabolic defect profile area in B31G from 2/3dmax l to 0.85dmax l [3]. According to the NG-18 surface flaw equations, there is a direct relation between flow stress, bulging factor (Folias factor M) and defect geometry [3] as follows:

$$\sigma_\theta = \bar{\sigma}\left[\frac{1-\frac{D}{t}}{1-\left(\frac{D}{t}\right)\frac{1}{M}}\right] \qquad (2.1)$$

Where D is the pipe diameter and t is the pipe wall thickness. Equation (2.1) can be rewritten for Modified B31G as follows:

$$\sigma_\theta = \bar{\sigma}\left[\frac{1-0.85\frac{D}{t}}{1-0.85\left(\frac{D}{t}\right)\frac{1}{M}}\right] \qquad (2.2)$$

The bulging factor M is given by [3]:

$$M = \sqrt{1+0.6275\left(\frac{2C}{\sqrt{Dt}}\right)^2-0.003375\left(\frac{2C}{\sqrt{Dt}}\right)^4} \qquad (2.3)$$

$\bar{\sigma}$(flow stress) $= \sigma_y + 69.8$ (MPa) $=\sigma_y + 10$ (ksi)

The failure pressure may be expressed by [3]:

$$P_f = \left(\frac{t}{R}\right)\bar{\sigma}\left[\frac{1-0.85\frac{D}{t}}{1-0.85\left(\frac{D}{t}\right)\frac{1}{M}}\right] \qquad (2.4)$$

The above equation typically underestimates the remaining strength of the pipe by assuming that the corrosion is lying axially along the pipe surface, which may not be the actual case. In addition, Modified B31G gives conservative results because it assumes that the corrosion pits are blunt defects, compared to other defects such as cracks. It was shown that sharp surface flaws have significantly lower collapse pressure than blunt surface defects [3]. Moreover, the data from the burst tests used in developing equation (2.4) contained sharp flaws [3]. Figure 2.7 shows the line that connects the corroded pits and its projection onto longitudinal axis of the pipe.

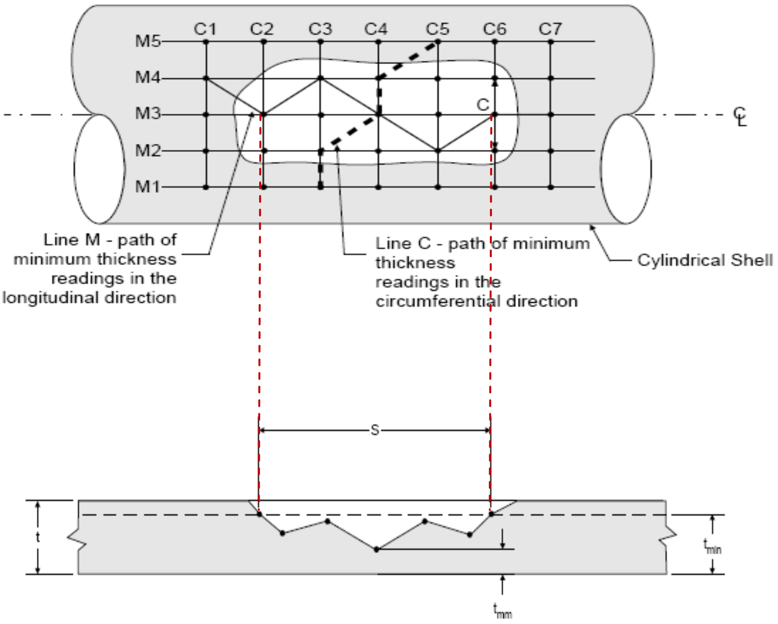

Figure 2.7 Inspection Planes and the Critical Thickness Profile [1].

2.1.3 RSTRENG

RSTRENG uses the modified form of the NG18 (equation 2.1) and it is more accurate in predicting the failure in a corrosion defect than the Modified B31G [15]. RSTRENG and the Modified B31G differ in their assumption of the projected area. The Modified B31G uses the parabolic area to calculate the remaining strength whereas RSTRENG uses the effective area. Figure 2.8 shows the difference in the projected area in both methods [4]. RSTRENG provides more accurate results than Modified B31G.

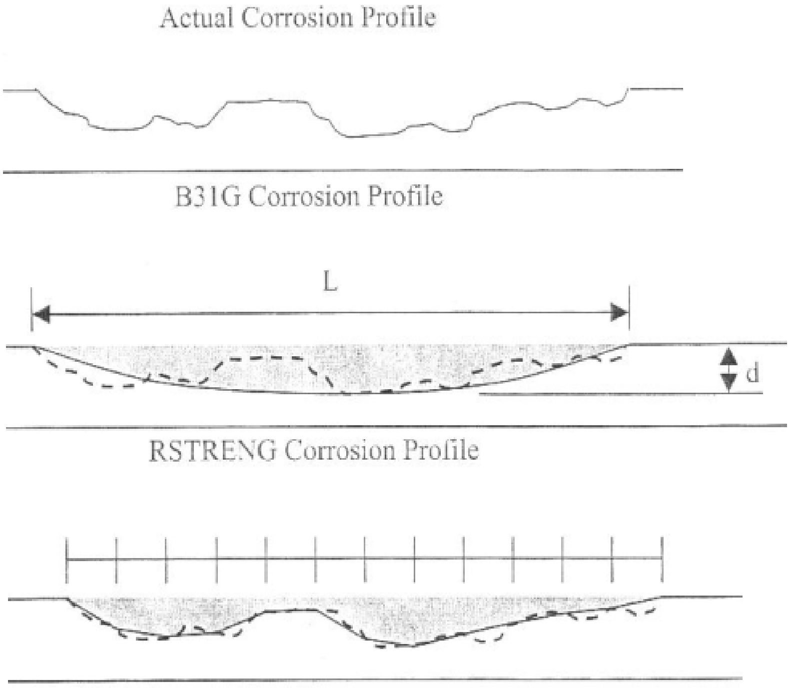

Figure 2.8 The Difference in the Projected Area in Modified B31G and RSTRENG [4].

In RSTRENG each individual measurement is assessed in combination with other corroded areas in an iterative procedure. For RSTRENG the failure pressure is calculated iteratively to predict the lowest failure pressure as follows:

$$P_f = \left(\frac{t}{R}\right)\bar{\sigma}\left[\frac{1-\dfrac{A}{A_0}}{1-\dfrac{A}{A_0}\dfrac{1}{M}}\right] \tag{2.5}$$

2.1.4 FE Modeling of Corrosion

For FEM analysis of longitudinal corroded groves in steel pipes, Mok [30] used simplified 2D and 3D models with actual defect geometry and material properties to predict the collapse pressure. The material properties were taken from tensile test data and modeled in ABAQUS using the Von Mises yield criterion and incremental plasticity (Prandtl-Reuss). The predicted results had an error of 5% compared to the experimental burst test data. To predict the collapse pressure, Mok evaluated the strains in the corrosion ligament and considered that the failure pressure occurred when the strains at the ligament started increasing in an asymptotic manner.

Several 3D elastic-plastic finite element analyses were conducted by Chouchaoui et al [31] who modeled single corrosion pits, complex electro-chemically machined flat-bottomed pits, and some natural corrosion defects of simple geometry. The material was modeled using incremental plasticity and isoparametric hybrid elements with reduced integration. The results of the FEM modeling were between -6% and 7% of the actual burst test failure pressure. The predicted results were dependent upon the mesh coarseness.

Although the coarse meshes converged, the results were conservative in predicting failure pressure. The model was considered to fail when the stress through the thickness of the corrosion ligament exceeded the ultimate tensile strength.

Several studies were undertaken by Fu and Kirkwood [32], Stephens[33], Klever [34], and Popelar[35] to understand the dependency of collapse pressure on the defect geometry and the interaction of closely spaced corrosion defects.

It was essential to specify a criterion that would assess the plastic collapse of a corrosion defect using FEM. For that reason, the strain-based criterion by Mok [30] and the stress-based criterion by Chouchaoui [31] were proposed. For this study the stress-based criterion was used.

The strain-based criterion predicts the failure pressure when the corrosion ligament gradient plastic strain increases asymptotically. On the other hand, the stress-based criterion proposed by Chouchaoui [31] considers plastic collapse when the equivalent stress through the ligament exceeds the ultimate tensile true stress. It was found by Chouchaoui that the strain-based approach provided large scatter in predicting the collapse pressure.

Another criterion was presented by Fu and Kirkwood [32] to increase the accuracy of predicting the collapse pressure of corroded pipes. They found that a critical stress state based on the true Von Mises stress at the point of necking gave more accurate results. Another alternative criterion suggested by Stephens [33] was based on the stress-strain and fracture behaviour of the material. Stephens suggested that material failure occurred when the stress reached the fracture stress, as defined by the following equations where C_1, C_2 and C_3 are material constants:

$$\varepsilon_f = \frac{C_1(CVP)^{C_2}}{\sigma_{UTS}}; \ \varepsilon_{UTS} = C_3\varepsilon_f \tag{2.6}$$

$$\sigma_{Fracture} = \sigma_{YS}\left(\frac{\sigma_{UTS}}{\sigma_{YS}}\right)^{\frac{\log(\varepsilon_f/\varepsilon_{YS})}{\log(\varepsilon_{UTS}/\varepsilon_{YS})}} \tag{2.7}$$

Leis [36] suggested that the stress-strain criterion was necessary if stable tearing in the ligament resulted in the development of the flaw. In the case of low fracture toughness materials, the flaw could result in brittle fracture before the plastic collapse.

The work of Chouchaoui [31] and Fu [32] was followed by Cronin [4] who used FEM to predict the failure pressure of complex natural corrosion defects using a critical-stress based failure criterion. The onset of collapse was predicted when the Von Mises stress at any point in the defect exceeded the ultimate tensile true strength (the critical stress). The results of burst tests on twenty-five pipe sections were modeled and the predicted of the failure pressure had an average error of -0.18%, with a standard deviation of 8.45%. However, the average error was reduced to 0.1% with a standard deviation of 4.1% when the defects were measured more accurately using a 3D scanner [4].

Both accurate defect geometry and material representation give the FEM approach an advantage over other assessment methods. Accurate defect measurement is required because the FEM is very sensitive to local changes in defect depth. Detailed material properties are also required to provide an accurate collapse pressure prediction. As a result, the FEM is considered as an accurate approach to predict failure pressure location of a corrosion defect.

It is worth noting that a transition in failure mechanism to instability-based failure could occur in the case of shallow defects (less than 20% of wall thickness). In such a case, the mode of failure changes from stress-based to geometric instability which depends on the geometry and hardening parameters of the material. Experimental testing verified [10] the geometric instability failure mechanism. The same mechanism was verified in the commercial FE code using Rik's method in ABAQUS [37] which allows for continued deformation of the model at lower loads beyond the instability limit.

2.2 Crack Defect Overview

There are several accepted codes for assessing crack defects in pipelines. Some of these use linear elastic fracture mechanics (LEFM) and others use elastic-plastic fracture mechanics (EPFM). EPFM is used instead of LEFM when significant yielding occurs in the material prior to fracture. For plain strain conditions, the maximum stress intensity is expected at the deepest point of a semi-elliptical crack. Failure in a cracked pipe usually occurs by plastic collapse or fracture depending on the material properties, defect size and loading conditions.

2.2.1 LEFM

LEFM can be used for a material with high strength where the plasticity in the vicinity of the crack tip is small [15]. The stress intensity factor K is a quantity that gives the magnitude of the elastic stress field. As the defects in this study were made in the longitudinal direction of the pipes, Fracture opening mode I loading (Figure 2.9) was the concern of this study since the hoop stress in the circumferential direction of the pipe was the highest and would cause the defect to fail. The stress intensity factor for Mode I loading was calculated using the following equation:

$$K_I = Y\sigma_m \sqrt{\pi a} \tag{2.8}$$

The geometry factor Y can be found in handbooks or codes such as the stress intensity factors handbook [15].

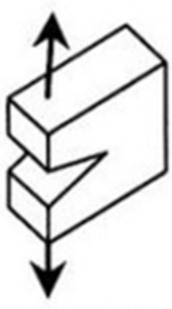

Figure 2.9 Mode I loading [19]

2.2.2 EPFM

EPFM or yielding fracture mechanics YFM is used for cracks in a ductile material when plasticity is significant at the crack tip. The fracture characterizing parameters in EPFM are the J-integral and the crack opening displacement COD. J is used to calculate the strain energy release rate around the crack tip and is a path independent integral. In two dimensions J is expressed as follows:

$$J := \int_\Gamma \left(W\, dx_2 - \mathbf{t} \cdot \frac{\partial \mathbf{u}}{\partial x_1}\, ds \right) \tag{2.9}$$

Figure 2.10 shows the J-Integral line in 2 dimensions.

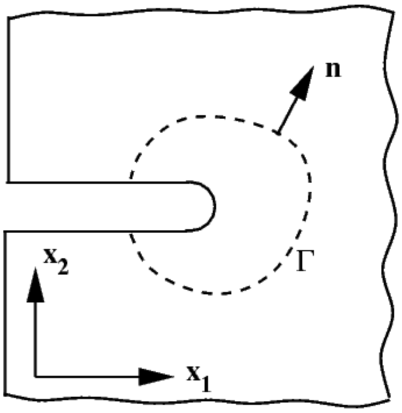

Figure 2.10 Line J-Integral around the crack tip [16],

To evaluate whether the crack defect in a pipe fails by plastic collapse or fracture, the critical fracture toughness should be used. The critical values of the fracture toughness are K_I (For LEFM) , $J_{IC,}$ or $J_{0.2}$ (for EPFM). Where J_{IC} is the critical strain energy release rate and $J_{0.2}$ is the strain energy release rate when the crack grows by 0.2mm. These material properties can be evaluated using ASTM Standard Test Method for Measurement of Fracture Toughness [18]. Note that fracture occurs when $K_I \geq K_{IC}$ and for the special case of plane strain deformation K_c becomes K_{IC}.

The J-integral can be related to K_c for LEFM by the following equation:

$$K_c = \sqrt{J_c\, E'} \qquad (2.10)$$

Where for plane strain: $E' = \frac{E}{1-\nu^2}$

The J-Integral has elastic and plastic parts according to the following equation where $J_c = J_{el}$:

$$J = J_{el} + J_{pl} \tag{2.11}$$

The additional plasticity part added to the elastic part causes the J-Integral to increases rapidly with applied stress for EPFM. This will be seen later in section 4.4.

2.3 Current Codes for Crack-Like Flaws Assessment

At present, API579 and BS7910 are the most common methods for assessing crack-like flaws in pipelines. Both methods are based on the failure assessment diagram (FAD) [20]. Also, NG-18, which is based on the Folias factor, and CorLAS software are used for assessing crack-like flaw in pipelines.

2.3.1 Failure Assessment Diagram (FAD)

The FAD approach is often applied at three different levels. These levels used for different amount of material property information. For example, LEFM for brittle fracture as well as EPFM or fully plastic collapse for ductile material can be evaluated [19]. Figure 2.11 shows the Level 1 FAD.

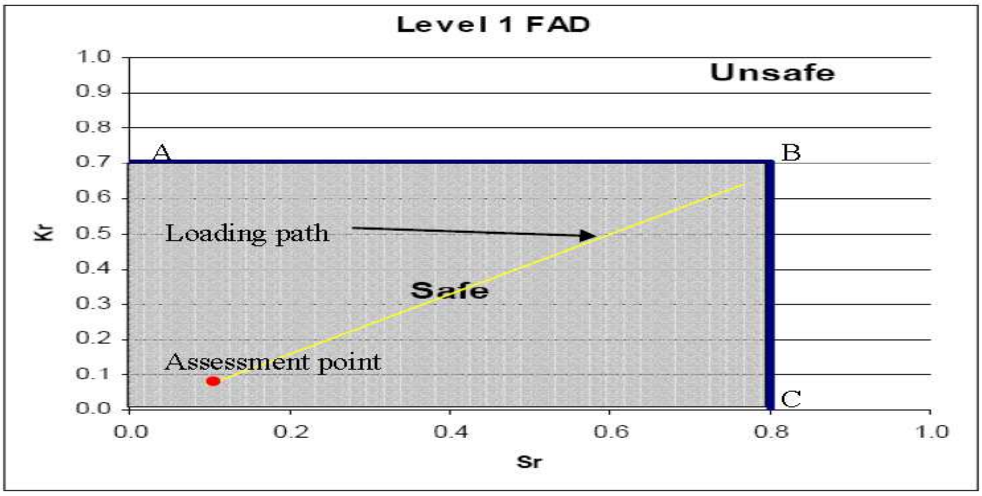

Figure 2.11 Level 1 FAD

- **FAD Level 1**

FAD level 1 (Figure 2.11) is used when information regarding the material properties or loading conditions is limited. In this case the material is assumed elastic perfectly plastic. The assessment lines are based on the relationship between the toughness ratio (K_r), and load ratio (S_r) of the component. The toughness ratio and the load ratio are given by the following two equations:

$$Toughness\ ratio \qquad K_r = \frac{K_I}{K_{Ic}} \tag{2.12}$$

$$Load\ ratio \qquad S_r = \frac{\sigma_{ref}^P}{\sigma_{flow}} \tag{2.13}$$

Where:

$\sigma_{flow} = \frac{\sigma_Y + \sigma_u}{2} \leq 1.2\ \sigma_Y$

The assessment point is considered safe if it lies in the shaded area where the toughness ratio is less than 0.707 and the load ratio is less than 0.8, otherwise the component is consider unsafe. With an increase in crack size or load, the assessment point will move along the loading path towards the unsafe line.

- **FAD Level 2**

Whereas FAD level 1 assumes that the material is elastic-perfectly plastic, FAD level 2 uses the actual material stress-strain curve providing more accurate assessment [20]. Similar to FAD level 1, if the assessment point using FAD level 2 lies in the bounded area, the component is considered safe. The following equation is used to construct the failure develop for FAD level 2 as shown in Figure 2.12.

$$K_r = (1 - 0.14\left(L_r^P\right)^2\left(0.3 + 0.7\exp\left[-0.65\left(L_r^P\right)^6\right]\right) \qquad (2.14)$$

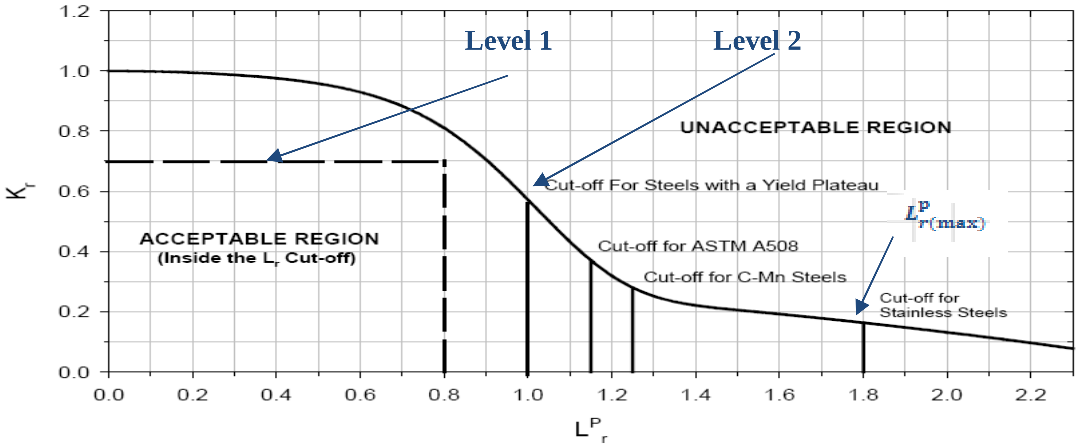

Figure 2.12 Failure Assessment Diagram Level 2 [1]

To prevent localized plastic collapse, the cut-off line $L_r^P(max)$ is calculated using the following equation:

$$L_r^P(max) = \frac{\sigma_y + \sigma_u}{2\sigma_y} \qquad (2.15)$$

- **FAD Level 3**

FAD level 3 requires the true stress-strain curve of the material (as with FAD level 2). FAD level 3 can predict whether the failure occurs by plastic collapse or by fracture. The following equations along with equation 2.13 are used construct the diagram shown in Figure 2.13.

$$K_r = [\frac{E\varepsilon_{ref}}{L_r^P\sigma_Y} + \frac{(L_r^P)^3\sigma_Y}{2E\varepsilon_{ref}}]^{-0.5} \qquad (2.16)$$

Where the references stress ε_{ref} can be taken from the true stress strain curve.

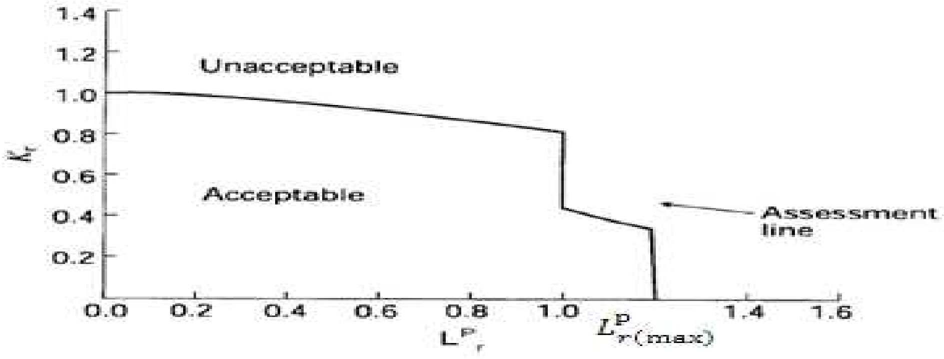

Figure 2.13 Failure Assessment Diagram Level 3 [20].

Both API579 and BS 7910 use a 3-level Fad-based approach. The difference between API579 and BS 7910 is in the procedure for calculation of the stress intensity and the reference stress, explained in Appendix A. FAD level 3 shown in Figure 2.13 is divided into three regions as shown in Figure 2.14. This can determine whether the crack fails by brittle fracture containing yield or plastic collapse.

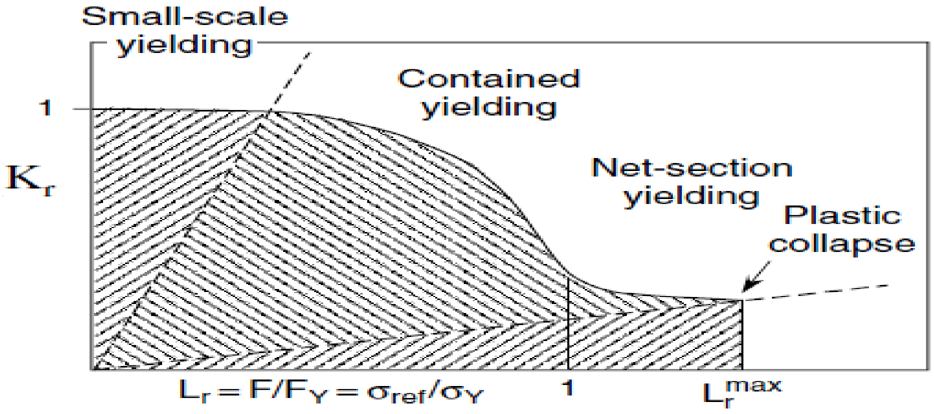

Figure 2.14 Ligament Yielding Range [40].

2.3.2 NG-18

NG-18 uses the stress and the fracture toughness based on the Charpy fracture energy Cv to calculate the collapse pressure of a pipeline containing a crack using the following equation [21]:

$$K_c^2 = (\frac{E\ C_v}{A})^2 = \frac{8}{\pi} c_{eq} \times \sigma_f^2 \times \ln \sec(\frac{\pi \times M_p \sigma_h}{2\sigma_f}) \quad (2.17)$$

Where

K_c : Fracture toughness = $\frac{EC_V}{A}$ (Joules/m^2)

σ_f : flow stress = σ_y+ 68.9 (MPa)

M_p : Bulge factor = $\frac{1-\frac{D}{t}(\frac{1}{M_t})}{1-\frac{D}{t}}$

M_t : Folias bulging factor =$\sqrt{[1+1.255\left(\frac{c_{eq}{}^2}{Rt}\right)-0.0135\left(\frac{c_{eq}{}^4}{R^2t^2}\right)]}$

To calculate the failure pressure, the following equation was used:

$$P_f=\frac{2t}{D\pi M_p}\times\sigma_f\times Cos^{-1}\left(\frac{1}{e^{\frac{E\pi C_V}{8AC_{eq}\sigma_f^2}}}\right) \qquad (2.18)$$

Where A: Fracture area of the Charpy specimen (normally 8 X 10 mm^2)

2.3.3 CorLAS

CorLAS is software developed by CC Technologies [21]. The program evaluates the residual strength of pipes with a corrosion or crack defect. CorLAS uses the J- Integral to evaluate the critical flaw size for the fracture toughness criterion in one of two ways. The first compares the applied value of J integral (J_{ap}) to the material fracture toughness (J_c). The second compares the applied tearing parameter

(dJ_{ap}/da) to the material tearing resistance (dJ/da). To determine the critical flaw size, each method requires iterative calculations [23].

2.3.4 FE Modeling of Cracks

Modeling fracture mechanics using ABAQUS requires the following background, obtained from the ABAQUS workshop (Modeling Fracture and Failure with ABAQUS) manual [7]. It is necessary to understand the important parameters used by ABAQUS to solve fracture mechanics problems, such as crack tip size, J-integral calculation, the contour integral, and the type of mesh. In order to construct the fracture problem, the material behavior -either linear or nonlinear- must be defined, and the type of fracture analysis (LEFM or EPFM) must be selected. Finally, the element size and type, the crack tip element size, and contour integral type must be defined.

2.3.4.1 FE Modeling of LEFM

For an isotropic linear elastic material, LEFM characterizes the local crack tip stress field using a single parameter called the stress intensity factor K. The stress intensity is dependent on the geometry of the specimen as well as the size and placement of the crack. It is defined from the elastic stresses near the crack tip of a sharp crack under residual stresses K, is also used to predict the stress state near the crack tip.

The stress and strain fields in the vicinity of the crack tip are expressed in terms of asymptotic series of solutions and they are valid only in a small region near the crack tip. The stress intensity factor is the parameter that relates the local crack tip fields with the global aspects of the crack problem. Equation

2.19 shows the leading order terms of the asymptotic solution where $\theta = \operatorname{atan}({}^{x2}/_{x1})$, K_I, K_{II}, and K_{III} are the stress intensity factors of the three modes, $f_{ij}^{I}(\theta), f_{ij}^{II}(\theta)\ and\ f_{ij}^{III}(\theta)$ are defining the angular variation of the stress for each mode, and r is the distance from the crack tip shown in Figure 2.15

$$\sigma_{ij}(r,\theta) = \frac{K_I}{\sqrt{2\pi r}} f_{ij}^{I}(\theta) + \frac{K_{II}}{\sqrt{2\pi r}} f_{ij}^{II}(\theta) + \frac{K_{III}}{\sqrt{2\pi r}} f_{ij}^{III}(\theta) \qquad (2.19)$$

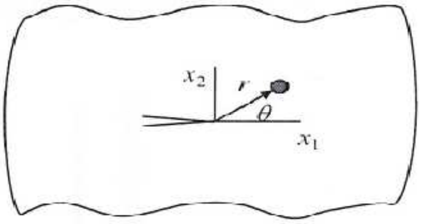

Figure 2.15 Crack Tip [7]

The predicted stress state at the crack tip possesses a square-root singularity for linear elastic (brittle) materials as shown in equation 2.20.

$$\sigma \sim \frac{1}{\sqrt{r}} \qquad (2.20)$$

It should be noted that the LEFM solution is not valid inside the plastic deformation zone if the material is modeled as elastic-plastic. The plastic zone r_P can be estimated in the LEFM asymptotic solution, where σ_o is the yield stress, by the following equation:

$$r_P \approx \frac{1}{2\pi} \left(\frac{K_I}{\sigma_o}\right) \qquad (2.21)$$

LEFM predicts infinite stress at the crack tip, which is unrealistic but the results could be used if the region of inelastic deformation near the crack tip is small enough that there is a finite zone outside this region where the LEFM asymptotic solution is accurate. In general, the effect on the elastic field surrounding the plastic zone becomes negligible at ~3r_P [7].

The crack tip in LEFM must be modeled as sharp crack. A sharp crack is used when small strain analysis is appropriate, such as in LEFM. In this case the singularity at the crack requires special attention depending on the material behavior.

The stress at the crack tip is large as it approaches the tip so the finite element mesh must be refined in the vicinity of the crack tip in order to predict accurate stresses and strains. For LEFM problems, accurate J-Integral values can be obtained with coarse meshes even though the local stress and strain fields are not very accurate.

2.3.4.2 J-Integral Evaluation

The J-Integral is used in rate-independent quasi-static fracture analysis to determine the energy release associated with crack growth. J can be related to the stress intensity factor for linear materials as follows:

$$J = \frac{1-\nu^2}{E} K_I^2 \quad For\ plane\ strain \tag{2.22}$$

$$J = \frac{K_I^2}{E} \quad For\ plane\ stress \tag{2.23}$$

Γ is the contour for J and should fall entirely within the annular region where K fields dominate shown in Figure 2.16.

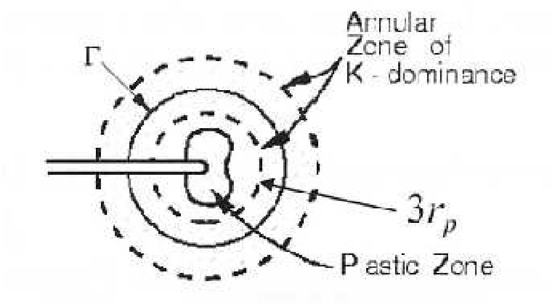

Figure 2.16 Plastic Zone and K-dominance

J values are more accurate if some singularity is included at the crack tip mesh since the stress and strain fields in the crack tip region will be more accurate. The small-strain singularities are $\varepsilon \ \alpha \ r^{-1/2}$ for linear elasticity, $\varepsilon \ \alpha \ r^{-1}$ for perfect plasticity, and $\varepsilon \ \alpha \ r^{-n/(n+1)}$ for power-law hardening material.

To capture the singularity using an 8-node isoparametric element, one side should be collapsed (e.g. nodes a,b, and c in Figure 2.17) so that all three nodes have the same geometric location at the crack tip. The midside nodes should be moved to the ¼ point nearest the crack tip. If node a,b, and c are free to move independently, then: $\varepsilon \rightarrow \frac{A}{r} + \frac{B}{\sqrt{r}}\ as\ r \rightarrow 0$ everywhere in the collapsed element. By contrast, if node a,b, and c are moving together, then A=0 and the stresses and strains are square-root singular which is suitable for linear elasticity. If node a,b, and c are free to move independently and the midside nodes remain at the midsides, then B=0 which responds to the perfectly plastic case.

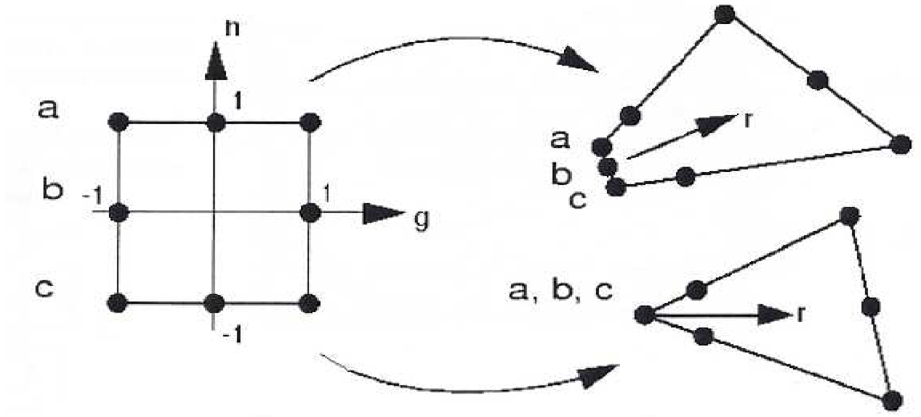

Figure 2.17 8-Nodes Isoparametric Element at Crack Tip [7]

Numerical evaluation of the J-Integral requires the crack geometry, definition of the crack front and identification of the crack extension direction. The J-integral is evaluated using a domain integral for reasons of accuracy. The domain is evaluated over an area, for two-dimensional problems, and volume, for three dimension problems, contained within a contour that surrounds the crack tip or crack line. ABAQUS defines the domain in terms of rings of elements surrounding the crack tip in two-dimensional analysis. In three dimensions, a tubular surface is defined that surround the crack line to define the domain as shown in Figure 2.18.

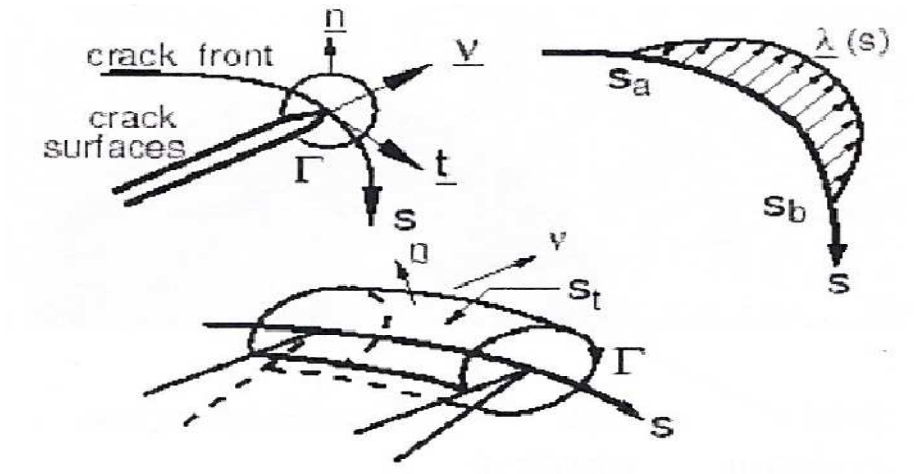

Figure 2.18 Contour Integral [7]

The crack direction, q vector, must be chosen carefully so that q is parallel to the crack surface as shown in Figure 2.19 A. If the crack direction q were not parallel to the crack surface then the first contour will not contain all the crack tip nodes as shown in Figure 2.19 B. Therefore, the J-integral from the contours could be affected by the crack extension direction. Another method used in the case of semi-elliptical cracks where the crack line is not uniform, is to specify the normal surface of the crack n.

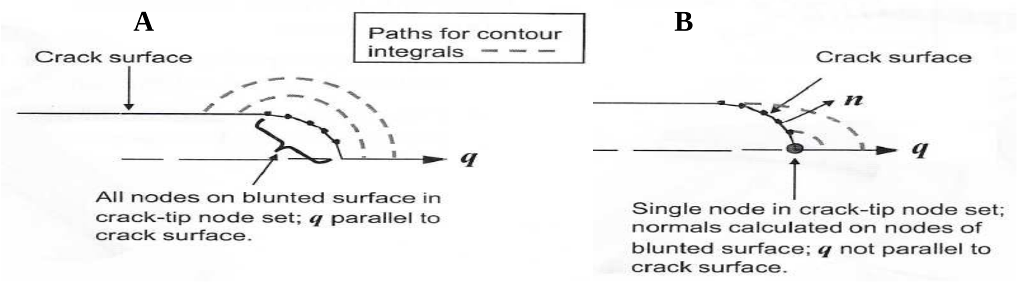

Figure 2.19 Crack Extension Direction [7]

ABAQUS creates different contours (domains) automatically. The first contour has the crack front and one layer of elements that surround it. The second contour consists of the ring of elements in contact with the first contour elements and first contour as well. The next contour is defined by adding the next ring of elements in contact with the previous contour. The first contour value is generally not used because it is not accurate [7]. The crack tip contours for EPFM problems, blunt crack (notch), are shown in Figure 2.20.

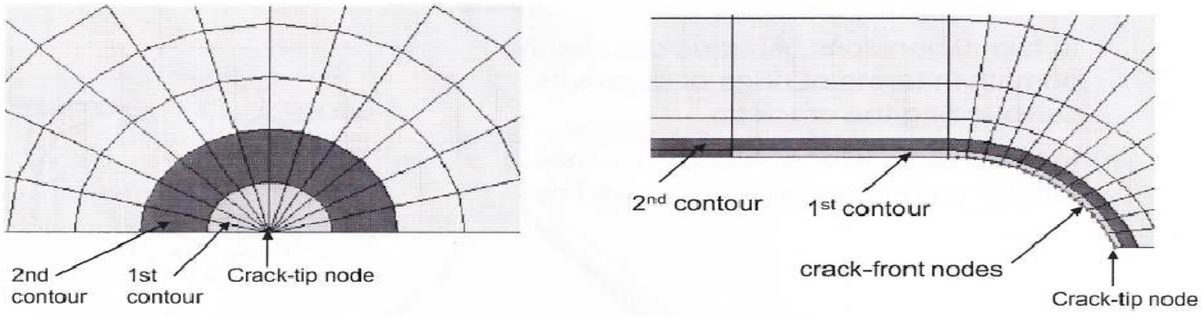

Figure 2.20 Blunt crack Tip and the Contours [7]

2.3.4.3 Nonlinear Fracture Mechanics or EPFM

The theory is based on nonlinear elastic material [7] instead of elastic-plastic material model. Consider a material that has a power-law hardening form:

$$\frac{\varepsilon}{\varepsilon_o} = \alpha \left(\frac{\sigma}{\sigma_o}\right)^n \tag{2.24}$$

Where σ_o is the effective yield stress, $\varepsilon_o = \sigma_o/E$ is the associated yield strain, E is the Young's modulus, and α and n are chosen to fit the stress-strain field data for the material. Figure 2.21 shows the behavior of the nonlinear elastic material that ABAQUS uses to represent the elastic-plastic materials.

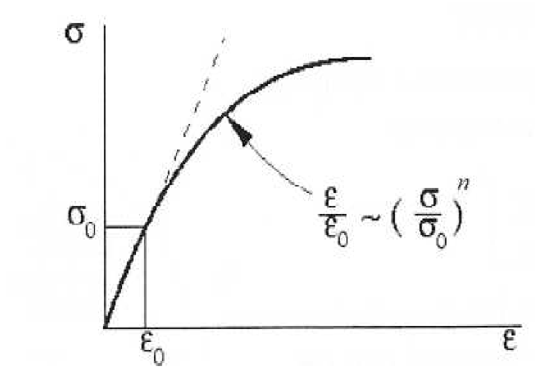

Figure 2.21 Nonlinear Elastic Material Behavior

This way the non linear elastic material behavior can be equivalent to elastic-plastic material behavior under monotonic loading. Thus, when the elastic-plastic material is subjected to monotonic loading, evaluating the J values will allow for characterizing the strength of the singularity in the crack tip region. This approach is used to model the results given on chapter 5.

2.3.4.3.1 Finite-Strain Analysis of Crack Tip

For plasticity (EPFM), the crack tip region has to be modeled carefully to give accurate results. For example, the crack tip radius and crack tip element size should be small and the size is determined from the fracture toughness and the plastic zone size. A crack can be modeled in ABAQUS as blunted crack or notch which is used for finite strain analysis for ductile materials. In this case there is no singular behavior at the crack tip. The radius of the notch should be $10^{-3}r_P$ [7]. The notch radius must be small enough so that the deformed shape of the notch no longer depends on the original geometry under applied loads. For this to be true, the notch must blunt out to more than four times its original radius. The element size around the notch must be about 1/10th the notch radius as shown in Figure 2.22.

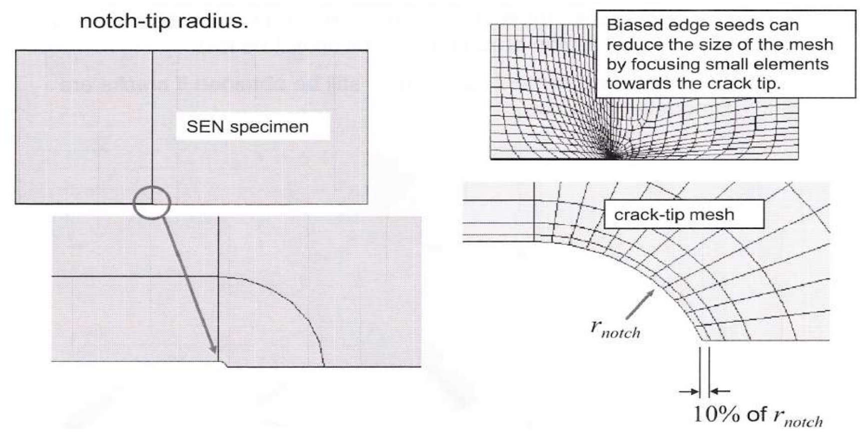

Figure 2.22 Element Size at the Notch Tip Radius [7]

Singular elements should not be used for finite-strain analysis. In addition, the mesh must be sufficiently refined to avoid numerical problems when evaluating the J-integral and to be able to model the high strain gradients around the crack tip if the details in this region are required.

2.3.4.4 Element Type

Plastic deformation is considered incompressible for Von Mises plasticity. As the plastic deformation starts to dominate the response, the rate of total deformation becomes incompressible (constant volume). All quadrilateral and brick elements are suitable for use in J-integral evaluation to handle this incompressibility condition except for the fully integrated quadrilaterals and brick elements without the hybrid formulation. Some elements such as CPE8 and C3D20 will become over constrained (lock) as the material becomes more incompressible. In contrast, second-order elements with reduced integration such as CPE8R and C3D20R, which was used in this study, work best for crack tips in particular. A regular pattern of deformation in the displaced shape plot is a sign of mesh locking. A change to reduced integration elements from fully integrated elements or refining the mesh density if using reduced integration elements may solve the locking problem. The elastic-plastic materials are more sensitive to meshing than for small-strain linear elasticity.

Chapter 3 Experimental Testing

This chapter summarizes a series of rupture tests done by Hosseini [9] on several seam-welded pipe sections to investigate the failure behavior of a pipe containing longitudinal defect. The tests were carried out by making either artificial corrosion, crack, or CIC defects of different depths in several end-capped pipe sections. Each experiment was modeled using finite element method in Chapter 5 and the results were compared to the experimental results of this chapter.

3.1 Corrosion Defect Experimental Data

Three artificial corrosion defects were created in the longitudinal direction of the pipe by machining a rectangular groove with rounded corners to avoid stress concentrations [9]. Each defect length was 200 mm, and the depths were 22%, 45%, and 61% of the wall thickness. Figure 3.1 shows the corrosion defect dimensions while Figure 3.2 shows the tested pipe.

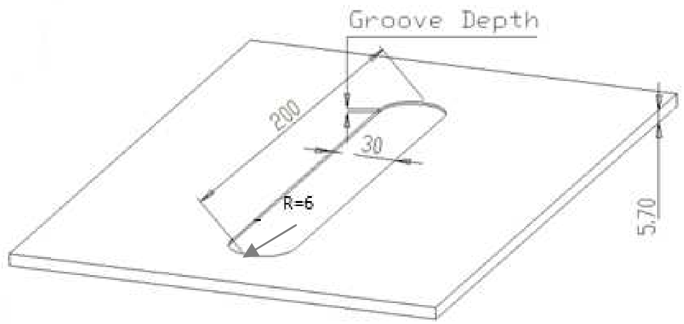

Figure 3.1 Corrosion Defect Dimensions

Figure 3.2 Burst Test of The 61%WT Corroded Pipe [9]

Hosseini used the analytical methods modified B31G and RSTRENG to predict the failure pressure before the test. The experimental and analytical results are summarized in Table 3.1 and Figure 3.3. These results will be used to validate the corrosion modeling results in Chapter 5.

Table 3.1 Experimental and Analytical Failure Pressure Results in Corroded Pipe [9]

Test ID	**Experimental Failure Pressure (MPa)**	**Predicted Burst Pressure**		$\mathbf{Error}(\%) = \frac{\mathbf{Experimental} - \mathbf{Predicted}}{\mathbf{Experimental}} \times \mathbf{100}$	
		RSTRENG (MPa)	**MB31G (MPa)**	**RSTRENG**	**MB31G**
C1	12.8	9.47	9.73	26.0	24.0
C2	9.59	7.10	8.25	26.0	14.0
C3	6.0	5.51	6.54	8.0	-9.0
		Average Error (%)		**20.0**	**10.0**

Hosseini concluded that RSTRENG is more reliable than the Modified B31G in predicting the failure pressure [9] because RSTRENG uses a more complete description of the longitudinal geometry of the corrosion defect. In general as shown from Figure 3.3, the analytical solutions gave conservative results compared to the experimental failure pressure.

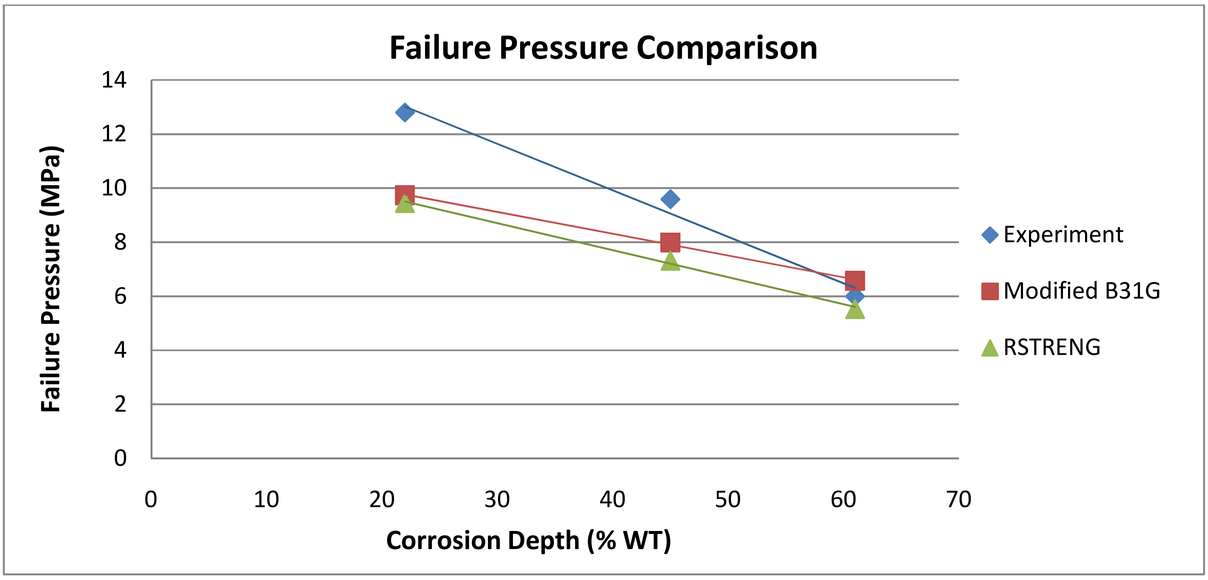

Figure 3.3 Experimental and Analytical Failure Pressure Results in Corroded Pipe [9]

As expected, the failure pressure decreases with the depth of the corrosion defect which is expected in the finite element modeling as well. In addition, Hosseini [9] observed the fracture surface of the tested pipes and concluded that the failure occurred due to plastic collapse by ductile tearing. The three corrosion defects of (22%, 45%, and 61%WT) were modeled and the results will be seen in Chapter 5.

3.2 Crack Defects Experimental Data

Four artificial crack defects were created in end-capped seam-welded pipe sections. The direction of the prefatigued cracks was made axially to investigate the behavior of a longitudinal crack defect. The semi-elliptical crack depths and geometries are given in Table 3.2, and Figure 3.4, respectively.

Table 3.2 Geometry of the Artificial Crack Defect [9]

Test ID	Pipe Dimension (mm)			Defect Dimension (mm)		Collapse Pressure (MPa)
	Length	**Width**	**Thickness**	**Length (2c)**	**Depth (a) (%WT)**	
CR1	1800	508	5.70	200	38	10.1
CR2					47	9.30
CR3					48	9.60
CR4					51	8.83

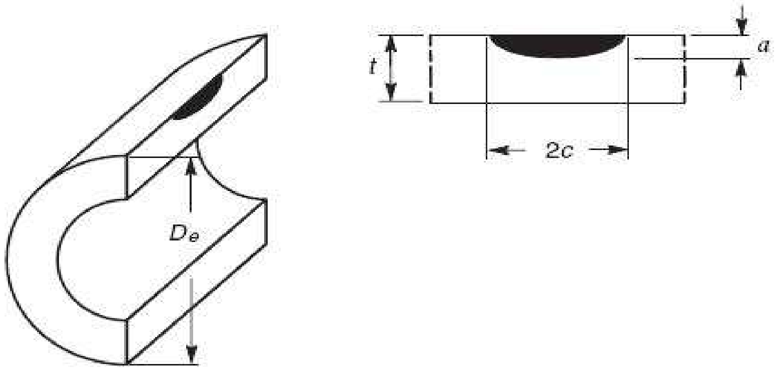

Figure 3.4 Semi-elliptical Crack Geometry [9]

Hosseini [9] used several analytical methods to predict the crack defect failure pressure. These methods were BS 7910 level 3 FAD, API 579 level 3 FAD, and NG18. Moreover, CorLAS software provided by TCPL was also used for the flaw collapse pressure investigation. Hosseini [9] showed that all the analytical solutions were conservative, and the CorLAS program provided the best failure pressure prediction agreement. The results are summarized in Table 3.3 and Figure 3.5,

Table 3.3 Failure Pressure Results in Cracked Pipe [9]

Test ID	**Crack Depth (a) (%WT)**	**Exp. Failure Pressure (MPa)**	**Predicted Failure Pressure (MPa)**				$\mathbf{Error}(\%) = \frac{\mathbf{Exp.} - \mathbf{Pred.}}{\mathbf{Exp.}} \times \mathbf{100}$			
			API 579 Cylinder	**BS7910 Cylinder**	**CorLAS**	**NG-18**	**API 579 Cylinder**	**BS7910 Cylinder**	**CorLAS**	**NG-18**
CR1	38	10.1	8.10	5.80	8.48	7.10	20.0	43.0	16.0	30.0
CR2	47	9.30	7.10	4.62	7.69	6.30	24.0	50.0	17.0	32.0
CR3	48	9.60	6.86	4.45	7.58	6.20	29.0	54.0	21.0	35.0
CR4	51	8.83	6.21	3.97	7.24	5.90	30.0	55.0	18.0	33.0
				Average Error (%)			**25.0**	**50.0**	**18.0**	**33.0**

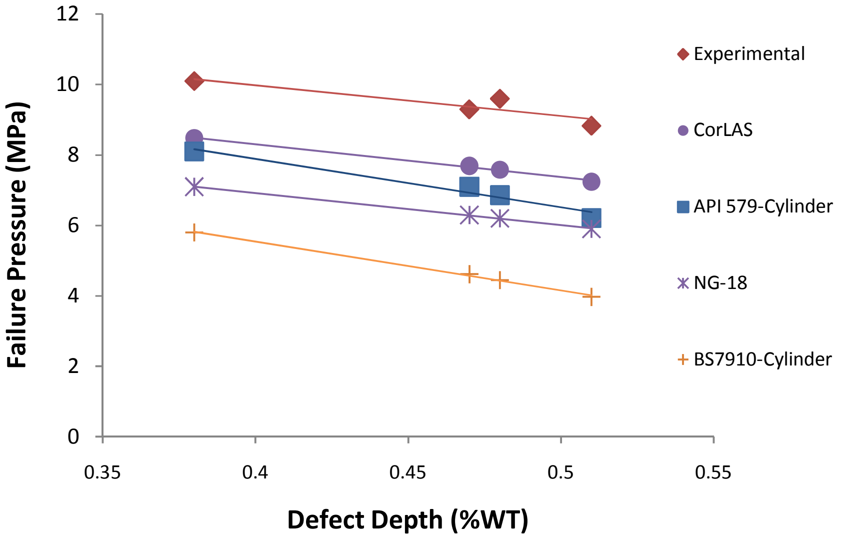

Figure 3.5 Experimental and Analytical Failure Pressure Results in Cracked Pipe [9]

API 579 level 2 FAD cylinder approach was less conservative than the other analytical methods in predicting the collapse pressure because of using the bulging factor (M) directly in the stress intensity factor solution. According to Hosseini [9], the crack defects (38%, 47%, 48% and 51%WT) failed by plastic collapse and this results were verified by examining the fracture surface after the rupture test. Moreover, Hosseini [9] stated that in some cases the failure mode started as plastic collapse and continued with ductile tearing, or vice versa. The four cracks of (38%, 47%, 48%, and 51%WT) were modeled in Chapter 5 to simulate the burst test.

3.3 Crack-in-Corrosion (CIC) Experimental Data

Five CIC experiments were undertaken by Hosseini [9]. The pipes were seam-welded with end-caps and the direction of the defects was in the axial direction. The CIC defect was prepared by first machining a longitudinal slit in the pipe, and then initiating and propagating a fatigue crack from the slit. A rectangular groove, similar to corrosion defect was then machined over the crack as shown in Figure 3.6. The geometries of the CIC defects are given in Table 3.4.

Table 3.4 Geometry of Tested Pipes for Crack-in-Corrosion Defects [9]

Test ID	**Corrosion & Crack Length (mm)**	**Corrosion Width(mm)**	**Defect Depth**		**Total Defect Depth (%WT)**
			Crack (%)	**Corrosion (%)**	
CIC1	200	30	32	68	52
CIC2			38	62	59
CIC3			34	66	60
CIC4			30	70	61
CIC5			35	65	66

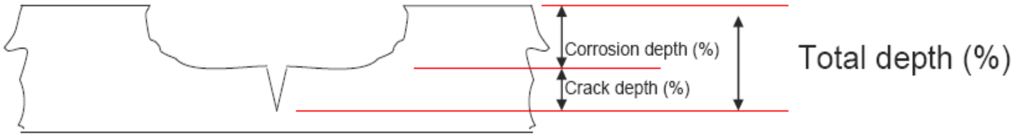

Figure 3.6 Transverse View Through CIC Flaw and Definition of Depth [9]

A numerical study by Cronin and Plumtree [43], stated that the failure pressure results of the CIC defects, where intermediate between those of a long uniform crack and a long uniform corrosion defect. Therefore, Hosseini [9] used the analytical solution to predict the failure pressures of the CIC defects based on the following two assumptions [9]:

1-The CIC defect was treated as a crack defect of equivalent depth.

2-The CIC defect was treated as a corrosion defect of equivalent depth.

API 579 level 3 FAD cylinder approach provided the best analytical method for assessing the crack-like flaws and RSTRENG provided the best results for evaluating the corrosion defects [9]. Therefore, both methods were used to evaluate the CIC failure pressure data. In addition CorLAS software was also used since it provided the least conservative prediction of crack defects. The results of the experiments and the analytical prediction are summarized in Table 3.5 and Figure 3.6.

Table 3.5 Experimental and Analytical Failure Pressure Results in CIC Defected Pipe [9]

Test ID	**Total Defect Depth (% WT)**	**Exp. Failure Pressure (MPa)**	**Predicted the Failure Pressure of Equivalent Defect (MPa)**			$\mathbf{Error}(\%) = \frac{\mathbf{Exp.} - \mathbf{Pred.}}{\mathbf{Exp.}} \times \mathbf{100}$		
			Crack Only		**Corrosion Only**	**Crack Only**		**Corrosion Only**
			Level 3 FAD API 579-Cylinder	**CorLAS**	**RSTRENG**	**Level 3 FAD API 579-Cylinder**	**CorLAS**	**RSTRENG**
CIC1	52	7.74	6.15	7.21	6.55	21.0	7.0	15.0
CIC2	59	6.72	4.89	6.48	5.75	27.0	4.0	14.0
CIC3	60	7.06	4.75	6.45	5.63	33.0	9.0	20.0
CIC4	61	7.89	4.45	6.43	5.51	44.0	19.0	30.0
CIC5	66	6.15	3.73	5.93	4.91	39.0	4.0	20.0
				Average Error (%)		**33.0**	**8.0**	**20.0**

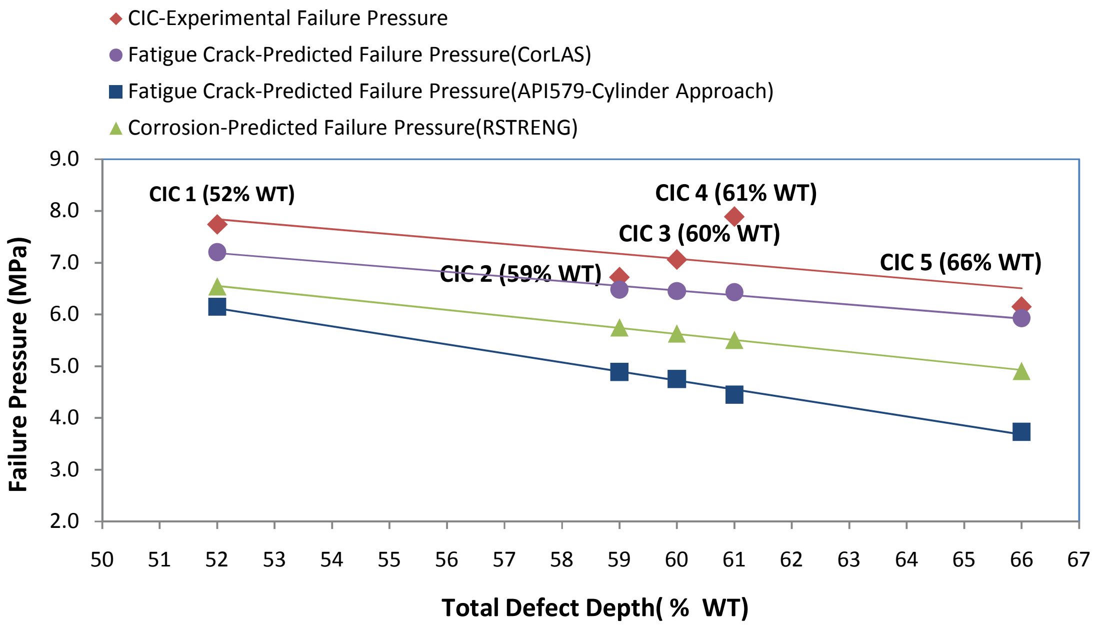

Figure 3.7 Experimental and Analytical Failure Pressure Results in CIC Defected Pipe [9]

In Figure 3.7 Hosseini [9] show that all the used methods provided conservative results for an equivalent CIC defects. CorLAS predictions of the CIC defect collapse pressure were more accurate than API 579 level 3 FAD Cylinder approach and RSTRENG. It also shows that the crack, as expected is more critical than the corrosion. The results of Hosseini’s experimental results are summarized in Figure 3.8

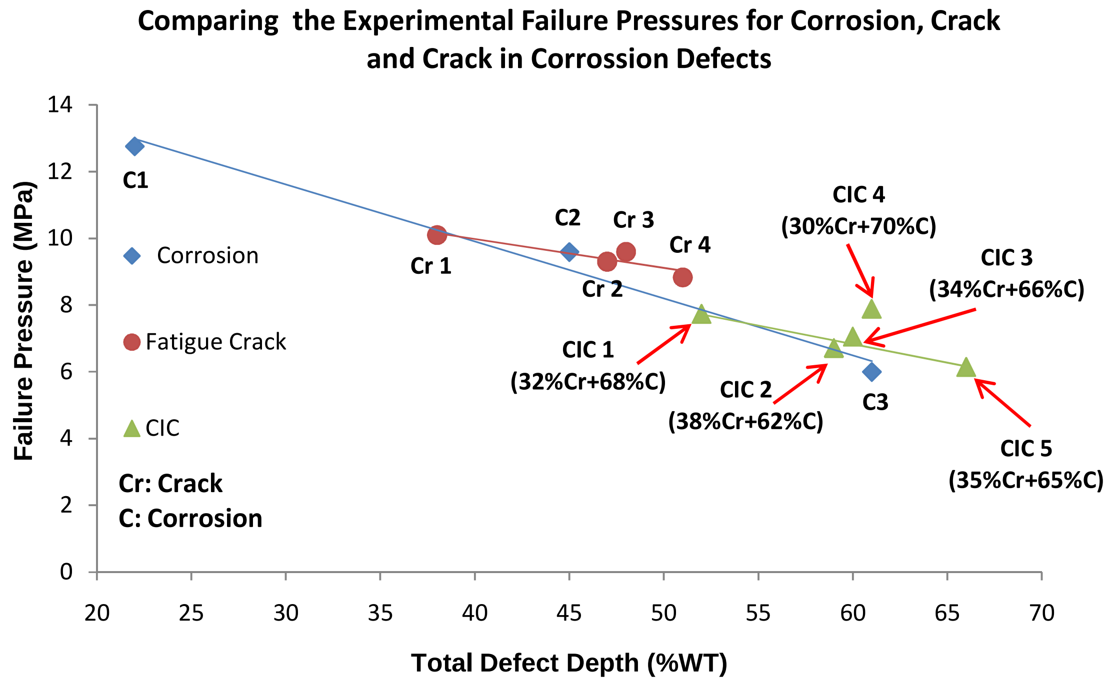

Figure 3.8 Experimental Summary of Corrosion, Crack, and CIC Defects [9]

According to experimental results in Figure 3.8, the CIC defect collapse pressure fell in between crack defect only (upper bound) and corrosion defect only (lower bound). Usually, the crack defect is more critical than the corrosion defect of the same depth. Apparently, from Figure 3.8 the corrosion defects were more critical than the crack defects. This is due to the fact that the corrosion defects were made as blunt defect with uniform depth were as the crack defects were made as semi-elliptical cracks. In addition to the difference in defects profiles, the corrosion defects have more removed material in the width than the crack defects [9]. Based on Hosseini's [9] observation of the fracture surface of the tested pipe with CIC defect, the failure occurred by plastic collapse.

Chapter 4 Material Characterization

In order to evaluate the integrity of the pipe, it is important to know the material properties. Once the appropriate failure criteria have been identified, the material properties are also required to conduct the modeling. Tensile, Charpy and J-Integral tests were conducted by the author according to the ASTM standards to obtain the required information.

4.1 Tensile Testing

The tensile test provides engineering stress-strain curves that are used to determine the true strength and the plastic strain behaviour of the pipe material. True stress-strain can be evaluated up to necking assuming constancy of volume. Twenty four tensile test specimens were cut from several pipe sections because the material properties could vary along the pipe line from one section to another. Since the longitudinal and circumferential strengths may differ in the pipes, specimens were cut in both directions. The first set of tests contains three longitudinal and three circumferential specimens taken from one pipe section. The rest of the test specimens (eighteen specimens) were taken from three different pipe sections and were paired with Charpy testing.

Twelve longitudinal and twelve circumferential tensile test specimens were prepared and tested according to the ASTM standard [24]. The tensile test specimen dimensions were 5.7 mm thickness, and 12.5 mm width, with a gage length of 60 mm, as shown in Figure 4.1. The Young's Modulus of Elasticity was assumed to be 207 GPa. The test results are given in Table 4.1 and Table 4.2 for the longitudinal and circumferential tensile test specimens, respectively.

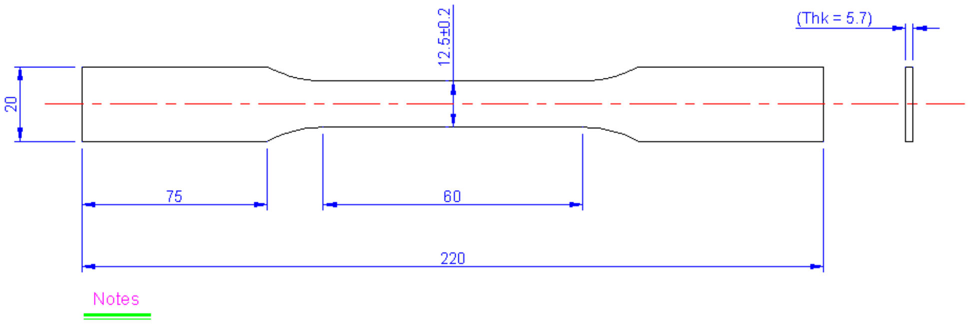

1. All dimensions are in (mm).

Figure 4.1Tensile Test Specimen Dimensions

Table 4.1 Longitudinal Tensile Test Results

Longitudinal Direction						
Specimen ID	**σ_Y (0.2 % Offset)**		**σ_Y (0.5 %)**		**σ_{Uts} (Eng. Stress)**	
	(MPa)	**(psi)**	**(MPa)**	**(psi)**	**(MPa)**	**(psi)**
L1	343	49748	361	52359	549	79626
L2	348	50473	362	52504	546	79191
L3	341	49458	356	51633	544	78900
L4	363	52649	380	55114	563	81656
L5	357	51778	380	55114	571	82817
L6	363	52649	381	55259	551	79916
L7	343	49748	361	52359	544	78901
L8	362	52504	376	54534	545	79046
L9	355	51488	372	53954	553	80206
L10	374	54244	387	56130	555	80496
L11	349	50618	365	52939	554	80351
L12	362	52504	383	55549	552	80061
Average	**355**	**51488**	**372**	**53954**	**552**	**80097**

Table 4.2 Circumferential Tensile Test Results

Circumferential Direction						
Specimen ID	**σ_Y (0.2 % Offset)**		**σ_Y (0.5 %)**		**σ_{Uts} (Eng. Stress)**	
	(MPa)	**(psi)**	**(MPa)**	**(psi)**	**(MPa)**	**(psi)**
C1	480	69618	483	69908	568	82381
C2	445	64542	449	65122	560	81221
C3	454	65992	460	66717	563	81656
C4	413	59928	430	62395	579	83977
C5	424	61524	435	63091	569	82526
C6	394	57171	409	59320	565	81946
C7	407	59057	419	60771	549	79626
C8	384	55720	398	57725	539	78175
C9	398	57751	411	59611	545	79046
C10	430	62395	448	64977	590	85572
C11	423	61379	434	62946	557	70198
C12	394	57171	418	60626	561	81366
Average	**421**	**60988**	**433**	**62777**	**562**	**81511**

Note that the average longitudinal $\sigma_{Y(0.2\%)}$ was 355 MPa, 17 MPa lower than $\sigma_{Y(0.5\%)}$, and the average circumferential $\sigma_{Y(0.2\%)}$ was 421 MPa, 12 MPa lower than $\sigma_{Y(0.5\%)}$. The circumferential strength results were averaged and used in this study because the hoop stress in the pipe was higher, and has been shown to be an appropriate value for assessment conservative approach. As recommended by the CSA [25], the 0.5% circumferential stress-strain values were used.

The true stress and true strain were calculated using the following equations assuming constancy of volume, up to necking:

A. True stress:

$$\sigma_{\mathrm{T}} = \sigma_{\mathrm{Eng}}\,(1 + \mathrm{e}) \tag{4.1}$$

B. True strain:

$$\varepsilon_T = \ln\,(1 + e) \tag{4.2}$$

Figure 4.2 represents the true stress-strain curve of the circumferential tensile test results. Some tensile data show initial negative strains because the specimens were initially curved and on testing, straightening took place causing the extensometer to record negative values [42]. As previously mentioned, the circumferential tensile test data were used to determine the plastic properties of the material which were determined by applying the Ramberg-Osgood equation as follow:

$$\varepsilon = \varepsilon_e + \varepsilon_p \tag{4.3}$$

$$\varepsilon = \frac{\sigma}{E} + \alpha\left(\frac{\sigma}{\sigma_{Ys}}\right)^n (\frac{\sigma}{E}) \tag{4.4}$$

Where n is the strain hardening coefficient and α is the strength coefficient. Both were determined from fitting the equation to the experimental data.

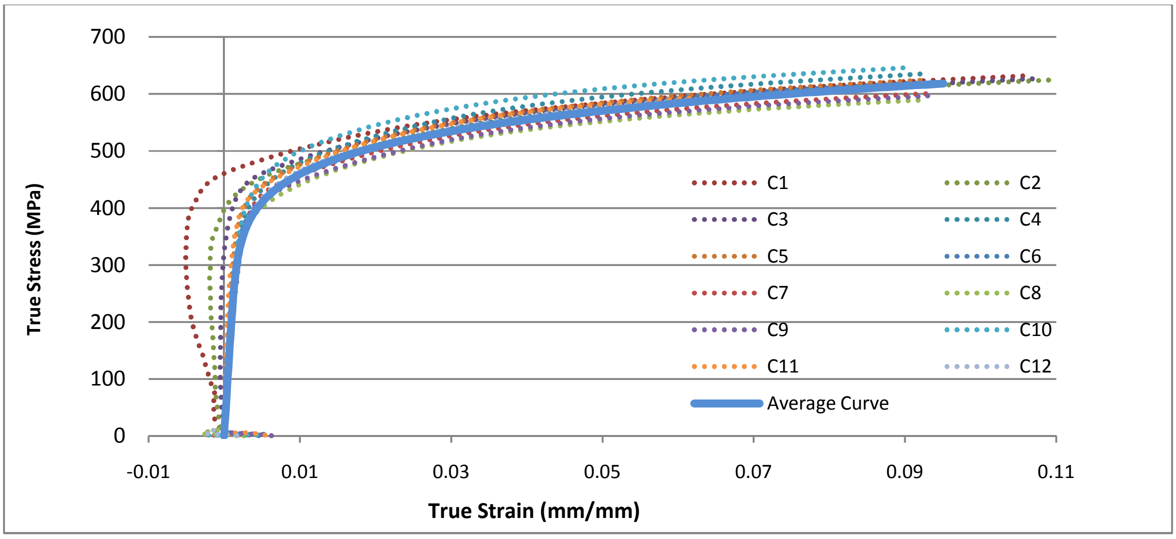

Figure 4.2 True Stress-Strain Curve for all Circumferential Tensile Test Samples

As shown in Figure 4.3, a power law curve was used for the plastic portion of the true stress-strain curves, up to the ultimate tensile strength.

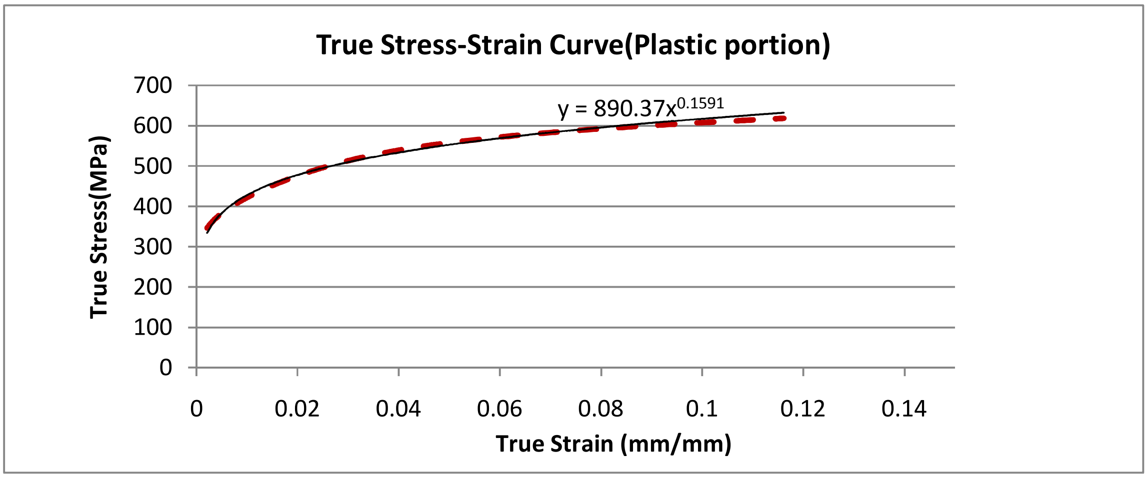

Figure 4.3 Exponential Curve Fitting to the True Stress-Strain Curve (C2)

Table 4.3 presents the calculated ultimate true tensile strength (the true stress at UTS) along with the strain hardening and strength coefficients for all the circumferential tensile tests and the average values were used to plot Figure 4.4.

Table 4.3 True Stress and Ramberg-Osgood Material Parameters - Circumferential Direction

Specimen Id	**Ultimate tensile stress (True Stress)**		**α**	**n**
	(MPa)	**(psi)**		
C1	631	91519	1.85	9.85
C2	624	90503	1.75	8.55
C3	626	90794	1.80	10.81
C4	635	92099	2.41	5.63
C5	625	90649	2.37	8.01
C6	620	89923	2.52	6.37
C7	603	87458	2.49	8.34
C8	592	85862	2.59	7.26
C9	599	86878	2.52	7.19
C10	646	93694	2.32	5.25
C11	591	85717	2.38	8.74
C12	615	89198	2.48	4.18
Average	**618**	**89524**	**2.29**	**7.31**

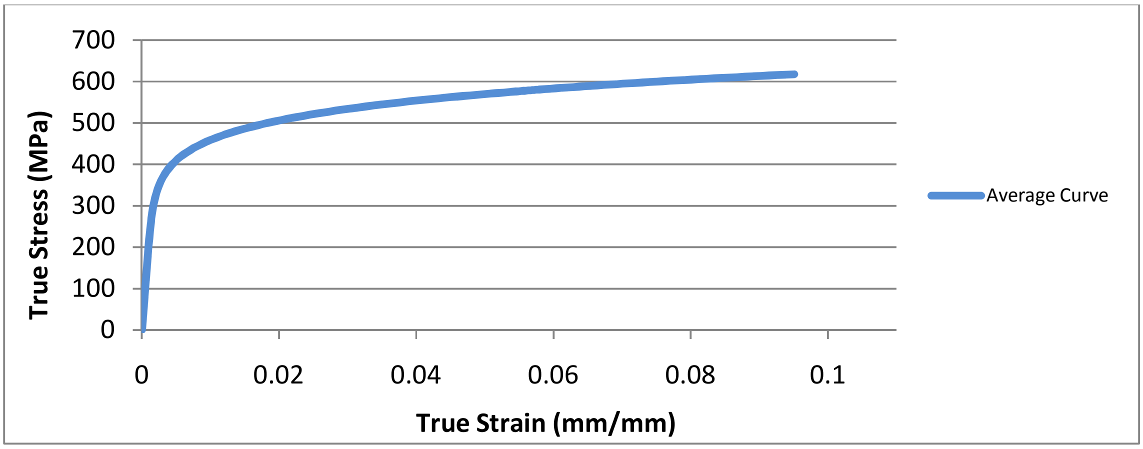

Figure 4.4 Average True Stress Strain Curve in Circumferential Direction

The average, maximum, minimum and standard deviation of the 12 tensile test samples carried out in each direction are given in Table 4.4. The most important properties for the modeling analysis were the ultimate true stress in the circumferential direction, the average true stress-strain curve, n, and α**.**

Table 4.4 Summary of The Tensile Test Results

	AVG	Max	Min	±STDEV
Longitudinal Tensile test result of 12 samples				
Yield stress σ_y (0.5%) (MPa)	372	387	356	10.07
Engineering ultimate σ_u (MPa)	552	571	544	8.08
Ultimate True σ_u (MPa)	608	625	591	9.65
Circumferential Tensile test result of 12 samples				
Yield stress σ_y (0.5%) (MPa)	433	483	398	24.2
Engineering ultimate σ_u (MPa)	562	590	539	14.1
Ultimate True σ_u (MPa)	618	646	591	17.6
α (equation 4.4)	2.29	4.39	1.75	0.82
n (equation 4.4)	7.31	9.85	4.18	1.67

The difference between the circumferential and longitudinal yield stress σ_y (0.5%) was 61 MPa. In general the circumferential strength of the pipe was greater than the longitudinal strength. Note that the yield strength of the circumferential tensile test had a large variation with a standard deviation of 24.2. This is due to the curved specimens which were flattened before testing.

4.2 Charpy V-notch Test

Two sets of CVN tests were undertaken according to ASTM standard [42]. The first test was conducted to determine the transition temperature and the upper shelf energy for the steel. 54 sub-sized specimens were tested from one pipe section that had a 5.7 mm wall thickness. The recommended full size specimen thickness is 10 mm but since the pipe thickness was smaller, sub-size samples of 5mm and 3mm thickness were machined, and some were flattened. The dimensions of the sub-sized CVN^S specimens are shown in Figure 4.5.

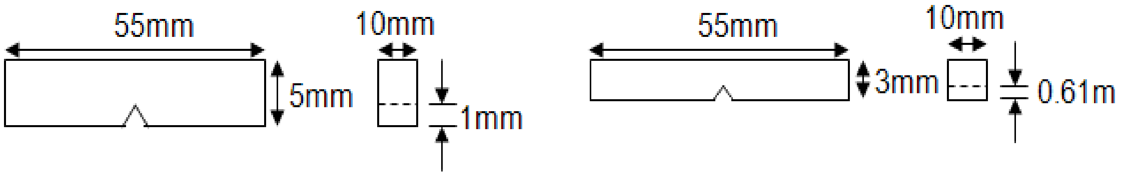

Figure 4.5 Sub-Size Specimen Dimensions for Charpy Test [42].

In addition, non-flattened samples of 3 mm thickness were also prepared and tested for comparison with the flattened samples in order to account for any discrepancies that could arise from to the flattening process. The tests were carried out at temperatures of -60°C, -40°C, -20°C, 3°C, 22°C, and 100°C to determine the ductile-brittle transition temperature. Furthermore, to evaluate any variation in the upper shelf energy, a second set of CVN^S tests was conducted to determine the upper shelf average energies of three other pipe sections. Therefore, another 54 sub-sized specimens from the three different pipe sections were tested at temperatures of 50°C, 100°C, and 150°C.

Table 4.5 Non Scaled Charpy Test Results

Temperature (°C)	**(CVN^S) Average Energy E (J)**		
	T=3mm Flattened	**T=3mm Non-Flattened**	**T=5mm Flattened**
150	N/A	11.0	26.0
100	12.0	12.0	25.0
50	N/A	11.0	24.0
22	14.0	13.0	19.0
3	12.0	9.00	16.0
-20	10.0	9.00	15.0
-40	8.00	8.00	7.00
-60	6.00	7.00	3.00

The sub-size specimens have less cross-sectional area which results in less energy absorption [24]; However, the energies can be scaled to the full size specimen using the following equation from API 579 [26]:

$$\mathrm{CVN} = \mathrm{CVN}^S\left(\frac{t_c}{t_c^S}\right) \tag{4.5}$$

The scaled CVN results are given in Table 4.6.

Table 4.6 Scaled Charpy Test Results

Temperature (°C)	(CVN) Average Energy E (J)		
	T=3mm Flattened	T=3mm Non-Flattened	T=5mm Flattened
150	N/A	37.0	52.0
100	41.0	39.0	49.0
50	N/A	37.0	49.0
22	47.0	44.0	38.0
3	40.0	40.0	32.0
-20	32.0	31.0	29.0
-40	26.0	27.0	15.0
-60	19.0	24.0	6.00

The CVN energy-temperature chart in Figure 4.6 summarizes the scaled test results. The Boltzmann function was used to fit a sigmoidal curve that identified the transition temperature and the upper shelf average energy. Equation 4.6 gives the function used in fitting the results:

$$Energy = \frac{-29.67}{1 + e^{\frac{T+22.9}{18.09}}} + 43.44 \tag{4.6}$$

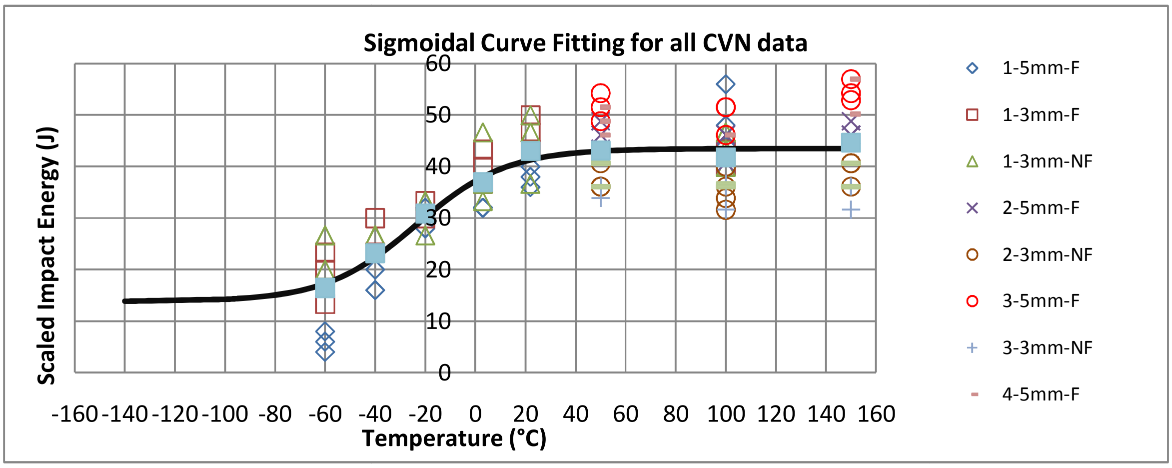

From the energy-temperature chart in Figure 4.6, the transition temperature was calculated to be -22.9°C. Scatter in the data may be due to two reasons.

a) Depend on the side where the notch was made in flattened specimen.

b) The scatter was magnified on scaling up the energy results to 10mm full size specimen.

The fracture surfaces of the CVN specimens were examined and the amount of shear fracture percentage was determined according to ASTM [24]. The results are shown in Table 4.7 and Figure 4.7, respectively. 100% shear fracture indicates fully ductile fracture and 50% ductile fracture corresponds to the transition temperature. From Table 4.7 the shear fracture percentage for the 5mm flattened specimens reached 50% at -20°C. In addition, the shear fracture percentage for the 3mm flattened specimens reached 50% between -20 and -40°C while for the 3mm non-flattened specimens, the 50% shear fracture percentage was close to -20 °C.

Table 4.7 Shear Fracture Percentage Results

Specimen Size (mm)	**T=5mm Flattened**	**T=3mm Flattened**	**T=3mm Non- Flattened**
Temperature (°C)	**Percent Shear %**		
150	100.0	100.0	100.0
100	100.0	100.0	100.0
50	90.0	100.0	100.0
22	90.0	90.0	100.0
3	70.0	90.0	86.7
-20	50.0	80.0	46.7
-40	10.0	30.0	20.0
-60	0.00	0.00	10.0

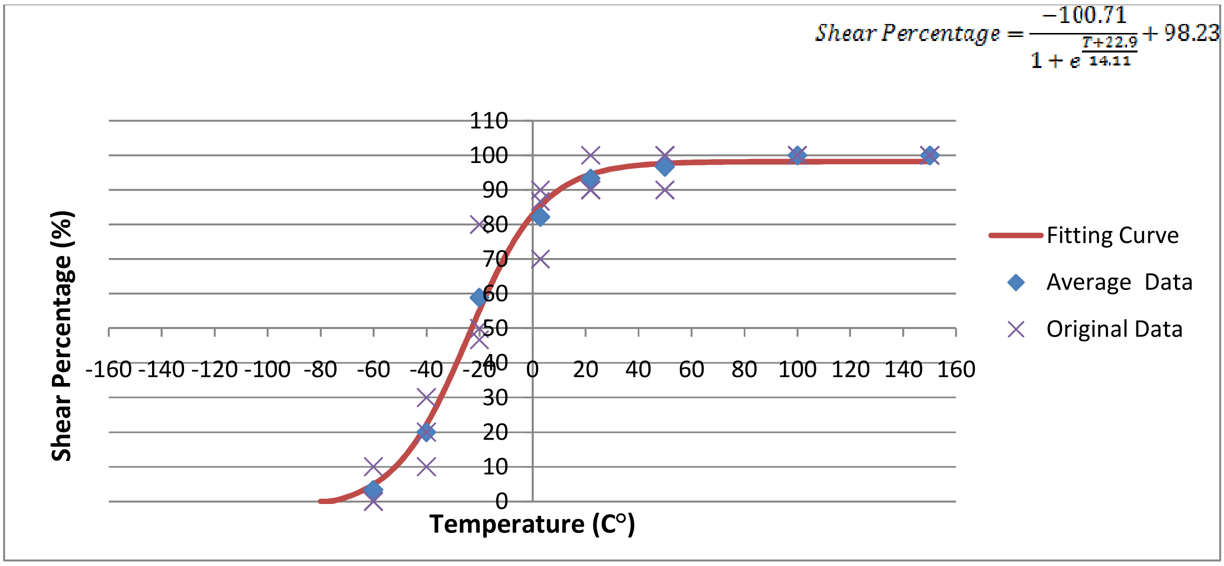

Figure 4.7 Percent Shear Fracture Chart

Figure 4.7 shows that the 50% observed ductile shear occurred at -22.98°C which agrees with a transition temperature of -22.9˚C found using the sigmoidal curve in Figure 4.6. A summary of the Charpy test results is given in Table 4.8.

Table 4.8 Summary of Charpy V-notch Test Results

Upper shelf Average energy E (J) Figure 4.6	**Lower Shelf Average Energy E (J) Figure 4.6**	**Transition Temperature, DBTT(°C) Figure 4.6**	**Average Percent Shear (%) at -22.98 (°C) Figure 4.7**
43.5	16.3	-22.9	50

4.3 Fracture Toughness Empirical Evaluation

Fracture toughness is defined as the ability of a cracked material to resist fracture. The evaluation of the fracture toughness provides an estimated value that can be used to determine the crack notch radius and the failure pressure in modeling the crack and CIC defects. There are several methods to convert the CVN energy to an equivalent fracture toughness. The relationships to convert CVN energy to K_{IC} or $J_{0.2}$ are empirical and have been developed over the past years by several groups. Tyson [27] provided three relations to convert CVN energy to K_{IC} as seen, for upper shelf energy of 43.5 J, in the digitized Figure 4.8 which were 147, 122, and 116 J. In addition, Mak and Tyson [28] have also developed empirical correlations to calculate $J_{0.2}$ using CVN energy seen in Figure 4.9 (96 J for an upper shelf energy of 43.5 J) and Figure 4.10 (113, 97, and 77 J for an upper shelf energy of 43.5 J), respectively. The three empirical evaluations (Figure 4.8- Figure 4.10) were carried out to give an initial average estimation of the fracture toughness value for the material under investigation. Moreover, in the absence of the fracture toughness value for old pipes, the empirical evaluation was the only way to estimate fracture toughness.

Mak and Tyson investigated the material properties of eight different pipes manufactured from 1952 to 1981. The pipes grades were X52, X65, and X70 and the thickness of the pipes ranged from 7.9 to 12.7 mm and all of the pipes exhibited ductile tearing on the reported CVN upper shelf energies given in Table 3.8 were used in the figures of Mak and Tyson given in Figure 4.8, Figure 4.9and Figure 4.10 to estimate the fracture toughness. Note that the pipe in this work had a 5.7 mm wall thickness (less than the pipe for the Mak and Tyson study) and was considered a thin-wall pipe. Therefore, the results in Figures 3.8-3.10 are just an approximation of the actual fracture value.

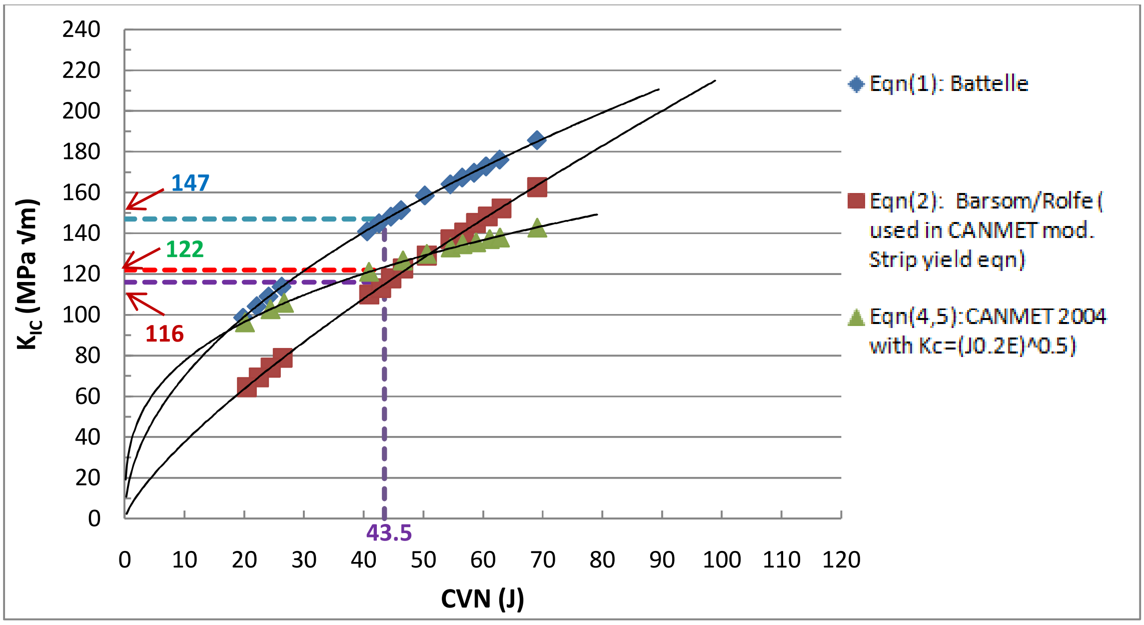

Figure 4.8 CVN Vs. K_{IC} Tyson [27].

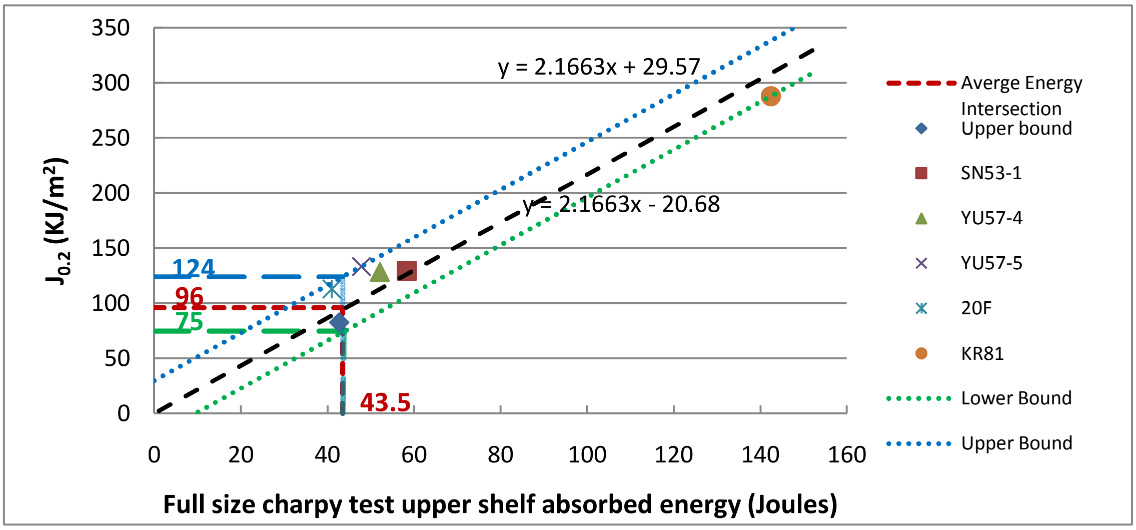

Figure 4.9 CVN Vs. $J_{0.2}$ Mak & Tyson [28].

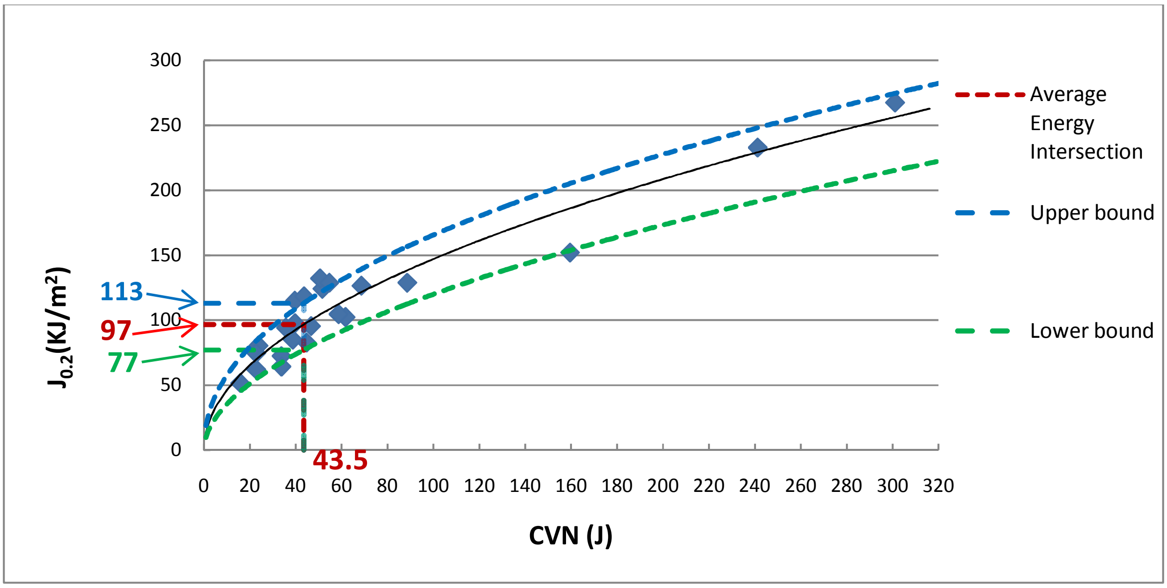

Figure 4.10 CVN Vs. $J_{0.2}$

The results of the previous correlations in Figure 4.8, Figure 4.9, and Figure 4.10 are averaged and summarized in Table 4.9.

Table 4.9 Empirical Conversion of CVN Energy to K_{IC} and $J_{0.2}$

Method	**CVN upper shelf average energy (Joules)**	**Average K_{IC} (MPa$\sqrt{m}$)**	**Average $J_{0.2}$ (KJ/m^2)**
Tyson	43.5	128 (16.4)	
Mak & Tyson			97 (19.5)
			95.7 (18)

The numbers in brackets give the standard deviation. These empirical results were most useful because the result of K_{IC} = 128 $MPa\sqrt{m}$ was used later to estimate the crack tip radius for the crack and CIC models. Moreover, based on the results of J-Integral testing in section 4.4, the empirical values of $J_{0.2}$ in, Table 4.9, prove to be very conservative when compared to the measured value.

4.4 J-Integral Test

J-Integral testing was conducted to evaluate the fracture toughness by determining the J_{IC} or $J_{0.2}$ of the steel under investigation. J-Integral tests according to ASTM [18] were carried out on three different pipe sections by BMT Fleet Technology Company [29]. BMT used single edge bend specimens (SEB). The specimen thicknesses were 5.3 mm for the first test set, 5.12 mm for the second, and 5.33 mm for the third. The differences in thickness resulted from machining specimens that contained varying amounts of corrosion. The specimens were prepared with the crack on the outer pipe diameter in the longitudinal direction. According to ASTM, the specimens were pre-cracked by fatigue [18] and then a load was applied and crack extension was measured. BMT Fleet Technology Company provided the curve shown in Figure 4.11 for the first test set.

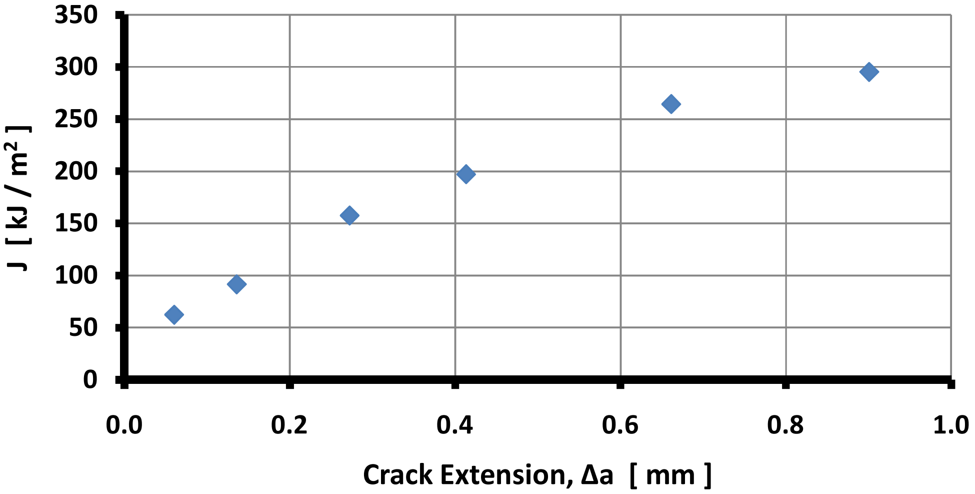

Figure 4.11 J-Integral Test Results for the First Test Set

This curve is believed to be done according to ASTM E 1820 [18] for the basic test method. BMT prefatigued the single edge specimens then they applied a load P and recorded the crack extension. Then they have used the following equations to draw J-integral versus the crack extension in Figure 4.11.

J integral was calculated as follows:

$$J = \frac{K^2(1-\nu^2)}{E} + J_{pl} \tag{4.7}$$

$$J_{pl} = \frac{\eta_{pl} A_{pl}}{B_N b_0} \tag{4.8}$$

Where: η_{pl}= 1.9 if the load-line displacement is used forA_{pl}, = 3.667 − 2.199(ao /W) + 0.437(ao /W)2 if the crack mouth opening displacement record is used for A_{pl}.

$$K_{(i)} = \left[\frac{P_i S}{(BB_N)^{1/2} W^{3/2}}\right] f(a_i/W) \tag{4.9}$$

$$f\left(\frac{a_i}{W}\right) = \frac{3\left(\frac{a_i}{W}\right)^{1/2}\left[1.99 - \left(\frac{a_i}{W}\right)\left(1 - \frac{a_i}{W}\right)\left(2.15 - 3.93\left(\frac{a_i}{W}\right) + 2.7\left(\frac{a_i}{W}\right)^2\right)\right]}{2\left(1 + 2\frac{a_i}{W}\right)\left(1 - \frac{a_i}{W}\right)^{3/2}} \tag{4.10}$$

Appendix A contains the analytical procedure and results for tests of J-Integral tests. A summary of the analytical procedure for the first test was carried out according to ASTM [18]. First, the crack extension was corrected using the following equation

$$J = Jel_o + \frac{Jpl_o}{1 + \left(\frac{\alpha - 0.5}{\alpha + 0.5}\right)\frac{\Delta a}{bo}} \tag{4.11}$$

A power law curve was then fitted and the exponential value of the new curve was used as m the J-R curve exponent according to the following equation:

$$J = Jel_o + \frac{Jpl_o}{1 + \left(\frac{\alpha - m}{\alpha + m}\right)\frac{\Delta a}{bo}} \tag{4.12}$$

The capacity and the limit of the specimen (J_{max} and Δa_{max}) were calculated using the following equations:

$$J_{max} = b_o \sigma_Y / 10 \tag{4.13}$$

$$J_{max} = B \sigma_Y / 10 \tag{4.14}$$

$$\sigma_Y = \frac{\sigma_{ys+}\,\sigma_{uts}}{2} \tag{4.15}$$

$$J_{limit} = b_o\sigma_Y/7.5 \tag{4.16}$$

$$\Delta a_{max} = 0.25b_o \tag{4.17}$$

$$J_{max} = b_o\sigma_Y/10 \tag{4.18}$$

Finally, the J-R curve was constructed showing the qualification area to evaluate J_{IC}, seen in Figure 4.12. The qualification region is the area defined by Δa_{min}, $\Delta a_{limit,}$ and $J_{limit.}$ To be acceptable for $J_{IC,}$ the J-R curve has to have at least five data points inside the qualification region. As a result of the analysis according to ASTM [18], there were fewer than five data points in the qualification area for all the J-Integral test sets. Figure 4.12 shows the first J-Integral test result after the analysis.

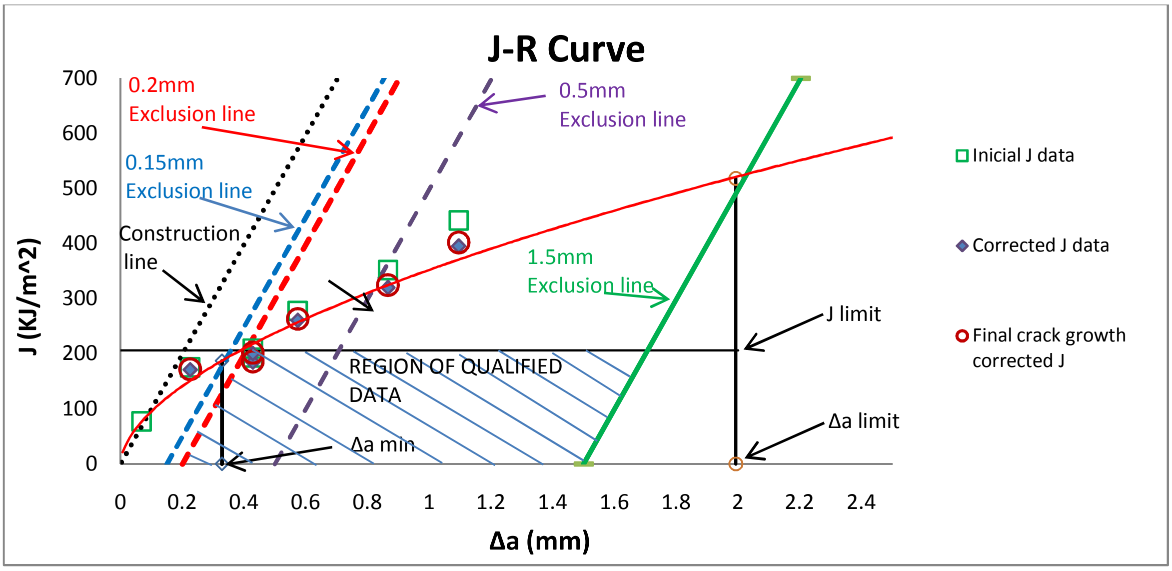

Figure 4.12 J-R Curve (First test)

The data shown in Figure 4.12 proved unsatisfactory to predict J_{IC} because the sample thickness was too small which may have caused extensive plasticity in the crack ligament since the fracture toughness value increased as the thickness decreases as shown in Figure 4.13.

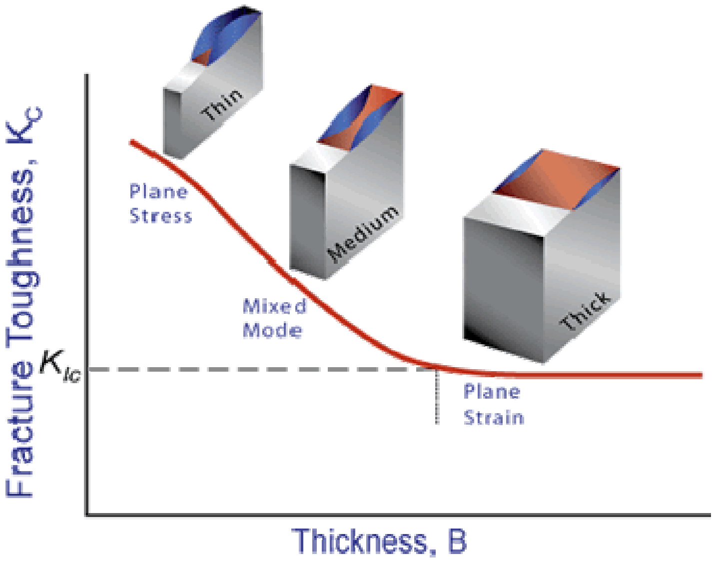

Figure 4.13 The Effect of Thickness on the Fracture Toughness [38]

However, the data was satisfactory to provide $J_{0.2}$ as a reference for the crack and CIC modeling failure criteria because $J_{0.2}$ is the value of the J after the crack has extended by 0.2 mm. Figure 4.14, Figure 4.15, and Figure 4.16 show the evaluation of $J_{0.2}$ for the three J-Integral tests. The evaluation of $J_{0.2}$ was determined from the intersection of the power fitting data curve (AB Figure 4.14) to the final corrected J data (CD Figure 4.14) with 0.2mm crack growth.

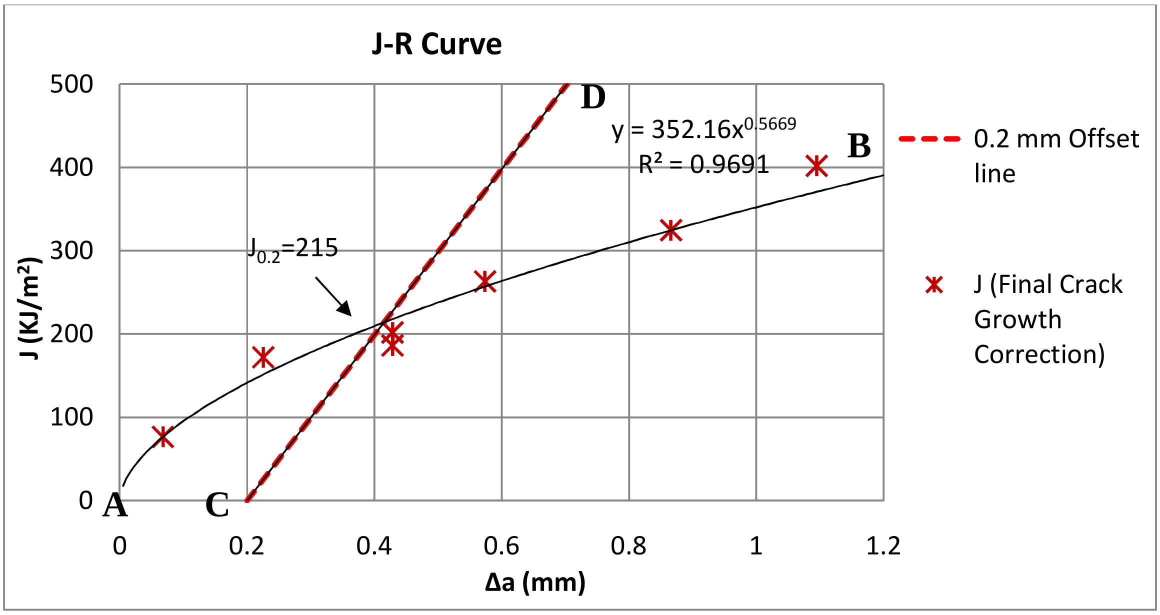

Figure 4.14 Evaluation of $J_{0.2}$ (First test)

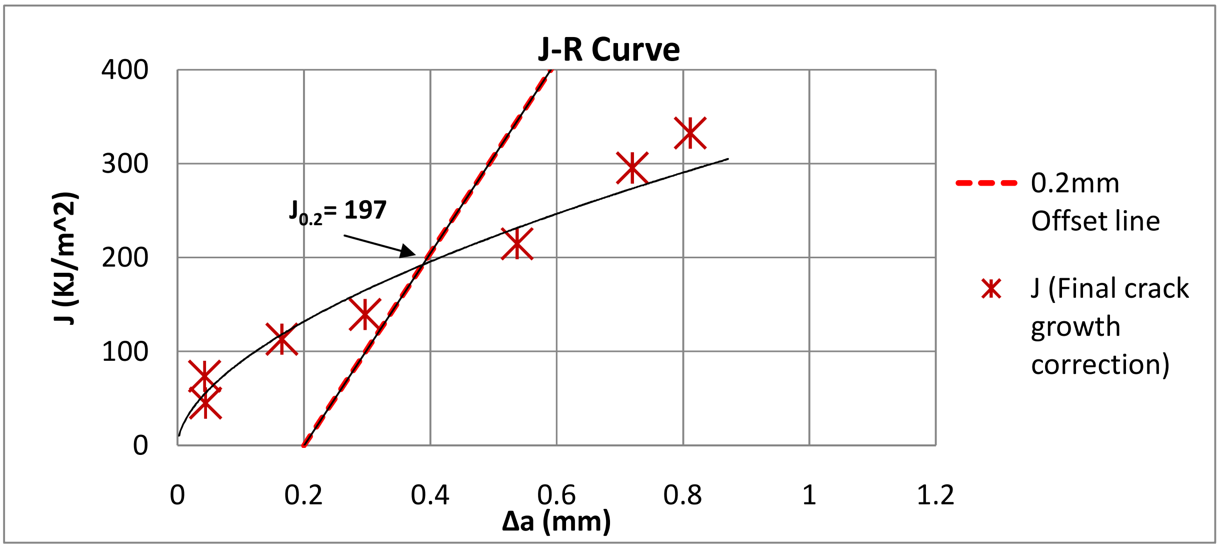

Figure 4.15 Evaluation of $J_{0.2}$ (Second test)

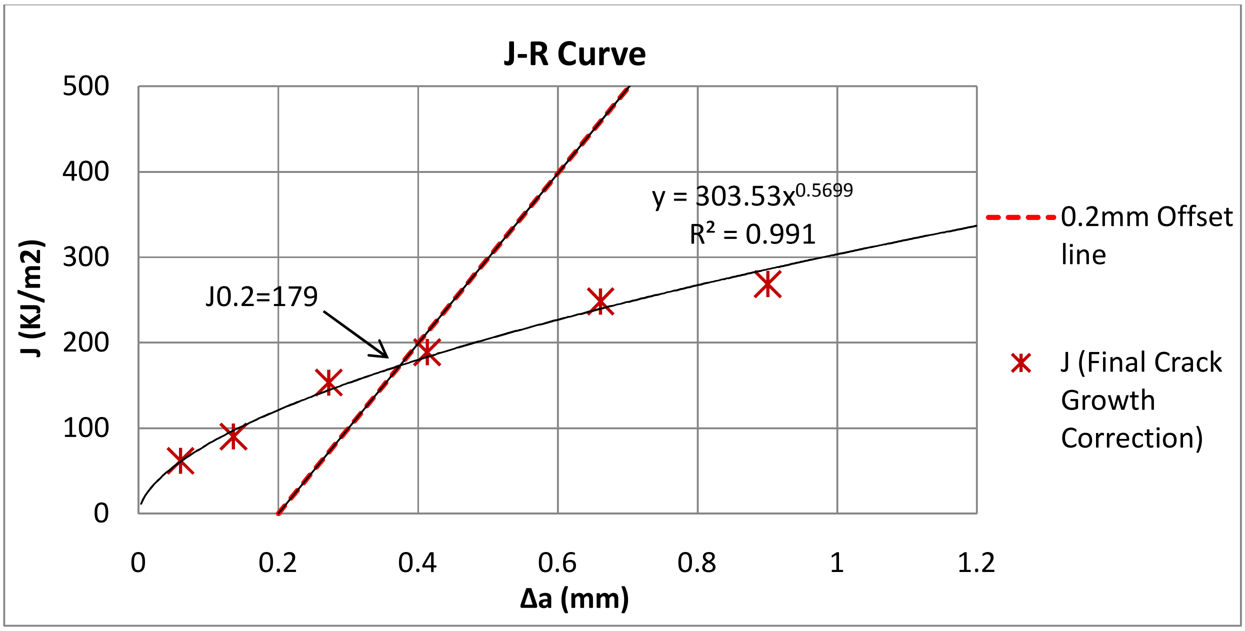

Figure 4.16 Evaluation of $J_{0.2}$ (Third test)

The final value of $J_{0.2}$ = 197 KJ/m^2 being the average of the three J-Integral tests sets values is summarized in Table 4.10. The average value of $J_{0.2}$ was used as a fracture limit in modeling crack and CIC defect.

Table 4.10 Summary of $J_{0.2}$ Results

Test Number	$J_{0.2}$ (KJ/m^2)
1	215.2
2	196.5
3	179.6
Average	**197.1**

The J-Integral testing result of 197 KJ/m^2 shows that the correlation results of $J_{0.2}$ = 97 or 95.7 KJ/m^2 given in Table 4.9 were significantly conservative for this material. The difference was expected because the pipes used by Mak and Tyson for the empirical correlation of K_{IC} and $J_{0.2}$ ranged from 7.9 to 12.7 mm which was in average twice the thickness of the pipe that was tested in this study.

Chapter 5 Numerical Analysis

5.1 Overview

The finite element method (FEM) has been used widely to investigate the prediction of collapse pressures in corrosion and crack defects. In this study the implicit finite element program ABAQUS [7] was used. For the material properties, the average of the circumferential tensile test results given in Chapter 4 was used for modeling. The appropriate boundary conditions for restraining the models were the same for all of the defects modeled. The advantage of symmetry was taken to reduce the computational time, hence only a quarter of the defected pipe was modeled. The determination of the collapse pressure was done for corrosion modeling based on the critical stress criterion.

The type of element used for the analyses was hexahedral 20-node quadratic brick, reduced integration (C3D20R) [37] to decrease the computational time. This type of element was recommended by ABAQUS [37] for 3D modeling and for large strain problems because it gave the best results in minimum time.

The material properties were introduced to the model using incremental plasticity as discussed in section 2.3.4.3. The true strain of the circumferential true stress strain curve (Figure 4.4) was determined using the Ramberg-Osgood (equation 4.4). This method of representing the material was recommended by ABAQUS [37], for proportional monotonic loading. Furthermore, since the experimental pipe had end caps, plain strain conditions were simulated to restrain the pipe from expanding or contracting in the longitudinal direction [10] as shown in Figure 5.1.

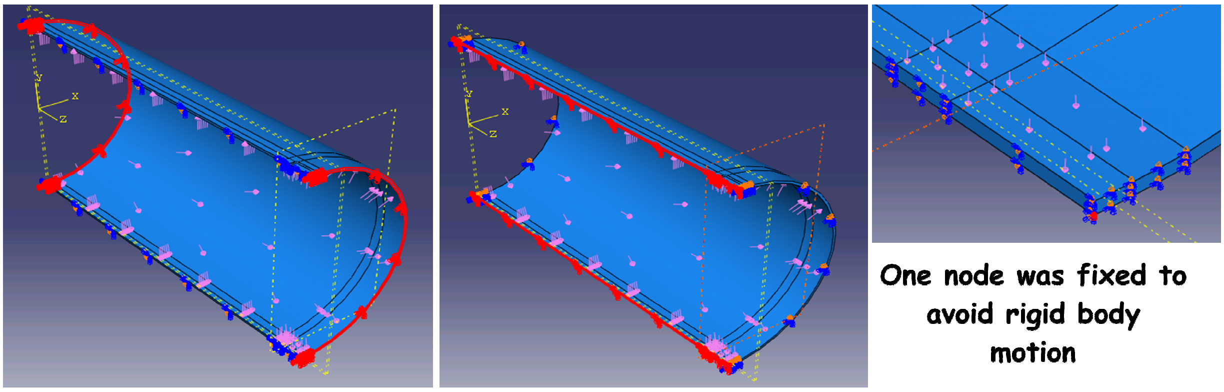

Bothe ends were symmetrically restricted in Z-direction (to simulate Plane strain)

Half walls were symmetrically restricted in X-direction

One node was fixed to avoid rigid body motion

Figure 5.1 Plain Strain Boundary Conditions

5.2 Corrosion Defect Numerical Evaluation

A set of five longitudinal aligned grooves of uniform depth were modeled using FEM to predict the failure pressure in pipes with 508mm diameter and 5.7mm wall thickness (WT). As discussed in section 2.1.4, failure initiate when the equivalent Von Mises stress at the bottom of the defect exceeds the critical stress expressed as the true ultimate tensile stress. Figure 5.2 shows the corrosion defect as modeled. Previous FE investigation by Cronin [4] concluded that two elements through the pipe thickness were sufficient to predict the failure pressure. Cronin also found that the failure pressure was relatively insensitive to the circumferential dimension of the defect because the amount of plasticity prior to failure was significant. In general, ten elements were used through the pipe wall thickness for corrosion defect modeling.

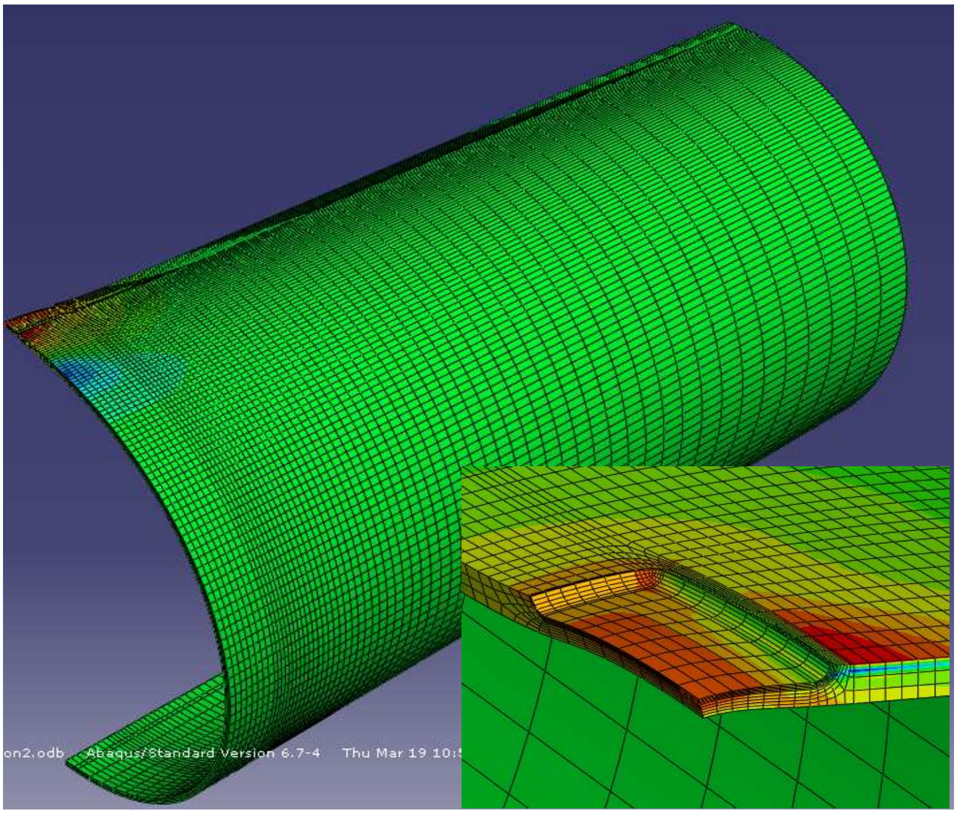

Figure 5.2 45% Corrosion Model

Five models with corrosion defects of 200mm length and depths of 22%, 30%, 45%, 61%, and 80%WT were evaluated. After modeling the problem with end caps, it appeared that adding the end caps only increases the number of elements and run time. Therefore, modeling of the end caps was neglected and the boundary conditions were applied for the case of plain strain [10]. The initiation of the failure was considered when the stress at the defect bottom reached the circumferential ultimate true stress of 618 MPa. After failure initiation, ductile tearing took place. The analyses of the corrosion modeling are shown in Figure 5.3.

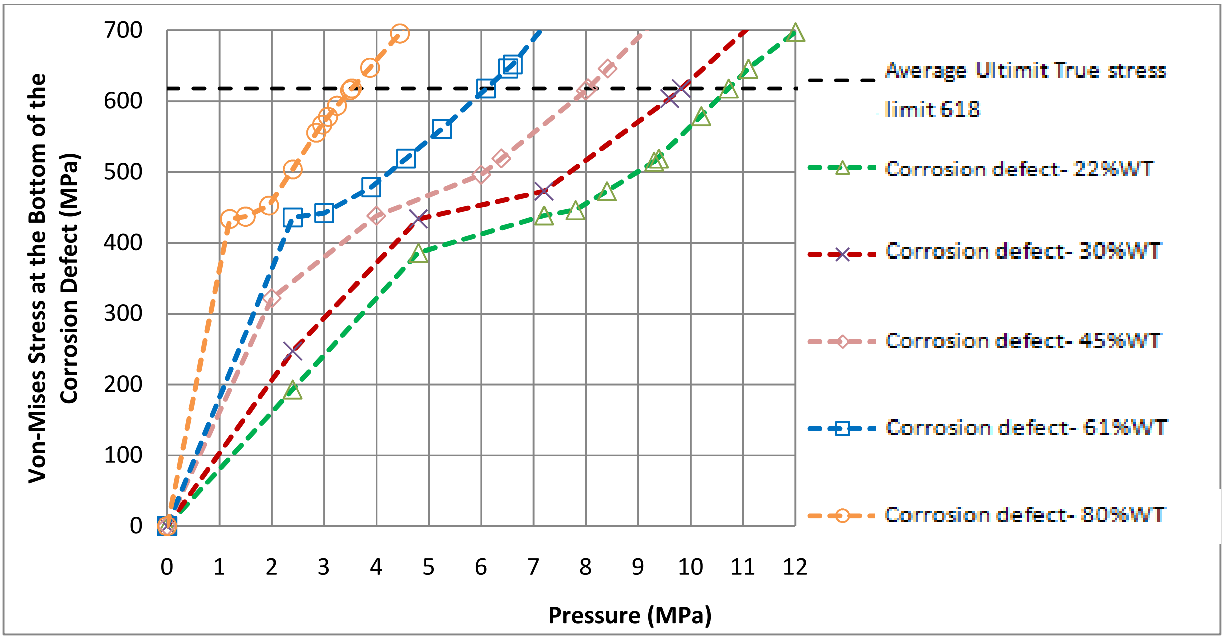

Figure 5.3 Corrosion Defect Failure Pressure Analysis

The intersection between the Von Mises effective stress at the center node in the bottom of the defect and the ultimate true stress value indicate the stress of failure as shown in Figure 5.3. Modified B31G, and RSTRENG were also used in this study to predict the failure pressure. Table 5.1 summarizes the results of analyzing the FE corrosion defect models and the analytical solutions with a comparison between Analytical methods and FE failure pressure prediction.

Table 5.1 FE and Analytical Results for Corrosion Modeling

Defect Depth %	FE Failure Pressure MPa	Modified B31G Failure Pressure MPa	Error% (FE Vs. Modified B31G)	RSTRENG Failure Pressure MPa	Error% (FE Vs. RSTRENG)
22	10.72	9.74	-10.11	9.45	-13.49
30	9.82	9.17	-7.08	8.76	-12.09
45	8.04	8.25	2.17	7.1	-13.68
61	6.10	6.57	7.15	5.53	-10.31
80	3.53	4.66	24.27	3.07	-14.95
Average Error (%)			**3.28**		**-12.90**

The FE method proved to be in a conservative agreement with Modified B-31G and the average error shown in Table 5.1 was 3.28%. Figure 5.4 shows failure pressure predictions of corrosion defects using analytical and FE methods.

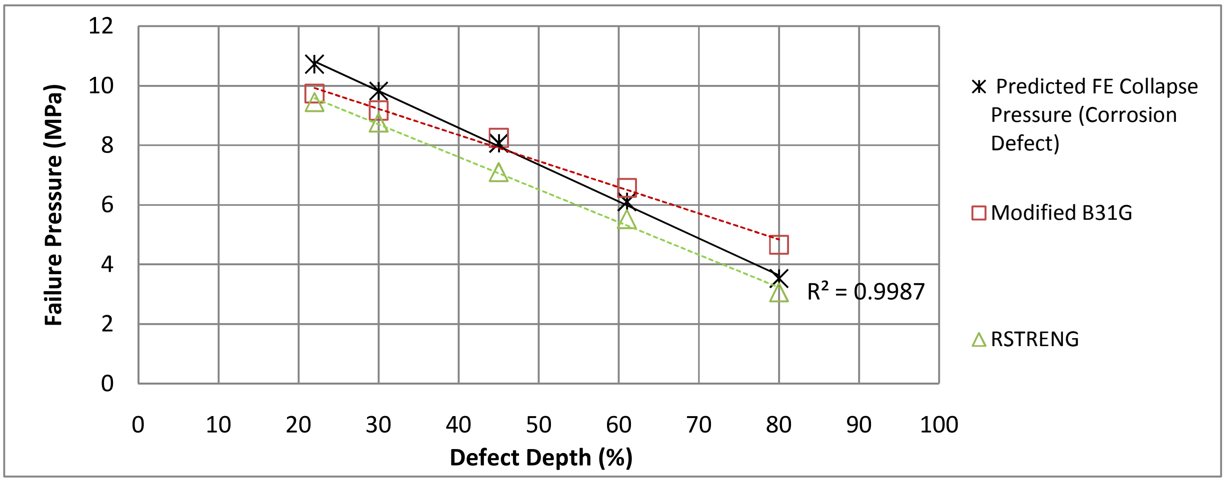

Figure 5.4 Numerical Failure Pressure Prediction of the Corrosion Defect

The results in Table 5.1 and Figure 5.4 were compared to the three experimental burst tests by Hosseini [9] (Figure 3.3) to validate the FE modeling. The two FE models of (30% and 80% WT) were conducted to extend the FE prediction. The failure pressure results showed an agreement with an average error of 10.13% as given in Table 5.2. Figure 5.5 shows a comparison in predicting the collapse pressure between experimental, analytical, and finite element modeling for the corrosion defects.

Table 5.2 Comparison Between Experimental and FE Results for Corrosion Modeling

Depth %	Failure Pressure (MPa)				Error % Experimental Vs. Predicted		
	Experimental	FE	Modified B31G	RSTRENG	FE	Modified B31G	RSTRENG
22	12.8	10.72	9.74	9.45	16.22	23.91	26.17
30	N/A	9.82	9.17	8.76	N/A	N/A	N/A
45	9.59	8.04	8.25	7.1	15.84	13.97	25.96
61	6	6.10	6.57	5.53	-1.67	-9.50	7.83
80	N/A	3.53	4.66	3.07	N/A	N/A	N/A
Average Error %					**10.13**	**9.46**	**19.99**

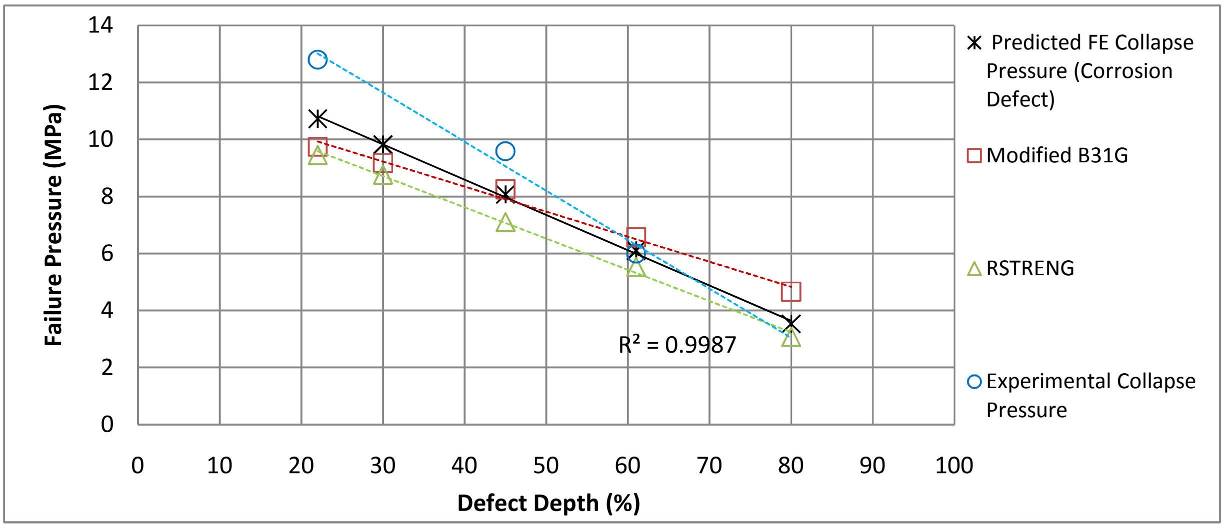

Figure 5.5 Corrosion Defect Analysis and Comparison [9].

The modeling results were conservative, with the 45% and 22%WT defects showing a greater conservative error. It is expected that the error increases for the shallower defects since the failure mode transfers to geometric instability as mentioned in the background for shallow defects. Naturally, the ultimate true stress is important in determining the failure pressure for corrosion modeling, and consequently the variation in the ultimate true stress should be considered. In present work considering the standard deviation of 17.6MPa (see Table 4.4) the ultimate true stress varied from 635.6 to 600.4MPa and the average error varied from 7.61% to 12.32%. The average errors for all prediction methods are plotted in Figure 5.6.

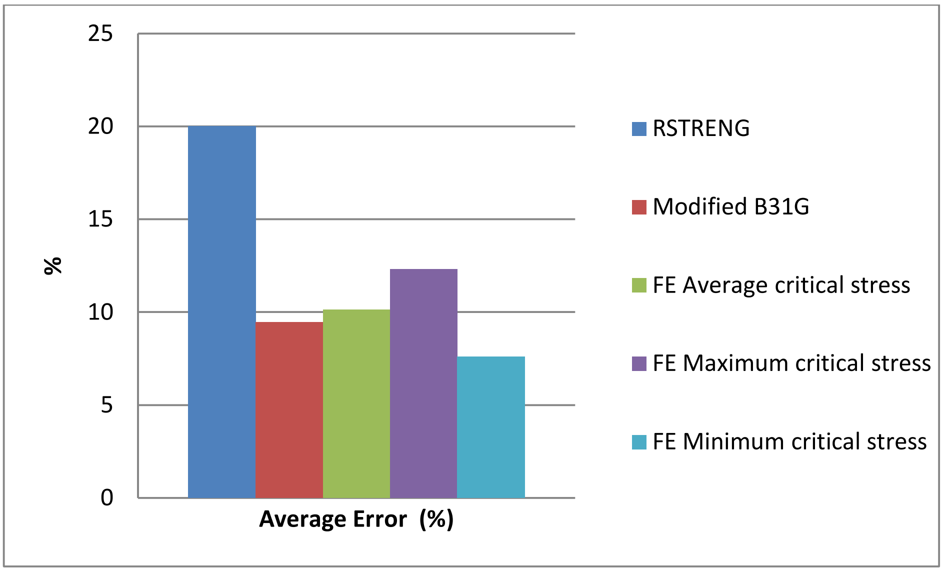

Figure 5.6 Average Error Comparison between Corrosion Defect Failure Prediction Methods

To summarize, the appropriate material properties and the geometry of a corrosion defect are the important parameters that could affect the collapse pressure prediction when using FE modeling.

5.3 Crack Defect Numerical Evaluation

The study of crack defects and prediction of stress intensity using FEM has been widely used particularly for elastic-plastic analysis. The differences between modeling LEFM and EPFM have been investigated by Cronin and Plumtree [10], and concluded that LEFM significantly overestimate, the failure pressure, as expected for this material. Therefore, EPFM was more appropriate in crack defect evaluation due to ductility of the material considered. As an example, to confirm this difference for the steel pipe under investigation a 20 %WT crack defect was modeled by both LEFM and EPFM. The results in Figure 5.7 showed that the difference in J-Integral in LEFM and EPFM increased rapidly with increase in the pipe pressure.

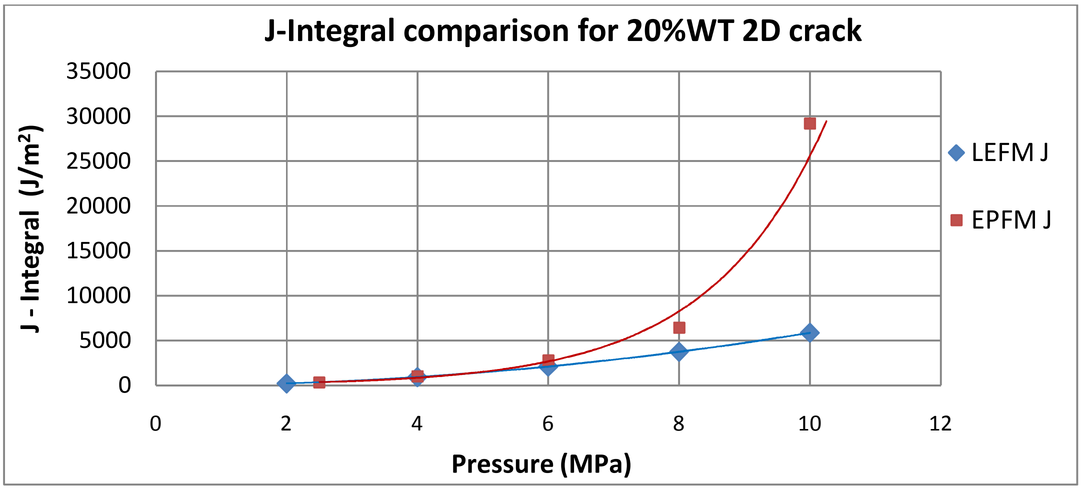

Figure 5.7 Comparison between LEFM and EPFM Modeling

The EPFM modeling of the crack was carried out for depths of 38%, 47%, 48% and 51%WT. As recommended by ABAQUS [37], the crack tip was modeled as a blunt notch with a specific radius as small as 10^{-3} of the plastic zone size r_p, so that the deformed shape, caused by internal pressure in the pipe, was no longer dependant on the original geometry. The following equation for the plastic zone size calculations was used for plain strain conditions [16]:

$$r_p = \frac{1}{2\pi}\left(\frac{K_{IC}}{\sigma_y}\right)^2 (1-2\nu)^2 \tag{4.1}$$

To obtain accurate results [37], the size of the element around the notch had to be 1/10 the notch tip radius so that the stress in the crack ligament could be captured and the results of the contour integral far from the crack were accurate when the solution converged. The fracture toughness K_{IC} for the material was estimated using CVN results (shown in Table 4.9 to be 128 MPa$\sqrt{m}$). According to equation 4.1 the plastic zone r_p was calculated to be 10^{-3} of r_p (0.013 mm). The material was modeled using incremental plasticity as recommended by ABAQUS [37]. The crack defects 200 mm lengths were modeled with an axial orientation on the outer surface of the pipe. Only quarter of the pipe was modeled to benefit from the symmetry of the problem as shown in Figure 5.8.

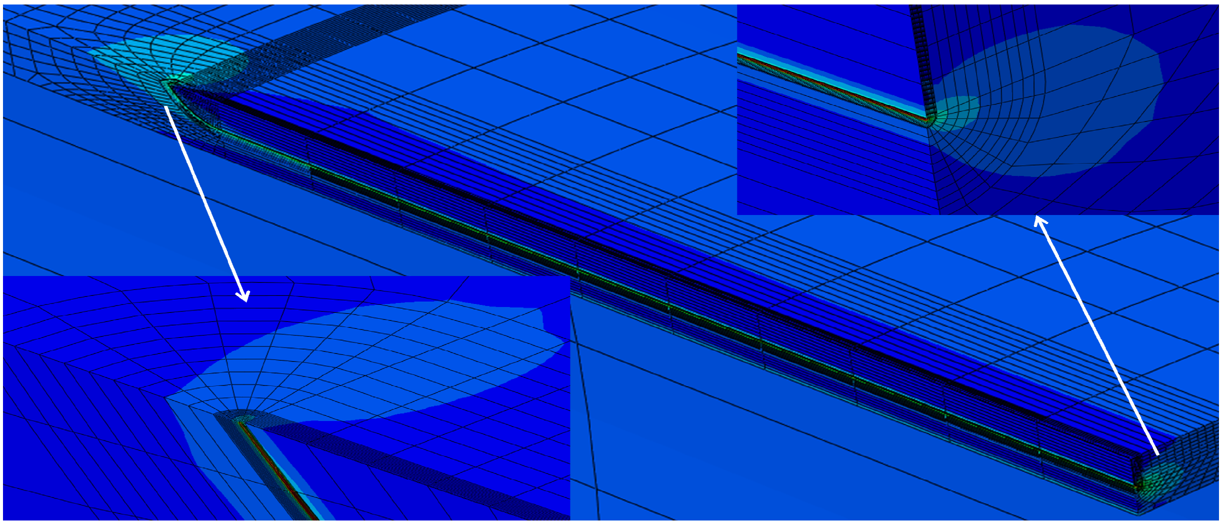

Figure 5.8 Crack Defect (Uniform depth Profile) Model

Generally, failures of cracks occur either by plastic collapse or fracture. The failure pressure criterion depends on the stress and energy release rate J in the vicinity of the crack. Both the average Von Mises stress along the crack ligament and the J-Integral values around the crack were evaluated and compared to the circumferential ultimate true stress and the critical fracture toughness $J_{0.2}$, respectively. When the average Von Mises stress in the crack ligament reached the true ultimate strength of the material first, the model was considered to fail by plastic collapse. On the other hand, if the J-Integral value in the vicinity of the crack reached the critical value of $J_{0.2}$, then failure occurred by fracture.

In the field, cracks appeared as colonies and usually represented by an equivalent uniform depth crack for collapse pressure evaluation [10] because the equivalent crack defect should be more critical than the colonies of the cracks in order to have a conservative result. Therefore, four FE cracks with uniform depths of (38%, 47%, 48%, and 51%WT) were modeled in order to simulate the burst test. Figure 5.9 - Figure 5.12 show the FE analysis of the crack models.

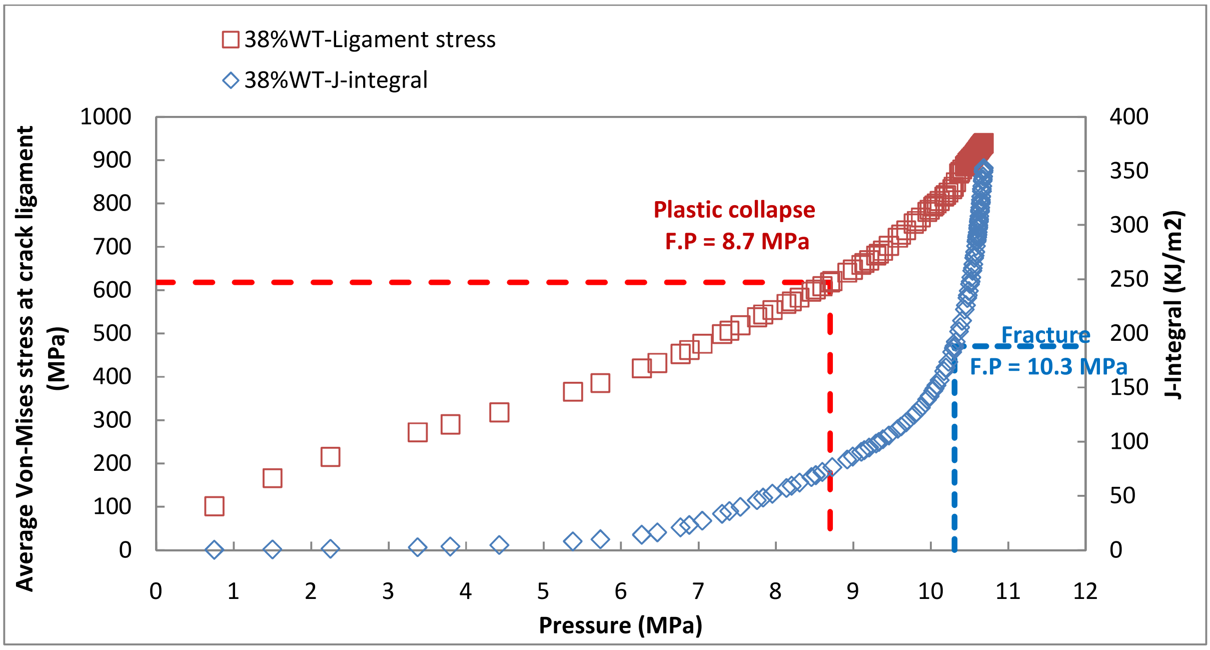

Figure 5.9 FE Analysis of 38%WT Crack Model (Uniform Depth Profile)

The average Von Mises stress in the vicinity of the 38%WT crack in Figure 5.9 reached the ultimate true stress before the fracture toughness limit was reached and therefore the failure mode was considered as plastic collapse. The same failure mode is shown for all the modeled cracks as shown in Figure 5.10 to Figure 5.12.

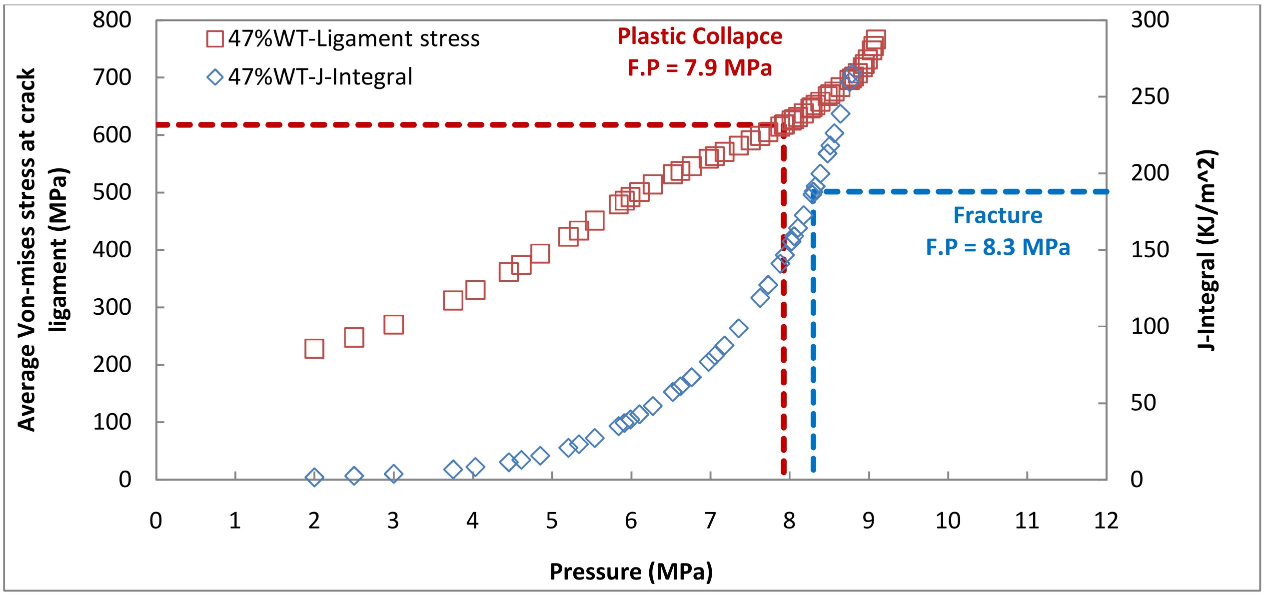

Figure 5.10 FE Analysis of 47%WT Crack Model (Uniform Depth Profile)

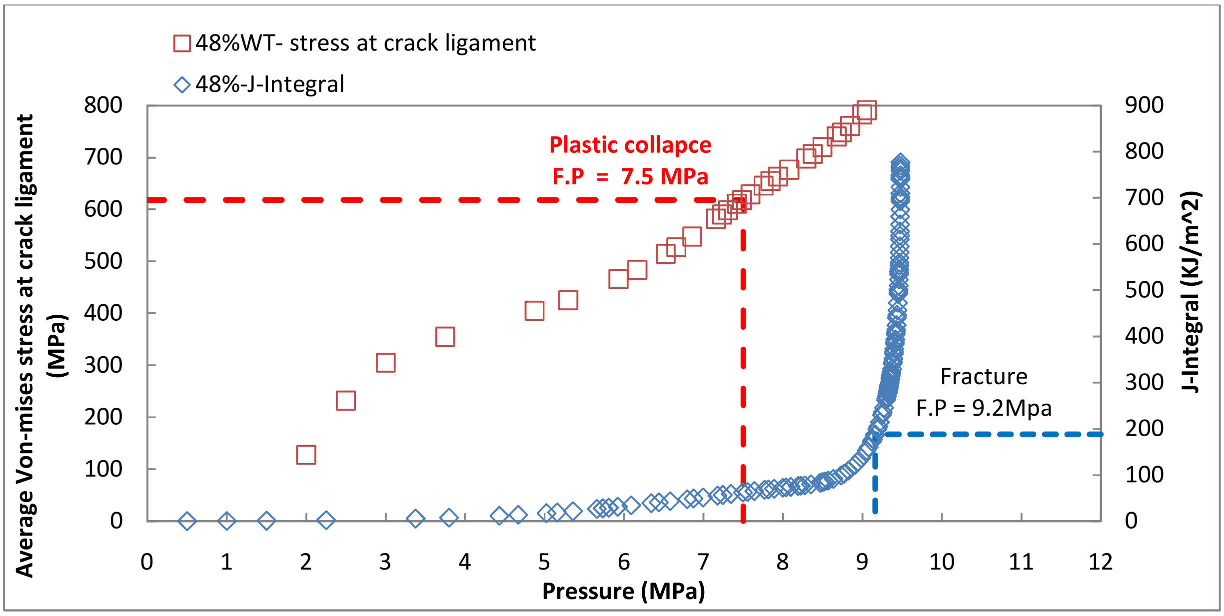

Figure 5.11 FE Analysis of 48%WT Crack Model (Uniform Depth Profile)

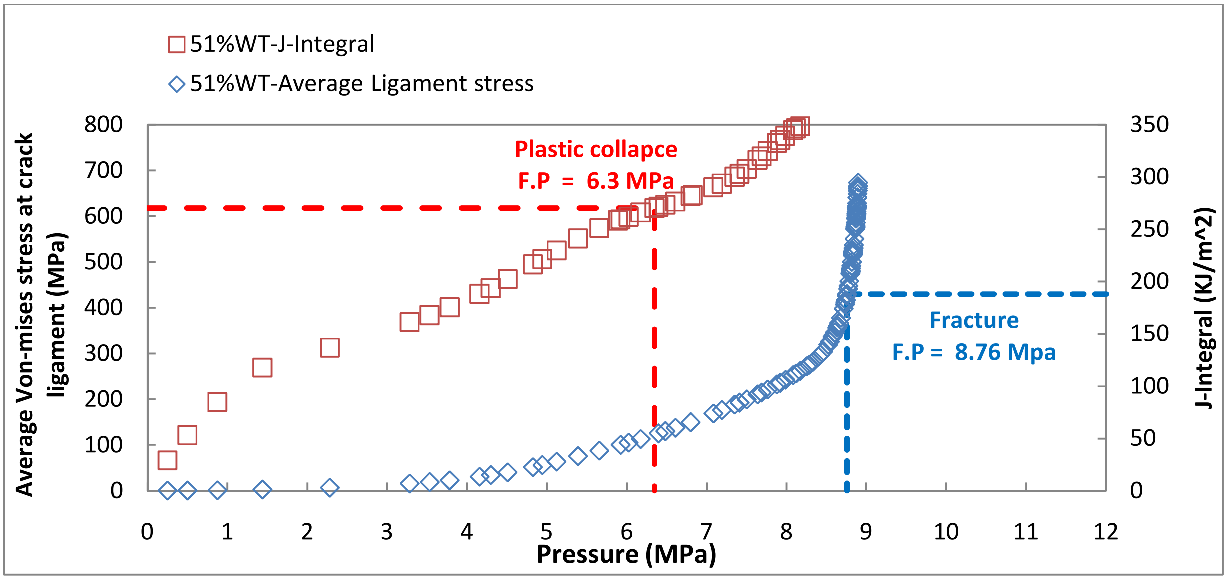

Figure 5.12 FE Analysis of 51% WT Crack Model (Uniform Depth Profile)

Table 5.3 Summarize the failure pressures of the FE analysis for the crack models based on the average Von Mises stress of the nodes in the crack vicinity.

Table 5.3 FE Results for Crack Defect (Uniform Depth Profile)

Crack ID #	FE Failure Pressure (MPa)
38% WT	8.70
47% WT	7.93
48% WT	7.50
51% WT	6.35

As expected the failure pressure increased with the decreased of the defect depth. The results of Table 5.3 are compared with the experimental and analytical results (Table 3.3) done by Hosseini [9] to validate the FE modeling results. Hosseini [9] showed that all the analytical solutions were conservative compared to his experimental results. Table 5.4 shows the FE results versus the experimental and analytical results.

Table 5.4 Crack Defect (Uniform Depth Profile) Analysis and Comparison [9]

Crack Depth %WT	**Exp. Failure Pressure (MPa)**	**Predicted Failure Pressure (MPa)**					$\mathbf{Error}(\%) = \frac{\mathbf{Exp.} - \mathbf{Pred.}}{\mathbf{Exp.}} \times \mathbf{100}$				
		FE	**API 579 Cylinder**	**BS7910 Cylinder**	**CorLAS**	**NG-18**	**FE**	**API 579 Cylinder**	**BS7910 Cylinder**	**CorLAS**	**NG-18**
38	10.10	8.70	8.10	5.80	8.48	7.10	13.86	20.0	43.0	16.0	30.0
47	9.30	7.93	7.10	4.62	7.69	6.30	14.73	24.0	50.0	17.0	32.0
48	9.60	7.50	6.86	4.45	7.58	6.20	21.88	29.0	54.0	21.0	35.0
51	8.83	6.35	6.21	3.97	7.24	5.90	28.09	30.0	55.0	18.0	33.0
Average Error (%)							**19.64**	**25.0**	**50.0**	**18.0**	**33.0**

The FE modeling results in Table 5.4 were in agreement with the burst test with an average error of 19.64%, which is less conservative than the analytical methods API 579, BS7910, and NG-18. It is apparent, that the difference between the experimental and FE failure pressures increases with increase in defect depth which is due to the difference in the defect profile shown in Figure 5.13. The FE crack models with uniform depth profiles assume that more material is removed at the shoulders. The error is due to the difference in the defect profiles between the experimented and the FE models.

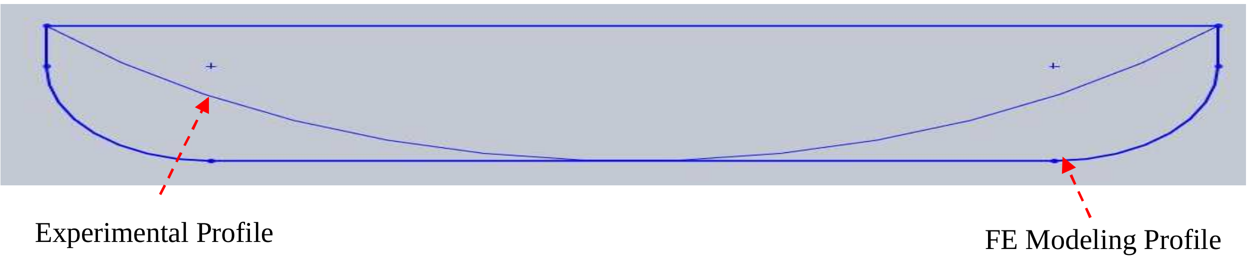

Figure 5.13 Side View of Experimental and FE Modeled Uniform Depth Crack Profile

Further work was carried out to improve the crack modeling results by considering a semi-elliptical crack profile which is shallower than the crack with uniformed profile. With a semi-elliptical crack profile, the FE modeling would be much more close to the burst test crack profile as shown in Figure 5.14 and the error should be reduced. The experimental profile was too sharp at the crack ends which will cause meshing and partitioning problems in ABAQUS therefore, the semi-elliptical FE profile still more aggressive than the experimental crack profile due to more removed material

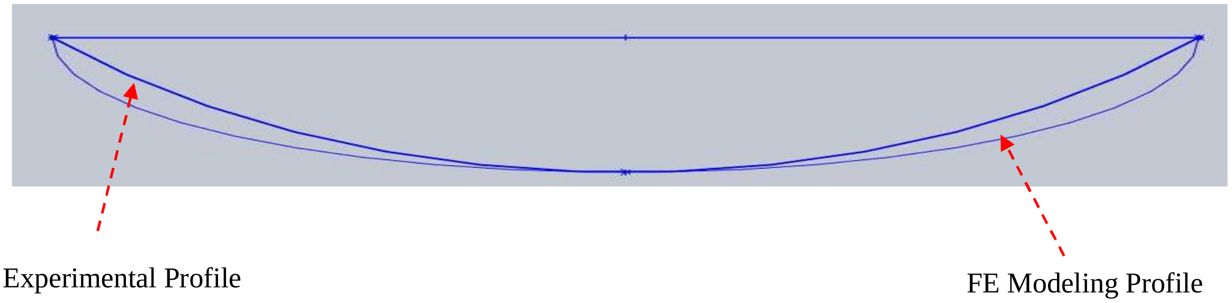

Figure 5.14 Side View of Experimental and FE Modeled Semi-elliptical Crack Profile

The semi-elliptical FE crack modeling was conducted using a computer with 8 processors and a 64-bit operating system since previous resources did not have enough memory. The semi-elliptical crack profile was successfully modeled as shown in Figure 5.15.

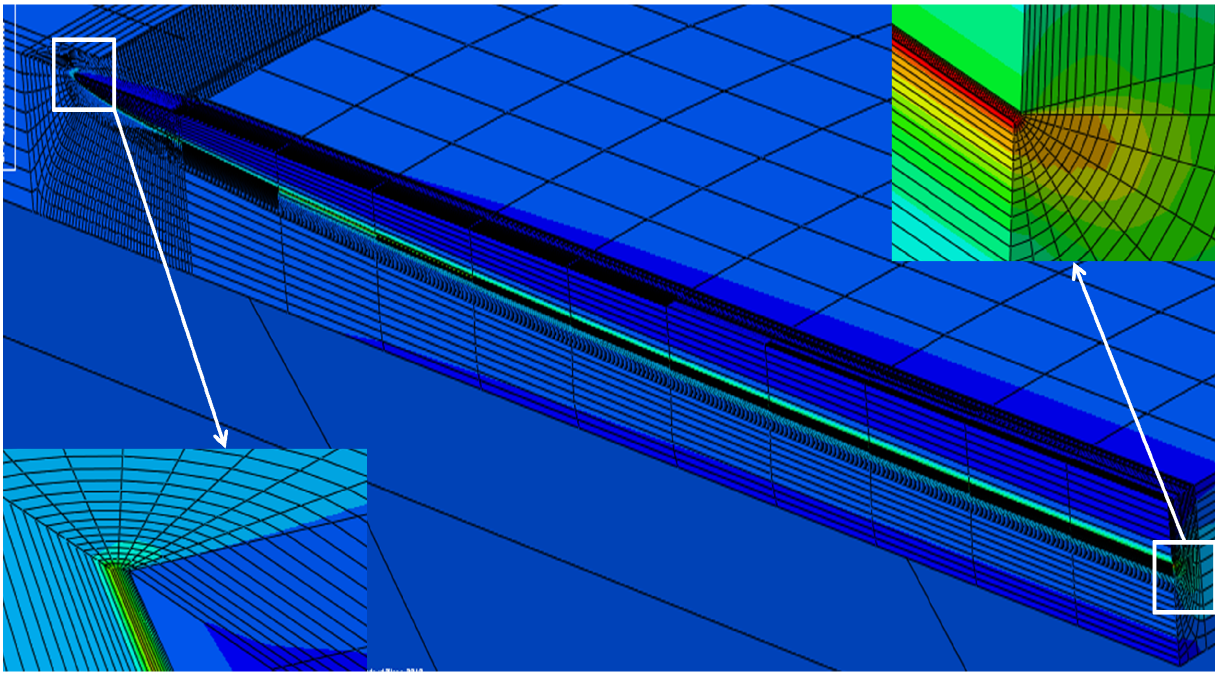

Figure 5.15 Crack Defect Model (Semi-elliptical Profile)

A set of four FE semi-elliptical crack models with depths of (38%, 47%, 48%, and 51%WT) were carried out and analyzed as shown in Figure 5.16 - Figure 5.19 using the same failure approach used for uniform depth cracks.

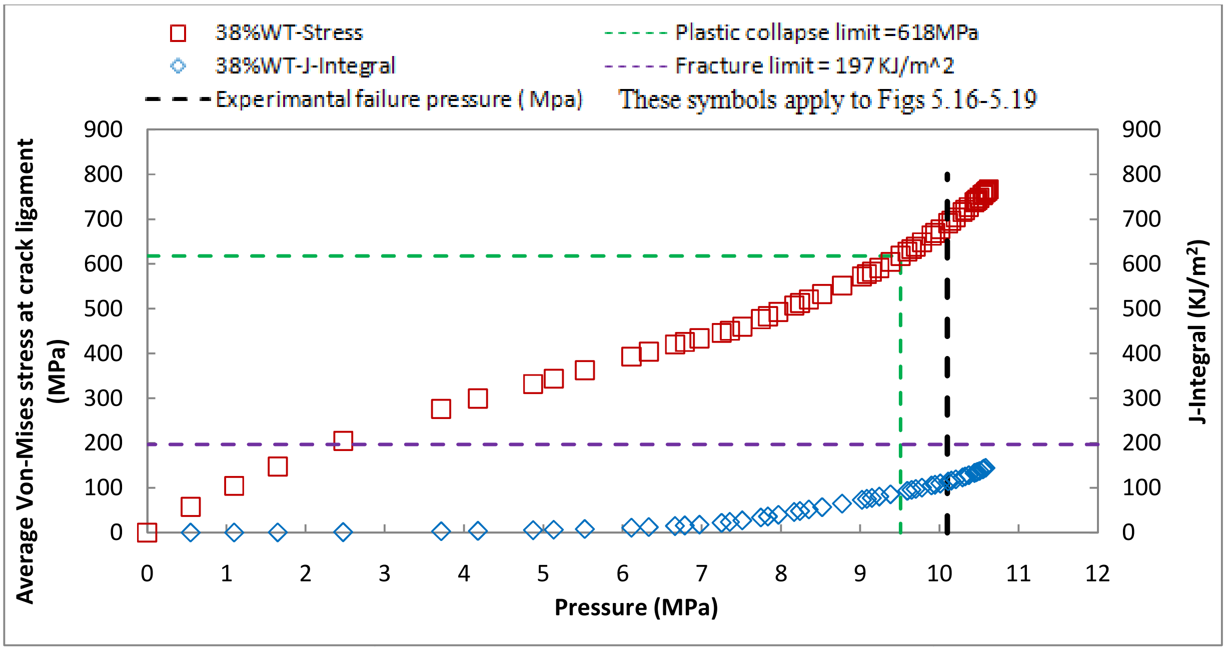

Figure 5.16 FE Analysis of 38%WT crack Model (Semi-elliptical Profile)

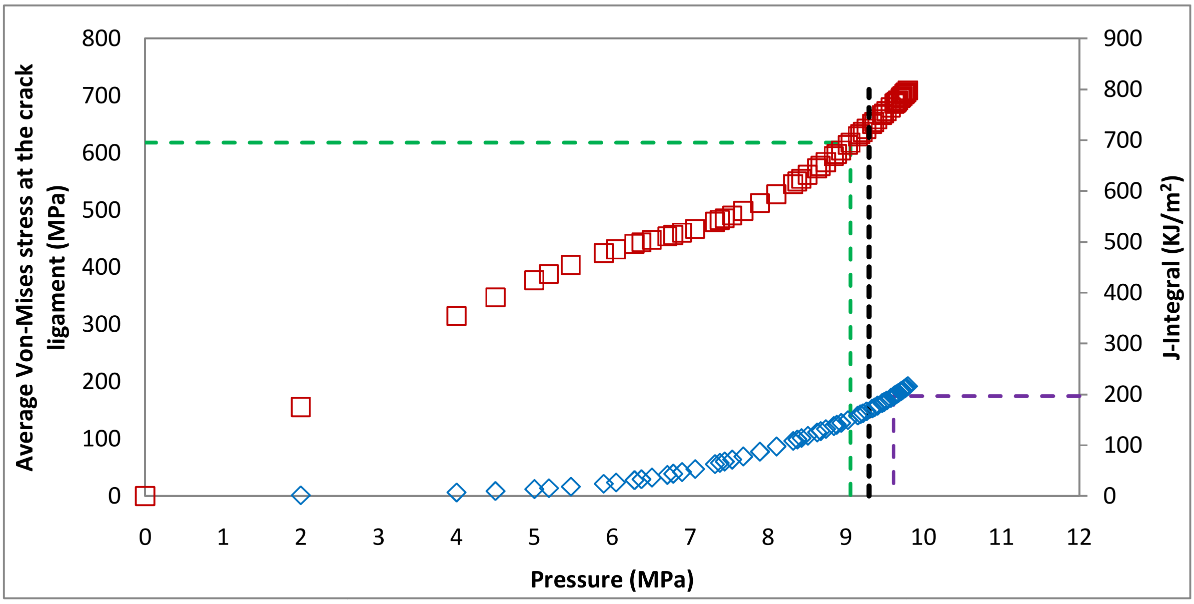

Figure 5.17 FE Analysis of 47%WT crack Model (Semi-elliptical Profile)

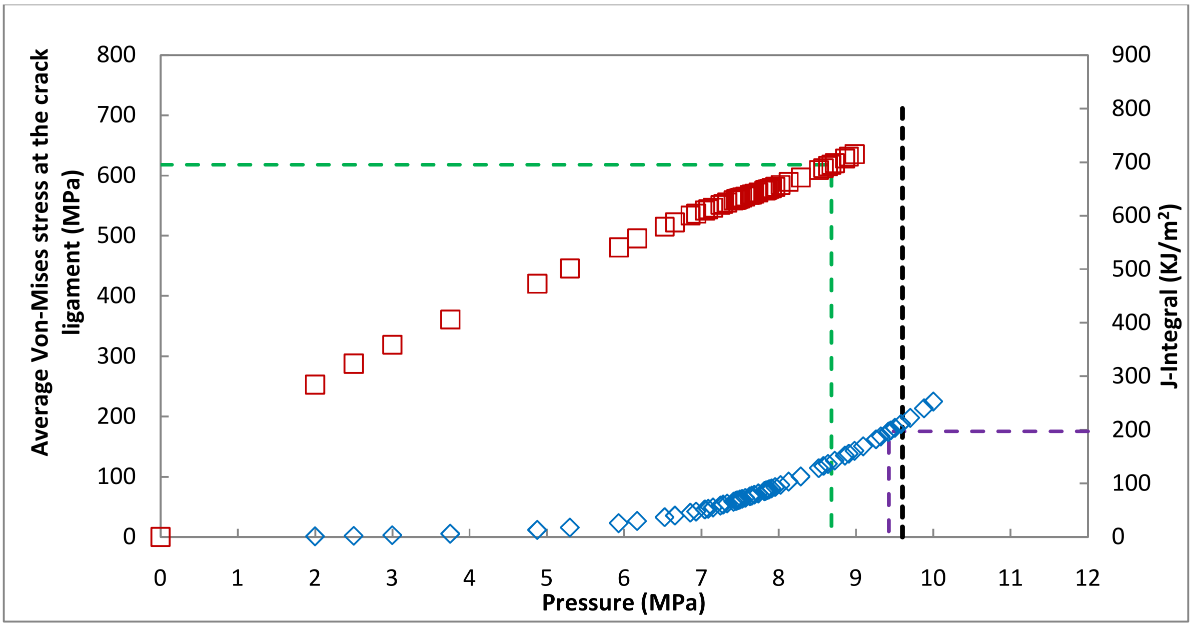

Figure 5.18 FE Analysis of 48% WT crack Model (Semi-elliptical Profile)

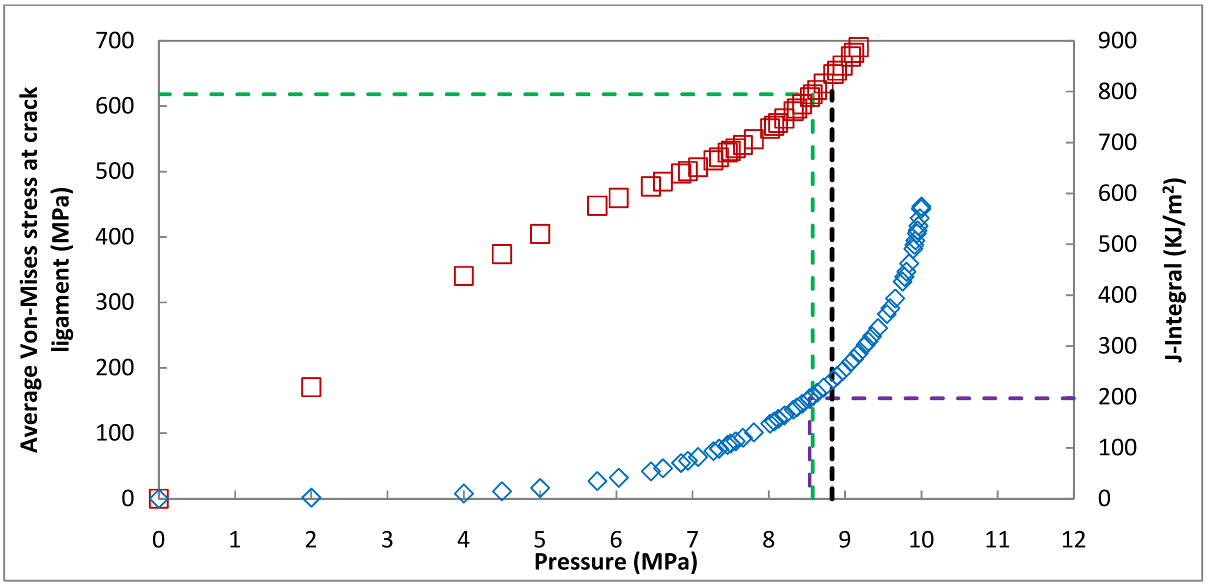

Figure 5.19 FE Analysis of 51% WT crack Model (Semi-elliptical Profile)

When considering the uniform depth crack modeling and the experimental results, the semi-elliptical crack models results showed a significant improvement in predicting the crack defect collapse pressure as shown in Table 5.5.

Table 5.5 Crack Defect (Semi-elliptical profile) Analysis and Comparison

Crack #	Experimental Failure Pressure (MPa)	FE Failure Pressure (Semi-elliptical) (MPa)	FE Failure Pressure (uniform depth) (MPa)	Error Exp. Vs. FE (semi-elliptical) (%)	Error Exp Vs. FE (Uniform depth) (%)
38%WT	10.10	9.51	8.70	5.84	13.86
47% WT	9.30	9.06	7.93	2.58	14.73
48%WT	9.60	8.68	7.50	9.58	21.88
51%WT	8.83	8.53	6.35	3.40	28.09
Average				**5.35**	**19.64**

As shown in Table 5.5 the predicted collapse pressure error using semi-elliptical FE crack profile is much less conservative than using uniform depth FE crack profile, as expected. The average error improved from 19.64% for the uniform depth crack profile to 5.35% for semi-elliptical crack profile. Figure 5.20 was plotted to compare the FE results with the other analytical methods from Table 5.4.

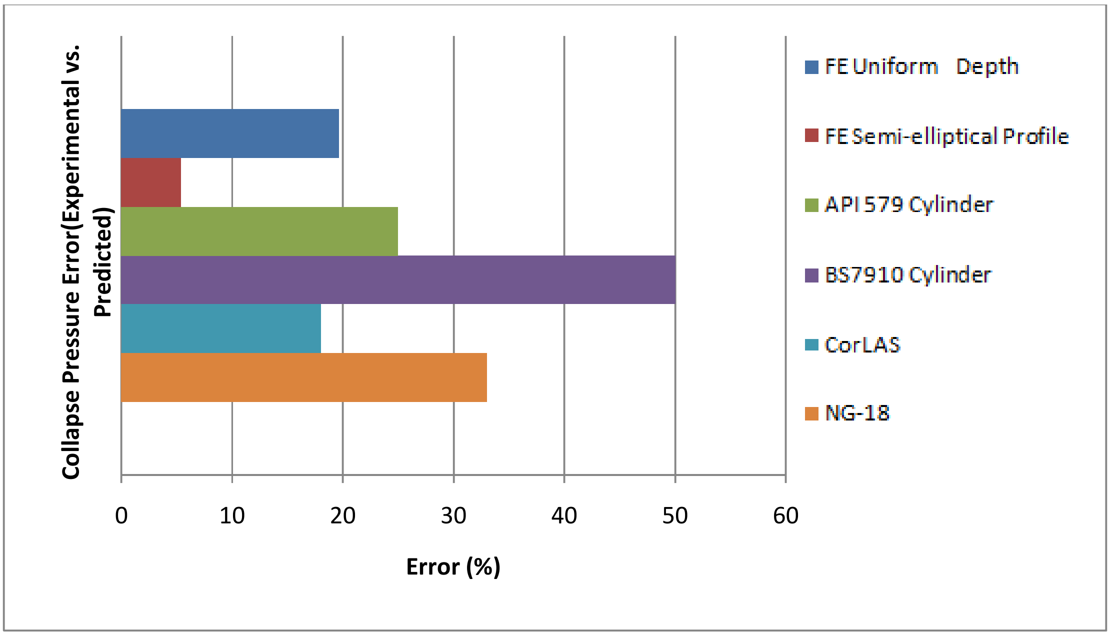

Figure 5.20 Comparison between FE and Analytical Failure Pressure Prediction.

Apparently, the FE method provided the best prediction for crack defect when compared with the other analytical methods as shown in Figure 5.20. Moreover, the crack defect profile was proven to be an important parameter that could affect the collapse pressure prediction when using FE modeling. Figure 5.21 was contains the collapse pressure results for the experimental, FE, and analytical.

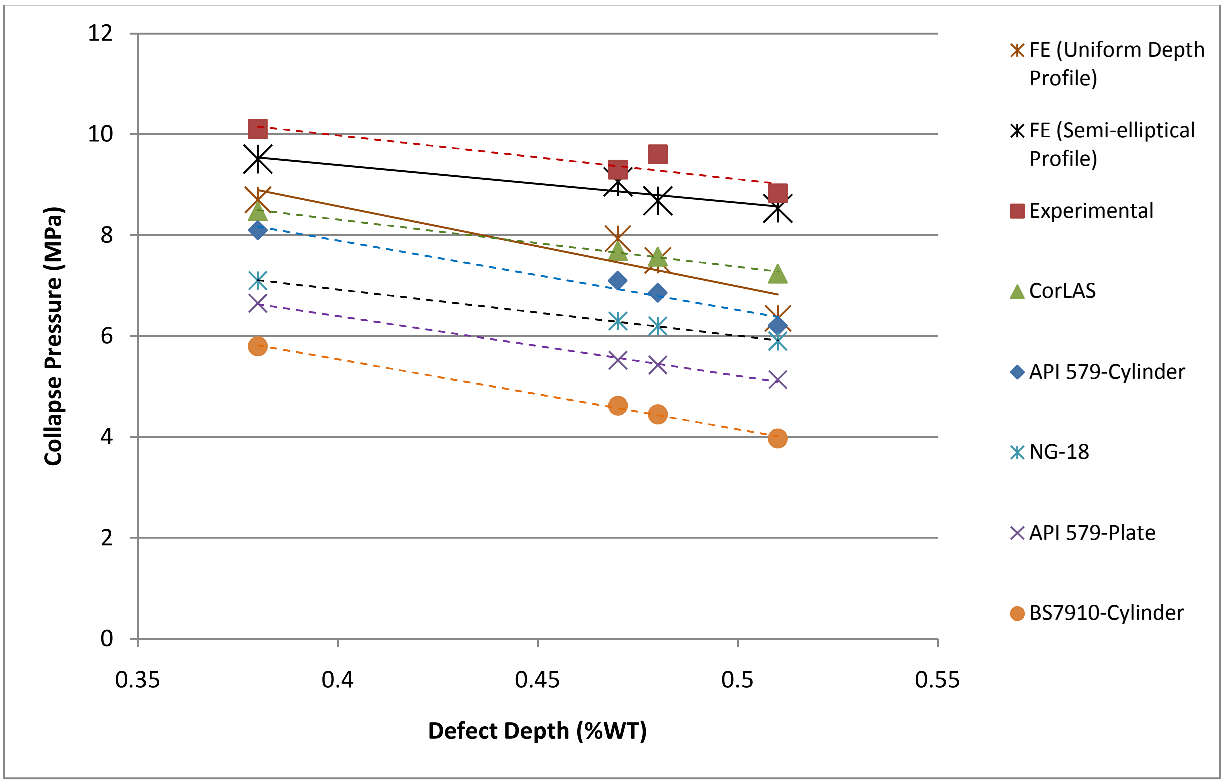

Figure 5.21 Crack Defect Comparison between FE, Experiment, and Analytical Failure Pressure [9]

5.4 Crack-in-Corrosion (CIC) Defect Numerical Evaluation

Five burst tests were modeled and the results were compared to the experimental results that were undertaken by Hosseini [9]. The CIC models have a corrosion defect with a flat bottom and a uniform depth crack as shown in Figure 5.22. The corrosion defect was 30 mm in width and 200 mm in longitudinal length while the crack length was 100 mm. Note that only quarter of the pipe was modeled.

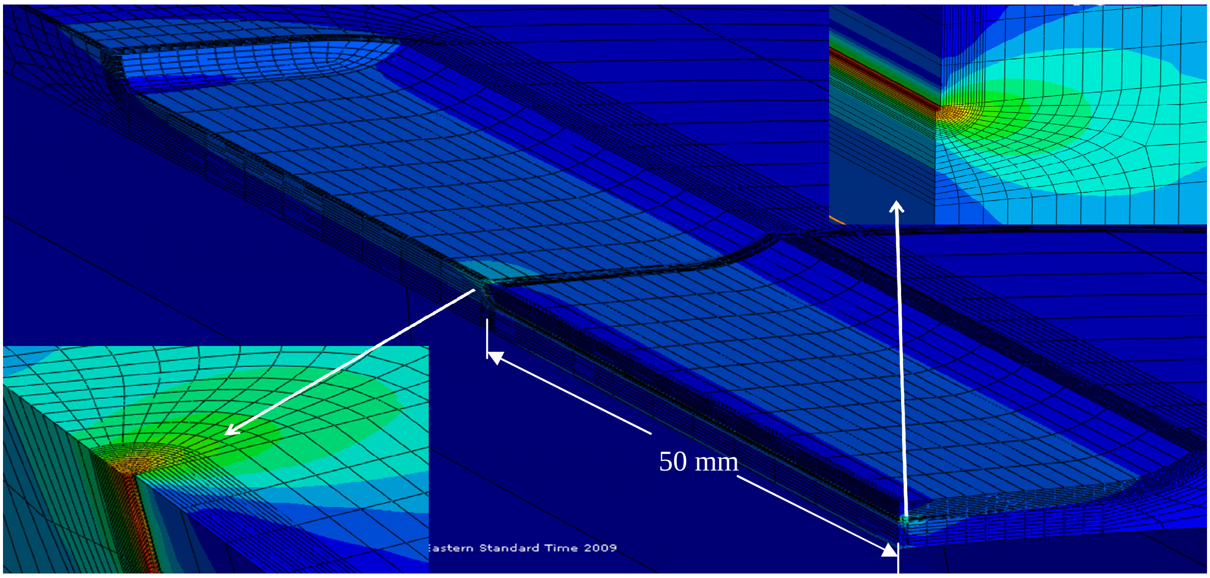

Figure 5.22 CIC Defect Profile

Table 5.6 shows the CIC defect geometries for the five FE models and the burst tests. The CIC models contain corrosion groove coincidence with crack. For example, the total defect depth of CIC1 is 52%WT out of the wall thickness that is divided into corrosion and crack percentages. 68% of the 52%WT is the corrosion depth while the rest of the 52%WT is 32% crack depth as shown in Figure 5.23 .

Table 5.6 CIC Defect Geometry [9]

Test ID	Corrosion Length (mm)	Corrosion Width (mm)	Defect Depth		Total Defect Depth (%WT)
			Crack (%)	Corrosion (%)	
CIC1	200	30	32	68	52
CIC2			38	62	59
CIC3			34	66	60
CIC4			30	70	61
CIC5			35	65	66

The difference in crack section profile between the experimental and modeled CIC defect is also shown in Figure 5.23. The FE corrosion defect profile of the CIC defect was modeled as the experimental defect, while the crack profile (in red color) was modeled with a uniform depth instead of semi-elliptical profile. The difference resulted in a conservative failure pressure because more material was removed from the crack defect. Accordingly the stress will be more concentrated in the sharper corners of the defect.

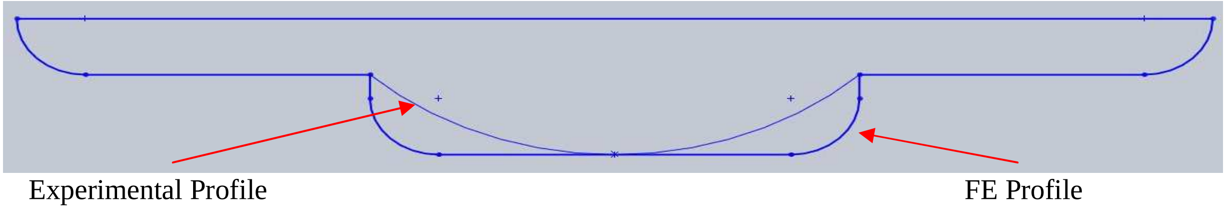

Figure 5.23 View of Actual and Modeled CIC Profile

The CIC defect was expected to fail by plastic collapse hence the failure criterion used in the analysis was the same as that used in evaluating the failure pressure for modeling the crack defect. The Von Mises stress in the crack ligament was calculated then averaged and compared to the circumferential ultimate true stress. In addition, the J-Integral around the crack profile was determined and compared to $J_{0.2}$ = 197 KJ/m^2 to assess whether if the crack failed by fracture or plastic collapse. Figure 5.24 - Figure 5.28 show the FE analysis of the CIC defect models.

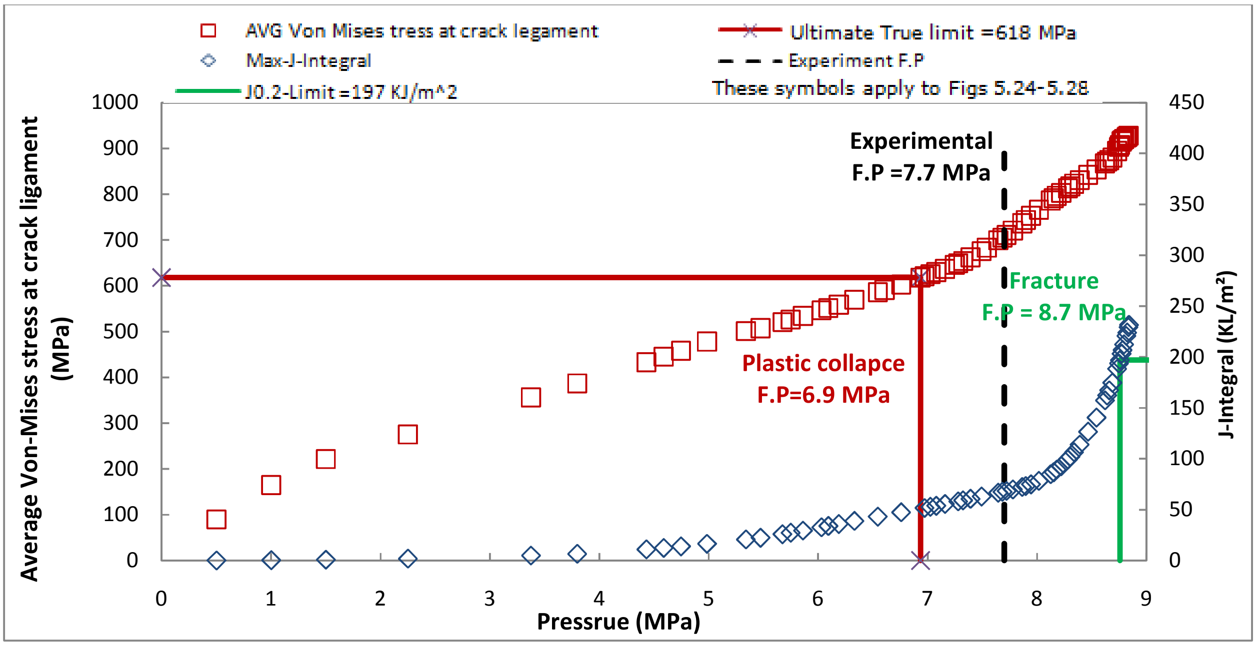

Figure 5.24 Failure Pressure Analysis of CIC-1

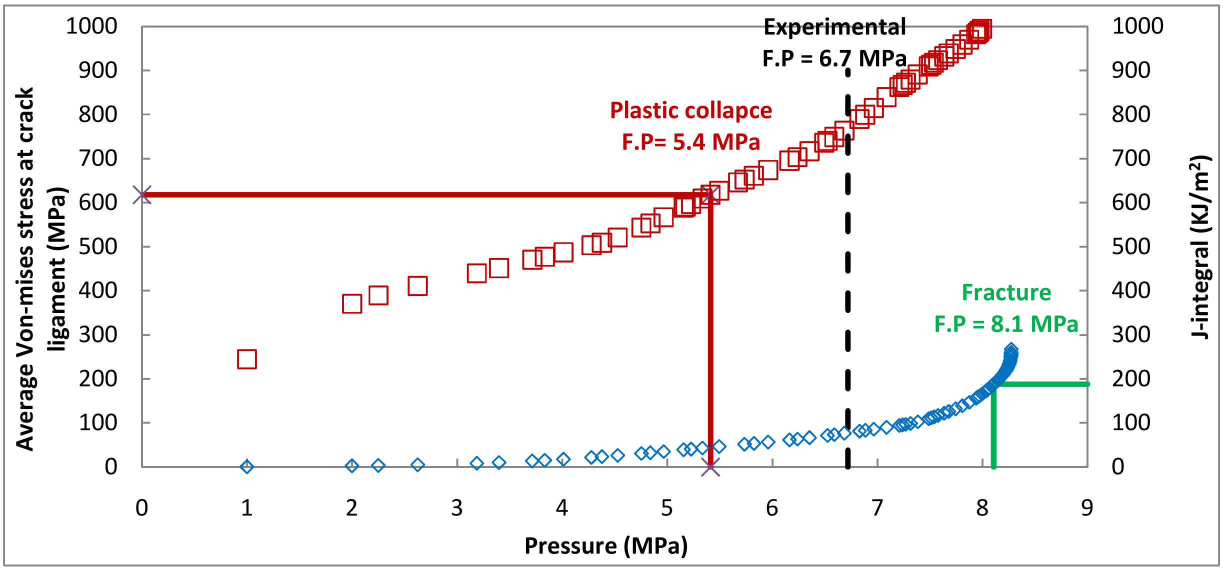

Figure 5.25 Failure Pressure Analysis of CIC-2

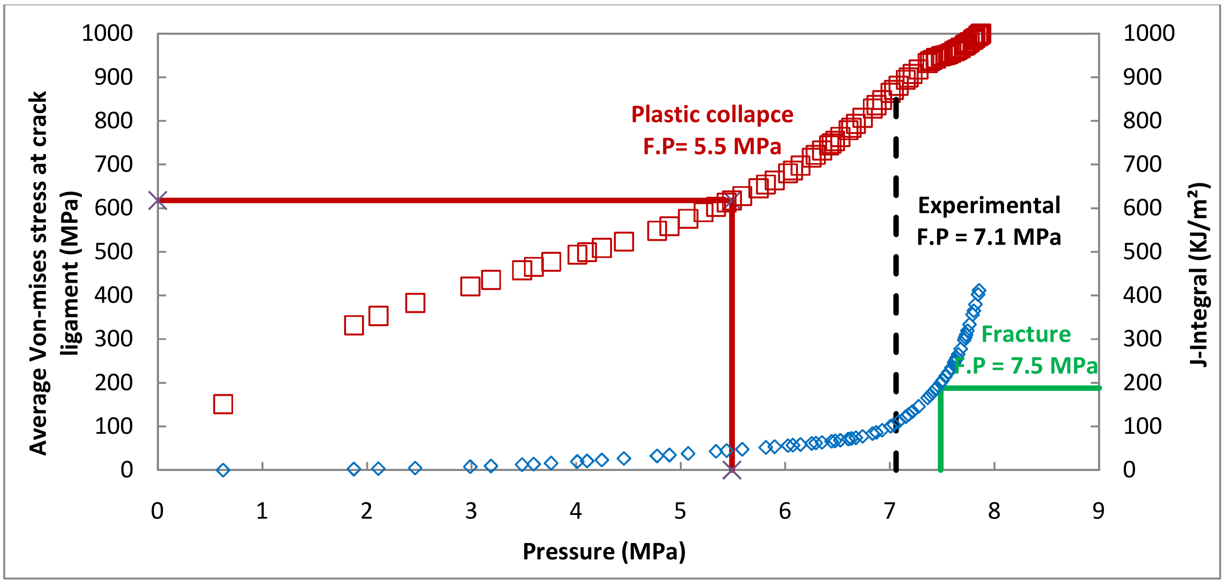

Figure 5.26 Failure Pressure Analysis of CIC-3

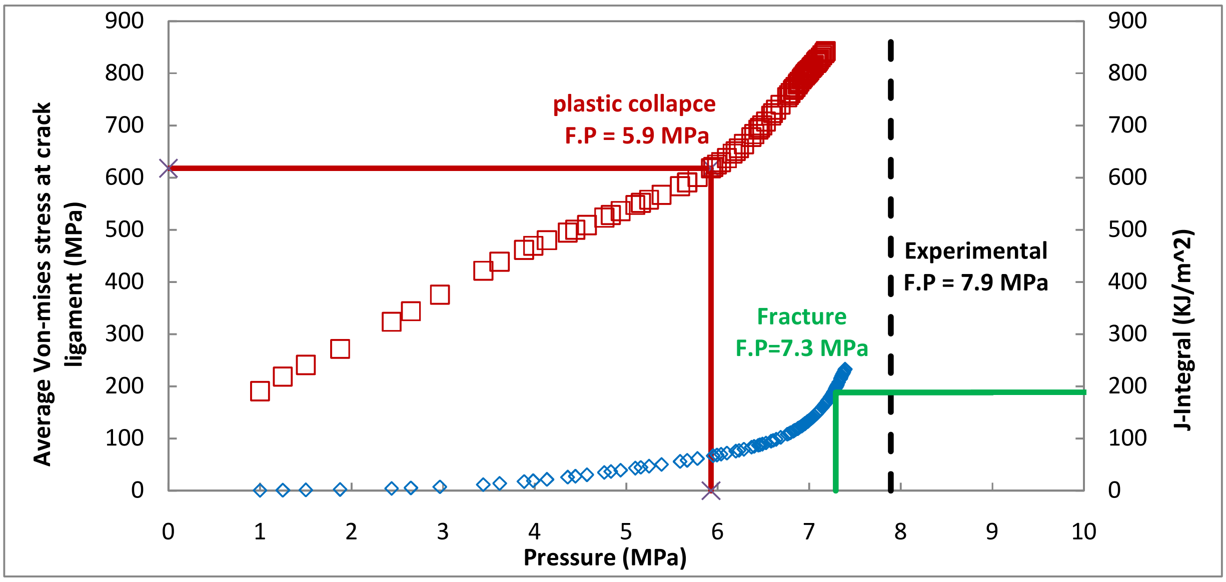

Figure 5.27 Failure Pressure Analysis of CIC-4

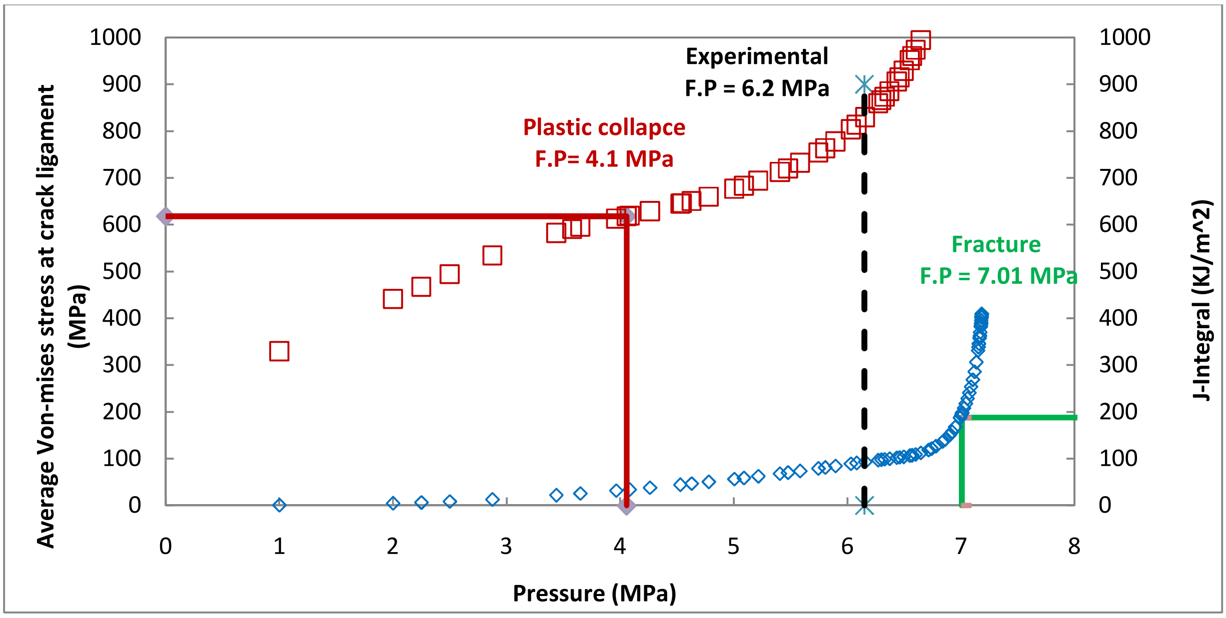

Figure 5.28 Failure Pressure Analysis of CIC-5

Table 5.7 summarizes the experimental and FE results for the CIC defect.

Table 5.7 Comparison Between Experimental and FE Results for CIC Modeling

CIC Defect ID	CIC Defect Depth (WT%)	Experiment Failure Pressure (MPa)	FE Failure Pressure (MPa)	Difference%
CIC-1	52	7.7	6.94	10.34
CIC-2	59	6.7	5.41	19.49
CIC-3	60	7.1	5.49	22.24
CIC-4	61	7.9	5.93	24.84
CIC-5	66	6.2	4.06	33.98
Average (%)				**22.18**

The CIC modeling results in Table 5.7 were conservative compared to the experimental results. The average difference was 22.18%. In general, the difference increased with crack depth in the CIC, similar to the crack modeling results. This was due to more material being removed at the shoulders in the crack profile compared to the experimental semi-elliptical crack profile shown in Figure 5.23.

Figure 5.29 shows a comparison between the FE, experiment and analytical solution. The analytical solution was done by Hosseini [9] for crack only and corrosion only to see if the CIC defect close to crack or close to corrosion. The results given in Figure 5.29 show that the FE method predicts the failure pressure with the same trend as the experimental burst test. It also shows that the FE approach provides a good estimation of the failure pressure of a CIC defect. It is possible that the error may be reduced if crack's profiles were modeled as semi-elliptical.

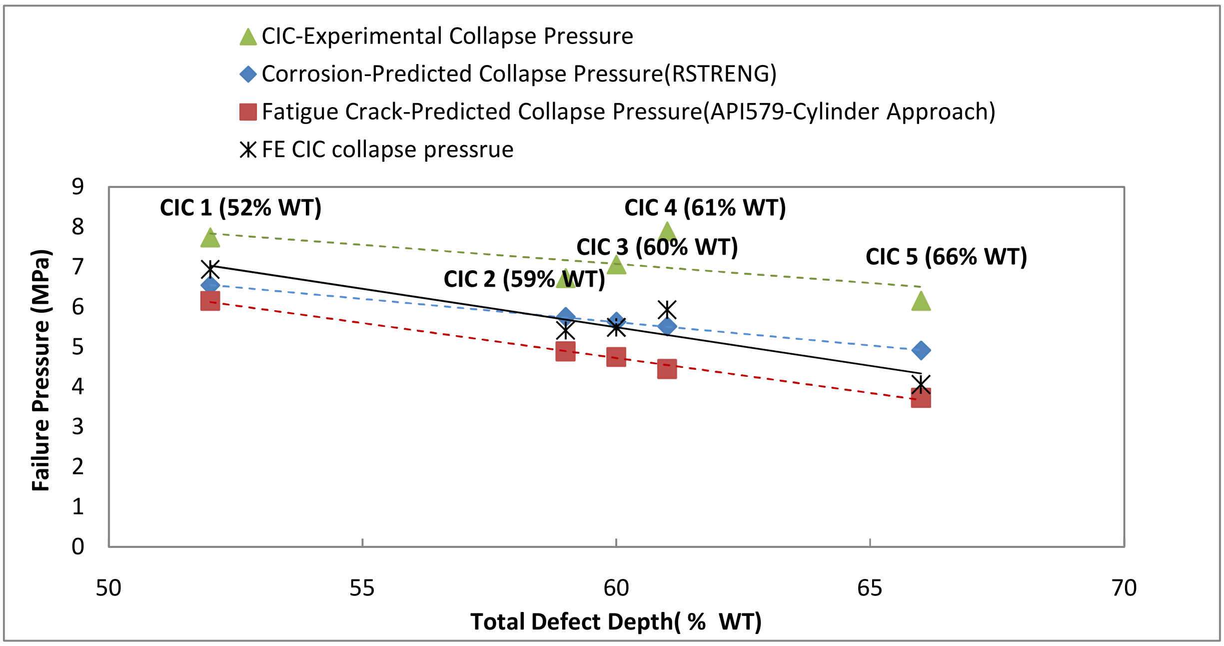

Figure 5.29 Comparison Between Experimental and FE Results for CIC Modeling [9]

Chapter 6 Results and Discussion

Modeling failure prediction requires accurate material properties, geometry, boundary condition, and appropriate failure criteria. The material properties of the pipe were very important parameters for FE modeling and to define the failure criteria of the defects under investigation in this study. The tensile testing provided the true circumferential ultimate stress (618 MPa (17.6 MPa)) that was necessary to define the plastic collapse (critical stress) limit. The circumferential tensile test results were used because the hoop stress of the pipe was higher and dominates defect failure. As expected, the circumferential tensile stresses were greater than the longitudinal strength. In addition, the yield strength of the circumferential tensile test had a large variation due to the curved specimens, which were flattened before testing.

CVN testing gave an upper shelf average energy of 43.5 J which was correlated to the fracture toughness (K_{IC} and $J_{0.2}$). The test also provided the transition temperature of -22.9 (°C). The variation of the CVN energies was due to the pipe thickness which allowed only sub-sized test specimens. The specimen results had a scatter which was magnified when scaling the energy results to equivalent full size specimen absorbed energy.

The J-Testing results were analyzed but the test data were not qualified to provide the fracture toughness (J_{IC}) directly. The pipe wall thickness allowed for only small test specimens which exhibited significant plasticity in the vicinity of the cracks. The data from the tests was used to determine $J_{0.2}$ which is an approximation of the fracture toughness. $J_{0.2}$=197 KJ/m^2 was a very important value that defined the fracture limit used later for crack and CIC FE modeling. The empirical correlated $J_{0.2}$ = 97 KJ/m^2 based on CVN upper shelf energy was very conservative when compared with the value measured from J-Integral testing which was 197 KJ/m^2. Thus, it is better to determine the fracture toughness using J-Integral testing for J_{IC} if possible or to use $J_{0.2}$ for thin wall pipes. The correlation was still considered valid but it will result in very conservative failure predictions.

The corrosion modeling was done for defect depths of 22%, 45%, and 61%WT resulted in conservative predictions compared to the experimental failure pressure, with an average error of 10.13%. The modeled pipe was considered to fail when the material at the bottom of the defect reached the circumferential ultimate true stress of 618 MPa. If the variation of the circumferential ultimate true stress results was considered then the predicted error range varied from 5.66 to 27.89% conservative in agreement with previous studies. The error became greater with shallower corrosion defects because the failure mode is changing to geometric instability when the defect depth is less than 20% WT.

The crack modeling was done for depths of 38%, 47%, 48% and 51%WT based on two approaches, the uniform depth profile and the semi-elliptical profile. The crack with uniform depth profile was done because the uniform shape is the logical equivalent shape for a colony of cracks [10] whereas the crack with the semi-elliptical profile was done to have less conservative results and because the experiments were done with semi-elliptical cracks. The FE modeling results for crack defects with uniform depth profile had an average error of 19.64% which is more conservative than the burst test results. The error increased with deeper crack defects as the modeled crack become more aggressive than the actual crack due to more material being removed. For crack defect modeling with a semi-elliptical defect profile, the average error was 5.35% (conservative) compared to the experimental failure pressure. The reason for the improvement was that the experimental crack profile was close to semi-elliptical. Modeling a crack with uniform depth is still valuable considering a colony of cracks [10] despite the large error in the crack modeling of uniform depth profile when compared to the specific experiment in this study.

Five CIC defects were modeled with total depths of 52%, 59%, 60%, 61%, and 66%WT. As was done for the crack modeling, the failure pressure criterion depended on the stress and energy release rate J in the vicinity of the crack. The CIC predicted failure pressure results were conservative compared to the experimental results with an average error of 22.18%. The error increased with the total defect depth because the deeper defects had more removed material. The error can be improved to be less conservative if the crack in the CIC defect was modeled with semi-elliptical profile.

Chapter 7 Conclusions and Recommendations

The FE modeling of the corrosion, crack, and CIC proved to give good estimations of the failure pressures. The defect geometry and the material properties are the important factors that affect the failure pressure predictions. In general, the FE modeling collapse pressure results were conservative compared the experimental results.

The circumferential tensile test data was used to predict response and failure of the defects. The ultimate true stress was the critical stress used to determine the failure initiation in corrosion defect modeling. It is recommended that the tensile test variation is considered, since the failure prediction depends on the value of the critical stress (ultimate true stress).

For CVN testing, full size specimens are preferred, because the sub-sized specimens may exhibit additional scatter. The sub-sized specimens used were scaled in order to match the full size absorbed energy. In addition, using the upper shelf average energy and correlating to the fracture toughness or $J_{0.2}$ using existing data fives a conservative estimate of the toughness.

For the J-Integral testing, the test specimen should be thick for the data to be qualified to provide J_{IC}. Since thin specimens were used, and the data was not qualified to provide J_{IC}, $J_{0.2}$ was used as an approximate value for the fracture toughness. J-Integral testing is recommended because it provides better estimation of the fracture toughness compared with Mak and Tyson correlation charts.

The corrosion FE modeling results gave conservative results compared to the experimental results and the average error was 10.13%. The error became more conservative with shallower corrosion (less than

20%WT) defects since the failure mode transfers to geometric instability. It is important to account for the scatter in the tensile strength when analyzing the FE corrosion defect. Moreover, removing the end caps from the calculation will decrease the computational time with no effect on the failure prediction.

The crack defect modeling results were conservative with an average error of 19.64% for the uniform depth crack profile and 5.35% for the semi-elliptical crack profile. The crack defect modeling is sensitive to the defect profile and the material loss affected the failure pressure prediction. The uniform depth approach should be used when having a colony of cracks in the field cases. To simulate an experimental crack, the crack profile of the model should be as close as possible to the experimental one. The J-Integral around the modeled crack tip should be monitored in both the depth, and the shoulders on the surface. The greater value has to be compared to the fracture toughness for predicted failure by fracture.

The results of CIC FE modeling were conservative when compared with the experimental results and the average difference was 22.18%. This error was also due to the defect profile being more aggressive than the experimental CIC defect. To conclude, the crack and corrosion modeling are sensitive to the profile shape and the amount of removed material.

For future work, the sub-modeling technique is highly recommended when having such repetitive models. For instance, all the modeled defects in this study had the same lengths and widths so they could be modeled separately and added later to the rest of the pipe body. This method would allow the user to have a very fine mesh for the sub-models (the defected parts) without having to remodel the whole pipe every time.

References

[1]. Canadian Energy Pipeline Association, www.cepa.com, September 2009.

[2]. K. Grimes, British Gas Inspection Services; D. G. Jones, British Gas PLC Determining Pipeline Fitness for Purpose From High Resolution Smart Pig Inspections. CORROSION 96, March 24 - 29, 1996 , Denver, Co

[3]. A.K. Escoe,”Piping and Pipeline Assessment Guide”, Elsevier, 2006.

[4]. D. S. Cronin, “Assessment of Corrosion Defects In Pipelines”, PhD Thesis, University Of Waterloo, 2000.

[5]. American Petroleum Institute, “Recommended Practice for Fitness for Service”, API -579, 2000.

[6]. British Standards Institute, BS 7910. “Guide on Methods for Assessing the Acceptability of Flaws in Metallic Structures”, BSI-10 2000.

[7]. SIMULIA, www.simulia.com, July 2010.

[8]. ANSYS, Inc., www.ansys.com, July 2010.

[9]. A. Hosseini, “Assessment of Crack in Corrosion Defects in Natural Gas Transmission Pipelines”, MSc Thesis, University of Waterloo, 2010.

[10]. D. S. Cronin and A. Plumtree, “Assessment of Crack in Corrosion Defects in natural Gas Transmission Pipelines”, Confidential report to TCPL, November 28, 2006.

[11]. G. R. K. Kanters, W.A.”Pipeline Corrosion and Cracking and the Associated Calibration Considerations for Same Side Sizing Applications“, Eclipse Scientific Products Inc., Williamsford, Ontario, Canada.

[12]. Corrosion Monitoring Focused Site, www.corrosion-club.com, June 2010.

[13]. Kingston Technical Software Co., www.corrosion-doctors.org, July 2010.

[14]. R. J. Eiber, W.A. Maxey, A.R. Duffy, G.M. McClure, “Further Work on Flaw Behavior in Pressure Vessels”, Institution of Mechanical Engineers, C88/71, February 1971.

[15]. A. Cosham, P. Hopkins,”Best Practice for the Assessment of Defects in Pipelines-Corrosion”, Engineering Failure Analysis, 2007, 1245-1265.

[16]. Wikipedia, www.en.wikipedia.org, July 2010.

[17]. G. Glinka, “Course Notes ME627, Fatigue & Fracture Mechanics Analysis & Design”, Fall 2007.

[18]. American Society for Testing and Materials (ASTM) Standards, ASTM E1820, 2008.

[19]. N. E. Dowling, “Mechanical Behavior of Materials”, Pearson Education, Third Edition, 2007.

[20]. British Standards Institute, BS 7910. “Guide on Methods for Assessing the Acceptability of Flaws in Metallic Structures”, Appendix P, BSI-10 2000.

[21]. D. S. Cronin and A. Plumtree, “Assessment of Crack in Corrosion Defects in Natural Gas Transmission Pipelines”, Confidential report to TCPL, November 30, 2007.

[22]. CorLAS User Manual.

[23]. C. E. Jaske and J. A. Beavers.,” Fitness-For-Service Evaluation of Pipelines with Stress-Corrosion Cracks or Local Corrosion”, The International Conference on Advances in Welding Technology (ICAWT), October 1999.

[24]. American Society for Testing and Materials (ASTM) Standards, ASTM E23, 2008.

[25]. CSA, “CSA Z245-99, Oil and Gas Pipeline Systems”, CSA, Toronto, 1999.

[26]. American Petroleum Institute, “Recommended Practice for Fitness for Service”, API -579, section F.4.3.3-d, 2000.

[27]. W. R. Tyson, “Assessment of Crack Defects”, Banff Pipeline Workshop, 2005.

[28]. D. K. Mak, and W.R. Tyson, “Material Assessment of Canadian SAW line-pipes”, IPC 1998, 711-721.

[29]. BMT Fleet Technology, www.fleetech.com, July 2010.

[30]. D. H. Mok, R. J. Pick, A. J. Glover, and R. Hoff (1991), “Bursting of Line Pipe with Long External Corrosion”, Int. J. Pres. Ves & Piping, 46, pp. 195-215.

[31]. B. A. Chouchaoui, R. J. Pick, and D. B. Yost (1992), “Burst Pressure Predictions of Line Pipe Containing Single Corrosion Pits Using the Finite Element Method", OMAE, Vol. V-A, pp. 203-210.

[32]. B. Fu and M.G. Kirkwood (1995a), “Determination of Failure Pressure of Corroded Line Pipes Using the Nonlinear Finite Element Method”, Pipeline Technology Conference, Belgium, Vol. II, pp. 1-9, 1995.

[33]. D. R. Stephens, B. N. Leis, and D. L. Rudland, “Influence of Mechanical Properties and Irregular Geometry on Pipeline Corrosion Defect Behavior”, 1997.

[34]. F. J. Klever, G. Stewart, A. C. Clemens, and V. Valk (1995), “New Developments in Burst Strength Predictions for Locally Corroded Pipelines”, OMAE, Vol. V, pp. 161-173,1995.

[35]. C. H. Popelar (1993), “A Plane Strain Analysis Model for Corroded Pipelines”, OMAE, Vol. V, pp. 281-288, 1993.

[36]. B. N. Leis, and D. R. Stephens (1997), “An Alternative Approach to Assess the Integrity of Corroded Line Pipe”, Seventh International Offshore and Polar Engineering Conference, May 1997.

[37]. ABAQUS manual.

[38]. NDT Resource Center, www.ndted.org, April 2010.

[39]. R. Rice, “A Path Independent Integral and the Approximate Analysis of Strain Concentration by Notches and Cracks”, Journal of Applied Mechanics, 35, 1968, pp. 379-386. .

[40]. European SINTAP Procedure,”Fitness-for-Service Fracture Assessment of Structures Containing Cracks”, 2007.

[41]. American Petroleum Institute, “Recommended Practice for Fitness for Service”, API 579, 2000.

[42]. American Society for Testing and Materials (ASTM) Standards, ASTM E8, 2008.

[43]. D. S. Cronin and A. Plumtree, “Assessment of Crack in Corrosion Defects in natural Gas Transmission Pipelines”, 7th International Pipeline Conference (September29-October 3, 2008).

[44]. American Petroleum Institute, “Recommended Practice for Fitness for Service”, Appendix D, API -579, 2000.

[45]. American Petroleum Institute, “Recommended Practice for Fitness for Service”, Appendix C, API -579, 2000.

[46]. British Standards Institute, BS 7910. “Guide on Methods for Assessing the Acceptability of Flaws in Metallic Structures”, Appendix M, BSI-10 2000.

Appendix A

a) Reference Stress API 579 (Cylinder Approach):

To calculate the reference stress of a cylinder under internal pressure containing semi-elliptical surface crack, the following equation should be used [44] :

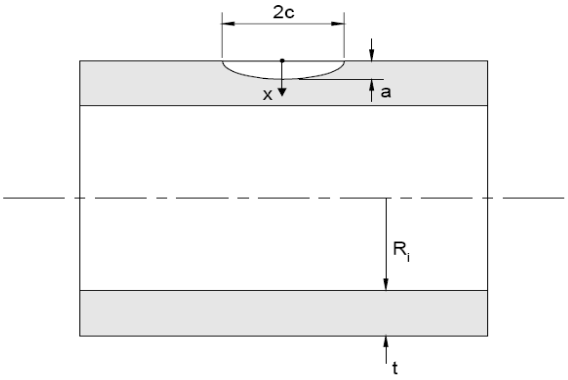

Figure A. 1 Cylinder – Surface Crack, Longitudinal Direction-Semi-elliptical Shape [44].

$$\sigma_{ref} = M_s \mathrm{P_m}$$

Where

P_m: Hoop Stress

Folias bulging factor $M_s$is given by:

$$\mathrm{M_s} = \frac{1-0.67\frac{a}{t}\left(\frac{1}{M_t}\right)}{1-0.67\frac{a}{t}}$$

$$M_t = \frac{1.02 + 0.4411\lambda^2 + .006124\lambda^4}{1 + .02642\lambda^2 + 1.533X10^{-6}\lambda^4}$$

$$\lambda = \frac{1.818C}{\sqrt{\mathrm{t}R_i}}$$

b) Stress Intensity API 579 (Cylinder Approach):

To calculate the stress intensity of a cylinder under internal pressure containing semi-elliptical surface crack, the following equation should be used [45] :

$$K_I = \frac{\mathrm{PR_i^2}}{\mathrm{R_o^2 - R_i^2}}[2G_0 \ + 2G_1(\frac{a}{\mathrm{R_i}}) \ + 3G_2(\frac{a}{\mathrm{R_i}})^2 + 4G_3(\frac{a}{\mathrm{R_i}})^3 + 5G_4(\frac{a}{\mathrm{R_i}})^4]\sqrt{\frac{\pi a}{Q}}$$

For the coefficients G_0 and G_1 for inside and outside surface cracks the following equation can be used:

$$G_0 = \mathrm{A_{0,0}} + \mathrm{A_{1,0}}\beta + \mathrm{A_{2,0}}\beta^2 + \mathrm{A_{3,0}}\beta^3 + \mathrm{A_{4,0}}\beta^4 + \mathrm{A_{5,0}}\beta^5 + \mathrm{A_{6,0}}\beta^6$$

$$G_1 = \mathrm{A_{0,1}} + \mathrm{A_{1,1}}\beta + \mathrm{A_{2,1}}\beta^2 + \mathrm{A_{3,1}}\beta^3 + \mathrm{A_{4,1}}\beta^4 + \mathrm{A_{5,1}}\beta^5 + \mathrm{A_{6,1}}\beta^6$$

Where

β Is given by following Equation

$$\beta = \frac{2\varphi}{\pi}$$

The parametersA_{ij}, are provided in Table C.11 [45].

To determine the influence coefficients G_2 ,G_3 and G_4, paragraph C.14.3 or C.14.4 [45]can be used.

Q is giving by the following equation:

Q=1+1.464 $(\frac{a}{c})^{1.65}$

σ_0: Uniform coefficient for polynomial stress distribution (MPa or psi)

a) Reference stress BS 7910 (Cylinder Approach):

To calculate the reference stress of a cylinder under internal pressure containing semi-elliptical surface crack, the following equation should be used [20]:

$$\sigma_{ref} = 1.2M_s \mathrm{P_m}$$

Where

$$M_s=\frac{1-\{\frac{a}{t\mathrm{M_t}}\}}{1-\frac{a}{t}}$$

$$\mathrm{M_t} = \{1 + 1.6\left(\frac{\mathrm{c}^2}{2\mathrm{R_i t}}\right)\}^{0.5}$$

b) Stress intensity BS 7910 (Cylinder Approach):

To calculate the reference stress of a cylinder under internal pressure containing semi-elliptical surface crack, the following equation should be used [46]:

$$K_I = \mathrm{M}\mathrm{f}_{\mathrm{w}}\mathrm{M}_{\mathrm{m}}\sigma_{\mathrm{m}}\sqrt{\pi a}$$

Where

$$f_w = \{\sec(\frac{\pi a c}{\mathrm{tW}})\}^{0.5}$$

$$\mathrm{M}{=}\frac{1-\{\frac{a}{t\mathrm{M}_{\mathrm{t}}}\}}{1-\frac{a}{t}}$$

$$\mathrm{M}_{\mathrm{t}} = \{1 + 3.2\left(\frac{\mathrm{c}^2}{2\mathrm{R}_{\mathrm{m}}\mathrm{t}}\right)\}^{0.5}$$

$$\mathrm{M}_{\mathrm{m}} = \left\{\mathrm{M}\left\{\mathrm{M}_1 + \mathrm{M}_2\left(\frac{a}{\mathrm{t}}\right)^2 + \mathrm{M}_3\left(\frac{a}{\mathrm{t}}\right)^4\right\}\mathrm{g}\mathrm{f}_{\varphi}\mathrm{f}_{\mathrm{w}}\right\}/\mathrm{Q}$$

$$\mathrm{M}_1 = 1.13 - 0.09(\frac{a}{c})$$

$$\mathrm{M}_2 = \frac{0.89}{0.2 + (\frac{a}{c})} - 0.54$$

$$M_3=0.5-\frac{1}{0.65+(\frac{a}{c})}+14\{1-\left(\frac{a}{c}\right)\}^{24}$$

$$Q=\{1+1.464\,(\frac{a}{c})^{1.65}\}^{0.5}$$

In the present case:

For deep point:

$$g=1$$

$$f_{\varphi}=1$$

For surface point:

$$g=\{1.1+0.35\left(\frac{a}{t}\right)^{2}\}$$

$$f_{\varphi}=\left(\frac{a}{c}\right)^{0.5}$$

Appendix B

- **J-Integral Test Analysis**

Table B. 1 shows the J-Integral test results.

Table B. 1 J-Integral First Test Set Results

Specimen #	**CMOD (in)**	**a_o (mm)**	**a_p (mm)**	**Δa (mm)**	**Δa_p (mm)**	**b_o (mm)**	**J_{el} (KJ / m^2)**	**J_{pl} (KJ / m^2)**	**J_{tot} (KJ / m^2)**
3.00	**0.01**	2.25	2.32	0.07	*0.07*	3.05	6.26	70.8	77.1
6.00	**0.03**	2.19	2.42	0.23	*0.23*	3.11	6.53	169	175
7.00	**0.03**	2.21	2.64	0.43	*0.43*	3.09	5.58	188	193
7-adj	**0.03**	2.21	2.64	0.43	*0.43*	3.09	5.54	204	210
4.00	**0.05**	2.44	3.02	0.57	*0.57*	2.86	4.21	274	278
2.00	**0.06**	2.43	3.30	0.87	*0.87*	2.87	2.78	349	352
1.00	**0.07**	2.21	3.31	1.10	*1.10*	3.09	2.61	439	442

The above results needed to be analyzed in order to evaluate $J_{0.2}$. The analysis was done according to ASTM E1820 – 08 [18]. The procedure and the result of analyzing one of the three test sets are summarized in the following steps:

1. Correcting the crack growth:
    1. Because crack growth is not monitored in the basic test procedure, a multiple-specimen technique is required to obtain the J-R curve. J-Integral values were calculated for 7 specimens from the first test set. The following equation was used to correct J-Integral initial results:

$$J = Jel_o + \frac{Jpl_o}{1 + \left(\frac{\alpha - 0.5}{\alpha + 0.5}\right)\frac{\Delta a}{b_o}}$$

While $\alpha = 1 \, for \, SE(B)$

2. Fit a power law curve of the expression $J = J_{1mm}\,\Delta a^{m}$ to the corrected data that have crack growth exceeding ($\Delta a/bo \geq 0.05$). Table B. 2 shows the corrected J, and Figure B. 1 shows the curve fitted.

Table B. 2 J-Integral Crack Growth Correction

Specimen #	Δa mm	J_{total} (KJ/m^2)	Corrected J (KJ / m2)
3.00	0.07	77.1	76.5
6.00	0.23	175	171
7.00	0.43	193	185
7-adj	0.43	210	201
4.00	0.57	278	261
2.00	0.87	352	320
1.00	1.10	442	396

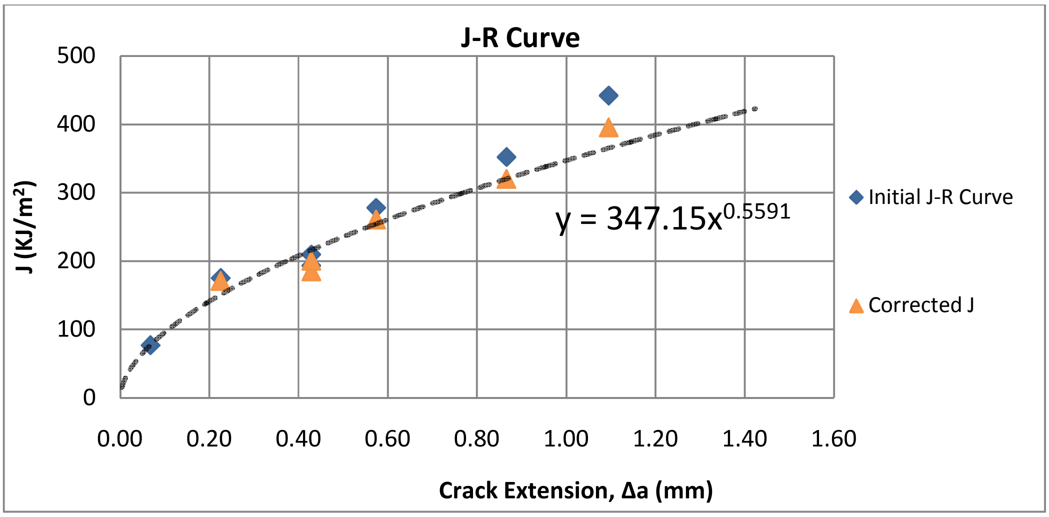

Figure B. 1 Power-law Curve Fitting to the Corrected Crack Extension

3. Calculate the final crack growth corrected using m = 0.5591 for the equation bellow:

$$J = Jel_o + \frac{Jpl_o}{1 + \left(\frac{\alpha - m}{\alpha + m}\right)\frac{\Delta a}{b_o}}$$

Table B. 3and Figure B. 2 represent the results of correcting J.

Table B. 3 Crack Growth Final Correction

Specimen #	Δa mm	J_{total} (KJ/m^2)	Corrected J (KJ / m^2)	Δa/b_o >0.05	Final crack growth corrected J (KJ / m^2)
3.00	0.07	77.1	76.5	0.02	76.6
6.00	0.23	175	171	0.07	172
7.00	0.43	193	185	0.14	186
7-adj	0.43	210	201	0.14	202
4.00	0.57	278	261	0.20	263
2.00	0.87	352	320	0.30	325
1.00	1.10	442	396	0.35	402

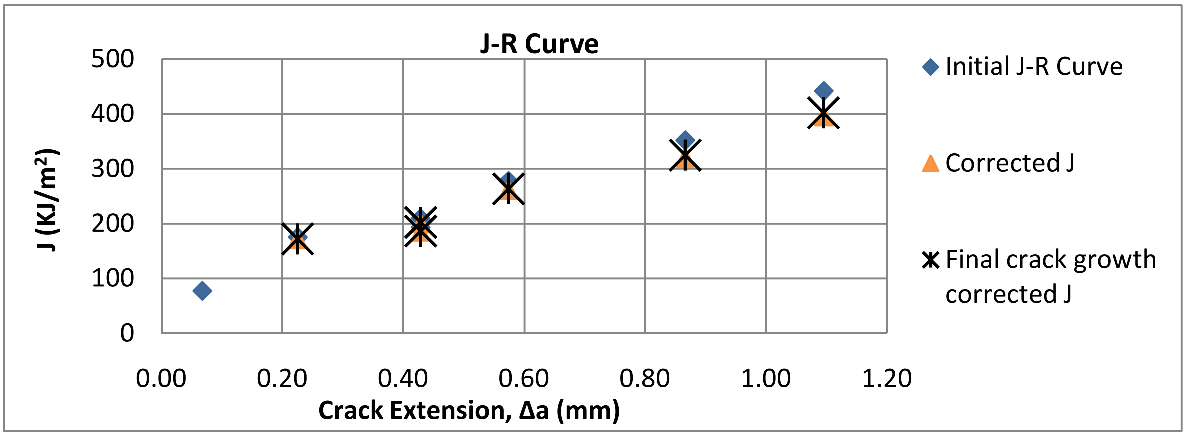

Figure B. 2 Crack Growth Final Correction

4. Measurement Capacity of Specimen: This capacity should then form a qualification area which should contain more than two points to evaluate $J_{IC.}$

   a. Set the maximum capacity of the J-Integral by taking the smaller J_{max} of the following:

$$J_{max} = b_o \sigma_Y / 10$$

$$J_{max} = B \sigma_Y / 10$$

$$\sigma_Y = \frac{\sigma_{ys+} \sigma_{uts}}{2}$$

   b. Set the maximum crack extension capacity by the following:

$$\Delta a_{max} = 0.25 b_o$$

$$\Delta a_{max} = 0.76 \text{ mm}$$

The results are shown as follows in Table B. 4 while Figure B. 3 shows the limit lines

Table B. 4 Measurement Capacity of Specimen

J_{max} = b_o σy/10 (KJ/m^2)	J_{max} = B σy/10 (KJ/m^2)	Δa_{max} = 0.25*b_o (KJ/m^2)
160	279	0.76
163		0.78
162		0.77
162		0.77
150		0.71
151		0.72
162		0.77
163	**279**	**0.78**

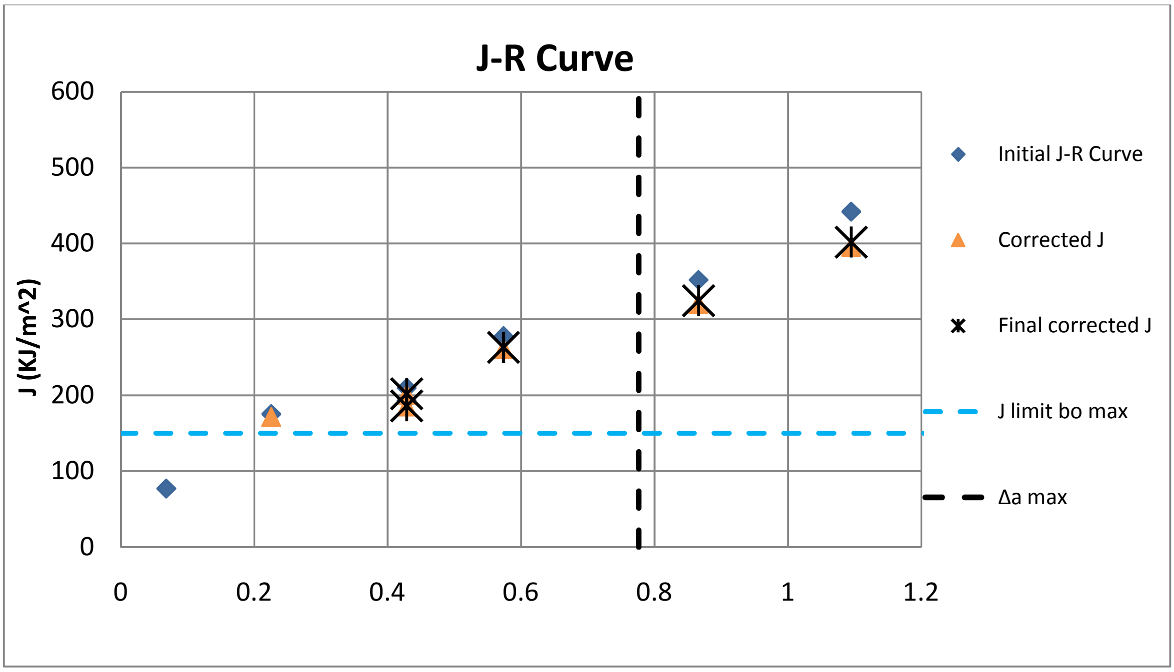

Figure B. 3 (J-R Curve) the Capacity of Specimen

Apparently from Figure B. 3 the limits are very small to contain enough qualified data for evaluating J_{IC}. The reason for the small capacity is the small pipe thickness that results in a small remaining ligament (b_o).

5. J_{IC} Evaluation:

Basic method was used to determine the toughness of the material near the onset of the crack extension from preexisting fatigue crack. The beginning stage of material crack growth resistance development is marked by the J_{IC}.

a. Calculate J according to the following equation and plot J versus Δa (J-R curve) as in Figure B. 4.

$$J = M\sigma_Y \Delta a$$

Table B. 5 Calculation of J and J_{limit}

B (mm)	**J=MσYΔa (KJ/m^2)**	**bo**	**J_{limit}= b_o σy/7.5**
3.05	69.4	3.05	208
3.11	231	3.11	212
3.09	439	3.09	211
3.09	439	3.09	211
2.86	588	2.86	195
2.87	888	2.87	196
3.09	1121	3.09	211

b. Plot construction lines from J

c. Draw exclusion line parallel to construction line intersecting the abscissa at 0.15 mm.

d. Draw exclusion line parallel to construction line intersecting the abscissa at 1.5 mm.

e. Plot all J – Δa data points that fall inside the area enclosed by these two exclusion lines and capped by J_{limit}

$$J_{limit} = b_o\sigma_Y/7.5 .$$

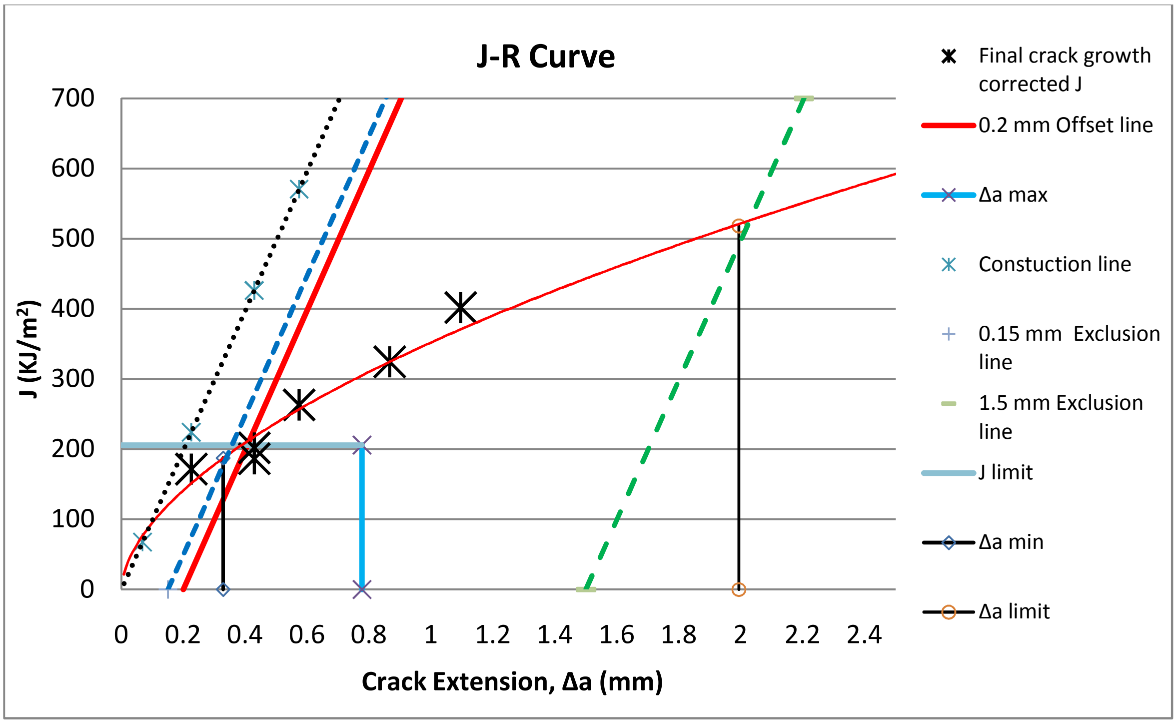

Figure B. 4 J-R Curve for Determining J_{IC}

As expected from the capacity lines, there are not enough qualified data according to Figure B. 5. Even after proceeding with fitting the curve and making the intersection between the 0.2mm offset line and the fitted curve to determine a provisional J_Q, the data is still not qualified for J_{IC} because of the following qualification requirements:

- The power coefficient C2 shall be less than 1.
- J_Q can be equivalent to J_{IC} if:
  - the thikness $B > 10\ J_Q/\sigma_Y$
  - the intial legament $b_o > 10\ J_Q/\sigma_Y$

- the slope of the power law regression $\Delta a_Q < \sigma_Y$

To evaluate J_{IC} an intersection between the 0.2mm offset line and the fitted curve should be plotted. This intersection point is to determine a provisional J_Q. The data should meet some conditions so that the provisional J_Q can be accounted as the material fracture toughness J_{IC}.

6. Data Qualifications:

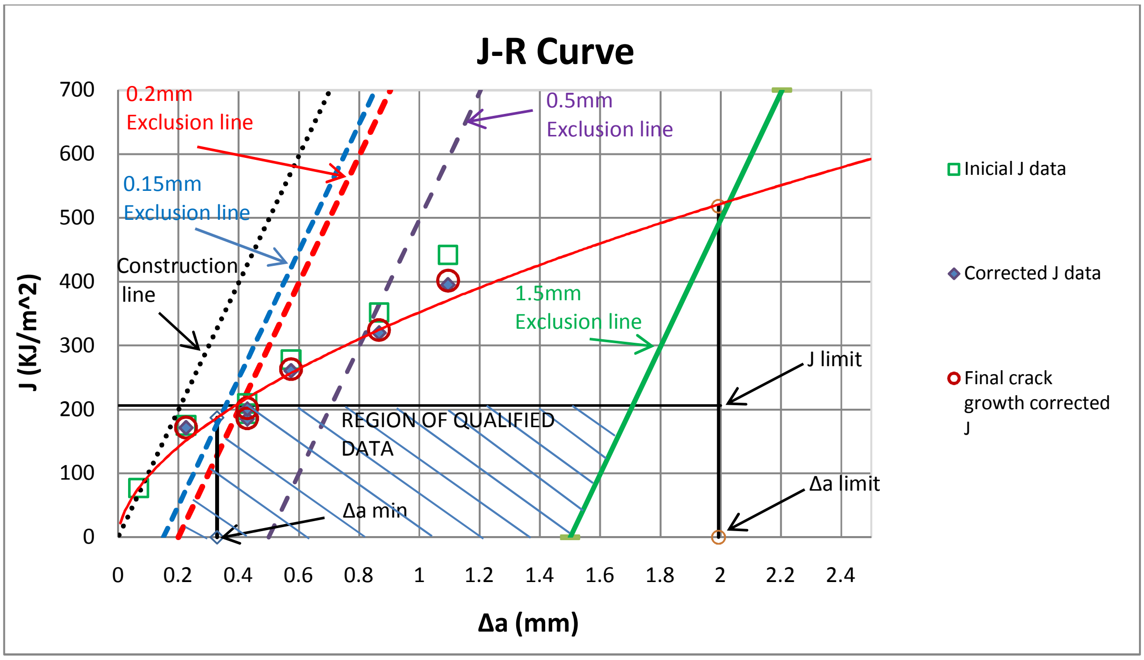

Figure B. 5 Qualified Data on J-R curve